

Numerical Simulations of NS-DBD Plasma Actuators For Flow Control

Popov, Ilya

DOI

[10.4233/uuid:f2fa6bd6-4419-494c-ab14-f0c1ec020270](https://doi.org/10.4233/uuid:f2fa6bd6-4419-494c-ab14-f0c1ec020270)

Publication date

2016

Document Version

Final published version

Citation (APA)

Popov, I. (2016). *Numerical Simulations of NS-DBD Plasma Actuators For Flow Control*. [Dissertation (TU Delft), Delft University of Technology]. <https://doi.org/10.4233/uuid:f2fa6bd6-4419-494c-ab14-f0c1ec020270>

Important note

To cite this publication, please use the final published version (if applicable).
Please check the document version above.

Copyright

Other than for strictly personal use, it is not permitted to download, forward or distribute the text or part of it, without the consent of the author(s) and/or copyright holder(s), unless the work is under an open content license such as Creative Commons.

Takedown policy

Please contact us and provide details if you believe this document breaches copyrights.
We will remove access to the work immediately and investigate your claim.

NUMERICAL SIMULATIONS OF NS-DBD PLASMA ACTUATORS FOR FLOW CONTROL

NUMERICAL SIMULATIONS OF NS-DBD PLASMA ACTUATORS FOR FLOW CONTROL

Proefschrift

ter verkrijging van de graad van doctor
aan de Technische Universiteit Delft,
op gezag van de Rector Magnificus prof. ir. K.C.A.M. Luyben,
voorzitter van het College voor Promoties,
in het openbaar te verdedigen op 22 Maart 2016 om 15:00 uur

door

Ilya POPOV

Master of Applied Physics and Mathematics
Moscow Institute of Physics and Technology
geboren te Moskou, Rusland.

Dit proefschrift is goedgekeurd door de

promotor: Prof. dr. F. Scarano

copromotor: Dr. S. J. Hulshoff

Samenstelling promotiecommissie:

Rector Magnificus,

Prof. dr. F. Scarano,

Dr. S. J. Hulshoff,

Onafhankelijke leden:

Prof. dr. U. Ebert,

Prof. J-P. Boeuf,

Prof.dr.ir. L.L.M. Veldhuis,

Prof.dr.ir. G.A.M. van Kuik,

Dr A. Y. Starikovskiy,

Overige leden:

Dr. M. Kotsonis,

voorzitter

Technische Universiteit Delft, LR, promotor

Technische Universiteit Delft, UD-LR, copromotor

CWI Amsterdam

CNRS U. Paul Sabatier

Technische Universiteit Delft, LR

Technische Universiteit Delft, LR, reservelid

Princeton University, USA

Technische Universiteit Delft, UD-LR



Keywords: flow control, plasma actuators, transition, separation

Printed by: Sieca Repro

Front & Back: Image created by J. O'Sullivan. CC-BY license.

Copyright © 2015 by Ilya Popov

[Creative Commons Attribution-ShareAlike 4.0 International License](https://creativecommons.org/licenses/by-sa/4.0/)

ISBN 978-94-6186-617-2

An electronic version of this dissertation is available at

<http://repository.tudelft.nl/>.

In memory of my father

Contents

Contents	vii
Summary	xi
Samenvatting	xiii
Nomenclature	xv
1 Introduction	1
2 Flow control	7
2.1 Overview	7
2.2 Flow control examples	9
2.3 Plasma flow control	13
2.4 Plasma actuators	14
2.4.1 AC-DBD plasma actuators	15
2.4.2 NS-DBD plasma actuators	16
2.5 Summary	21
3 NS-DBD plasma actuators	23
3.1 The physics of plasma	24
3.2 The physics of discharges	27
3.3 The layout of NS-DBD actuators	29
3.4 Operating parameters	30
3.5 Electrical measurements	34
3.5.1 Introduction	34
3.5.2 Experimental setup	36
3.5.3 Low voltage measurements	37
3.5.4 High voltage measurements	39
3.5.5 Energy per pulse	48
3.5.6 Conclusions from the experiments	50

4	NS-DBD actuator modeling	51
4.1	Introduction	51
4.2	NS-DBD effects and model assumptions	52
4.2.1	Compressible and thermodynamic effects	52
4.2.2	Momentum deposition	55
4.2.3	Spanwise uniformity of the actuator effects	56
4.2.4	Temporal properties	58
4.2.5	Proposed model	59
4.2.6	Numerical implementation aspects	60
5	Actuator in a laminar boundary layer	63
5.1	Introduction	63
5.2	Simulation setup	64
5.2.1	Simulation domain	64
5.2.2	Actuator model	65
5.3	Comparison to experimental measurements	65
5.4	Comparison to linear stability theory	66
5.4.1	Linearization error	71
5.4.2	Parallel flow assumption	72
5.4.3	The difference between the POD and LST analysis	72
5.4.4	Numerical errors of the simulation	75
5.5	Conclusions	75
6	Actuator in a free shear layer	79
6.1	Introduction	79
6.2	Actuator model	80
6.3	Simulation description	80
6.4	Results	82
6.4.1	Acoustic wave	82
6.4.2	Velocity oscillations and vortex structure	82
6.4.3	Entropy spot	87
6.4.4	Flow statistics	87
6.4.5	Comparison with linear stability theory	88
6.4.6	Effect of varying energy input	94
6.4.7	Mesh convergence	94
6.5	Conclusions	94
7	Conclusions and outlook	99
7.1	Conclusions	99
7.2	Outlook	100

A	NS-DBD plasma actuators on airfoils	103
A.1	Introduction	103
A.2	Setup and meshing	104
A.2.1	Boundary conditions	104
A.2.2	Turbulence model	106
A.3	Results	106
A.4	Analysis and conclusions	107
B	Proper orthogonal decomposition	111
B.1	Algorithm description	111
B.1.1	Introduction	111
B.1.2	Construction of POD basis	112
B.1.3	Projection of the N-S equations	114
B.1.4	Flow rate conservation	114
B.1.5	SGS model	115
B.1.6	Weighting	116
B.2	Validation	116
B.2.1	Laminar vortex shedding	116
B.2.2	Free shear layer	121
C	Linear stability theory	127
C.1	Introduction	127
C.2	Temporal stability	128
C.3	Spatial stability	129
C.4	Validation	130
C.5	Implementation details	132
	Index	133
	Bibliography	135
	List of publications	145
	Acknowledgements	149
	Curriculum Vitæ	151

Summary

Nanosecond dielectric barrier discharge (NS-DBD) plasma actuators is relatively new means of flow control. It has several advantages compared to more conventional means of flow control, such as small size, low weight, fast response time and controllability. It has been demonstrated to be able to promote transition of boundary layers and to postpone flow separation on aerodynamic surfaces. This makes the NS-DBD actuator a promising technology for many applications in aerospace and wind energy industries.

This thesis presents a study of NS-DBD actuator effects by numerical simulations. For the purposes of simulations of fluid-dynamic effects of the actuation, complex plasma dynamic processes are modeled by their thermal effects. This is possible due to a large separation of scales between plasmadynamic, thermodynamic and fluid dynamic phenomena. The resulting model is embedded into the compressible computational fluid dynamics (CFD) simulation using Navier-Stokes equations. This model is then used in numerical simulations in two model flows: a laminar boundary and a free shear layer. These model flows are relevant for promotion of laminar to turbulent boundary layer transition and laminar leading edge separation elimination.

For the laminar boundary case, the effect of a burst of discharges on a flat plate boundary layer is studied. The shape, wavelength and propagation speed of the disturbance introduced into the boundary layer by actuation are compared to experimental results and found to be in agreement. This indicates that the thermal model is adequate at predicting phenomenological effects of the actuation in this case. POD analysis of the CFD flow fields is employed to identify the dominating modes of the disturbance. The dominating mode is found to be the same as the least stable mode predicted by linear stability theory. A compression wave, however, is not found to play an important role, and the burst of pulses is found to produce the same effects as the long pulse with the same total energy.

For the free shear layer case, the model of the actuator is placed on a centerline in the beginning of a free shear layer. As a result of constant frequency actuation, early formation of vortices and shear layer breakdown are observed. Each actua-

tion event produces a convective disturbance in the flow field. Dynamics of the disturbances are analyzed and growth rates are found to be in agreement with the predictions of linear stability theory. A parametric study is carried out to study scalability of the actuator effects to change of actuation frequency and energy per pulse. A saturation effect with the increase of actuation frequency is observed.

For both studied cases, the effect of NS-DBD actuation is excitation of natural instability modes, which then evolve according to the stability properties of the flow.

Samenvatting

Nanosecond dielectric barrier discharge (NS-NBD) plasma actuators zijn een relatief nieuwe manier om een luchtstroom te beïnvloeden. Het heeft meerdere voordelen in vergelijking met meer conventionele methodes om de luchtstroom te controleren, zoals een kleine grootte, laag gewicht, snelle responstijden en beheersbaarheid. Het is gedemonstreerd dat het overgangspunt van laminaire naar turbulente grenslagen kan worden bevorderd, en loslating van de stroming kan worden uitgesteld op aërodynamische vormen. Hierdoor is de NS-NBD actuator een veelbelovende technologie for meerdere toepassingen in de lucht- en ruimtevaart industrie, en de wind energie industrie.

Deze scriptie presenteert een studie van NS-DBD actuator effecten met behulp van numerieke simulaties. Voor de simulatie van luchtstroom-dynamische effecten door de actuator, worden de complexe dynamische plasma processen gemodelleerd met thermische effecten. Dit is mogelijk door een grote scheiding van de schalen tussen de dynamiek van de plasma, warmte en luchtstroom fenomenen. Het resulterende model is ingebed in een compressibele computational fluid dynamics (CFD) simulatie van de Navier-Stokes vergelijkingen. Dit model is vervolgens gebruikt in numerieke simulaties in twee model stromingen: een laminaire grenslaag en een vrije schuiflaag. Deze model stromingen zijn relevant voor de bevordering van laminaire naar turbulente grenslaag loslating en de voorrand separatie eliminatie.

In het geval van de laminaire grenslaag, zijn de effecten van een uitbarsting van lozingen op een vlakke plaat grenslaag bestudeerd. De vorm, golflengte en voortplantingssnelheid van de verstoring die is geïntroduceerd in de grenslaag door de actuator worden vergeleken met experimentele resultaten, en zijn in overeenstemming met elkaar. In dit geval geeft het weer dat het warmte model voldoende de fenomenen van de actuatie heeft voorspeld. POD analyse van de CFD stromingsvelden wordt gebruikt om de dominante modi van de verstoring te identificeren. De dominante modus die is gevonden is dezelfde als de minst stabiele modus voorspeld door lineaire stabiliteits theorie. Echter, een compressiegolf speelt geen belangrijke rol, en een uitbarsting van pulsen produceert dezelfde

effecten als een lange puls met dezelfde totale energie.

In het geval van de vrije schuijflaag, wordt het model van de actuator geplaatst op de middellijn aan het begin van een vrije schuijflaag. As gevolg van constante frequentie aandrijving, wordt een vroege formatie van draaikolken en het afbreken van de schuijflaag geobserveerd. Elke actuatie gebeurtenis produceert een convectieve verstoring in het stromingsveld. De dynamiek van de verstoringen zijn geanalyseerd, en groeicijfers komen overeen met de voorspellingen van lineaire stabiliteits theorie. Een parameterstudie is uitgevoerd om de schaalbaarheid van de actuatie effecten te bestuderen wanneer de actuatie frequentie en energie per puls worden veranderd. Een verzadigings effect met het verhogen van de actuatie frequentie is waargenomen.

Voor beide gevallen die zijn bestudeerd, is het effect van de NS-DBD actuatie de opwekking van natuurlijke instabiliteits modi, welke vervolgens evolueren volgens de stabiliteits eigenschappen van de stroming.

Nomenclature

Symbol	Expression	Unit	Description
x		m	streamwise coordinate
y		m	wall-normal coordinate
z		m	spanwise coordinate
U		m/s	flow velocity
u, v, w		m/s	components of the flow velocity in x, y, z directions
U_∞		m/s	freestream flow velocity
l		m	characteristic size in the flow-wise direction
h		m	characteristic size in the wall-normal direction (for example, channel half-height, boundary layer thickness)
p		$\text{kg/m} \cdot \text{s}^2$	Pressure
q	$\frac{\rho U^2}{2}$	$\text{kg/m} \cdot \text{s}^2$	Dynamic pressure
ρ		kg/m^3	fluid density
μ		$\text{kg/m} \cdot \text{s}$	dynamic viscosity
ν	$\frac{\mu}{\rho}$	m^2/s	kinematic viscosity

Symbol	Expression	Unit	Description
Boundary layer			
τ_w	$\mu \left(\frac{\partial u}{\partial y} \right) \Big _{y=0}$	$\text{kg/m} \cdot \text{s}^2$	wall shear stress
u_*	$\sqrt{\frac{\tau_w}{\rho}}$	m/s	friction velocity
y^+	$\frac{u_* y}{\nu}$	—	dimensionless boundary layer wall-normal coordinate
u^+	$\frac{u}{u_*}$	—	dimensionless boundary layer flow velocity
δ^*	$\int_0^\infty \left(1 - \frac{u(y)}{U_\infty} \right) dy$	m	displacement thickness
θ	$\int_0^\infty \frac{u(y)}{U_\infty} \left(1 - \frac{u(y)}{U_\infty} \right) dy$	m	momentum thickness
δ_{99}		m	thickness at which flow velocity reaches 99% of the freestream velocity
Re	$\frac{Ul}{\nu}$	—	Reynolds number
Re_τ	$\frac{u_* h}{\nu}$	—	Wall shear stress based boundary layer Reynolds number
Re_{δ^*}	$\frac{U\delta^*}{\nu}$	—	Reynolds number based on displacement thickness
Re_θ	$\frac{U\theta}{\nu}$	—	Reynolds number based on momentum thickness
Periodic motion			
f		Hz = 1/s	Frequency
ω	$\frac{d\alpha}{dt} = 2\pi f$	1/s	Angular velocity
St, f^+	$\frac{fl}{U}$	—	Strouhal number, also known as reduced frequency
Compressibility and thermodynamics			
T		K	Temperature

Symbol	Expression	Unit	Description
m		kg/mol	Molar mass
R	8.31	J/mol · K	Universal gas constant
R_s	$R_s = R/m$	J/kg · K	Specific gas constant
k	1.38×10^{-23}	J/K	Boltzmann constant
C_p		J/kg · K	Specific heat capacity at constant pressure
C_V	$C_p - R_s$	J/kg · K	Specific heat capacity at constant volume
γ	C_p/C_V	—	Heat capacity ratio
U_s	$\sqrt{\frac{\gamma RT}{m}}$	m/s	Speed of sound
Ma	$\frac{U}{U_s}$	—	Mach number
Electrical			
V		V	Voltage
I		A	Current
P	$V \cdot I$	W	Electric power
E	$\int P dt$	J	Energy
Z		Ω	Impedance
c	3.00×10^8	m/s	Speed of light
Q		C	Charge
C	Q/V	F	Electric capacity
Wings and Airfoils			
α		deg	Angle of attack

Symbol	Expression	Unit	Description
c		m	Chord length
b		m	Wing span
A		m ²	Wing area
AR	$\frac{b^2}{A}$	—	Wing aspect ratio
L		kg · m/s ²	Lift force (normal to the flow direction)
D		kg · m/s ²	Drag force (along the flow direction)
M		kg · m ² /s ²	Pitching moment
C_L	$L = C_L A \rho U^2 / 2$	—	Lift coefficient
C_D	$D = C_D A \rho U^2 / 2$	—	Drag coefficient
C_M	$M = C_M A c \rho U^2 / 2$	—	Moment coefficient

Chapter 1

Introduction

The aviation industry is one of the most technologically advanced industries in the modern world, yet still faces many challenges. These include economical, safety and environmental challenges, among others. Success in all these areas greatly depends on a key characteristic of any aircraft — its aerodynamic performance.

One of the biggest limiting factors in aerodynamic performance is the occurrence of *separation*. Separation is a condition where the flow over an aerodynamic surface under strong adverse pressure gradient separates from the surface, creating an area of counterflow. Separation occurs on the suction (upper) side of airfoils at high angles of attack, above the so-called critical angle of attack, as illustrated in [Figure 1.1](#). As a consequence, the lift force generated by the wing is greatly reduced, and at the same time the drag force is increased. This condition, called *stall*, can lead to various dangerous consequences, such as high descent rates or loss of control. Wing stall defines the lower limit for the landing speed of an airplane, while the stall of retreating rotor blades limits the maximum speed of helicopters. Stall can also cause high dynamic loads on wind turbine blades.

Modern large airplanes (for example, passenger airliners, as shown in [Figure 1.2](#)) use (*high lift devices*) to improve maximum lift. These include trailing edge flaps and leading edge slats and slots, which effectively change the shape of the wing at takeoff and landing to provide higher lift. Slats and slots do so by preventing separation, while flaps increase generated lift. These devices can be effective, but are often heavy and consist of many moving parts. They are also and relatively slow to control.

The performance of high lift devices can be improved using additional flow control. Flow control is a colloquial name for methods used to change the behavior

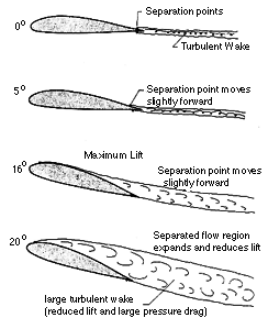


Figure 1.1: Flow separation on a wing happens at a high angle of attack, causing loss of lift and increase of drag. Image: NASA.



Figure 1.2: Example of elaborate high lift devices: triple slotted flaps on a wing of Boeing-737 airliner. Image: NASA.

of the flow compared to its natural behavior. Many different techniques have been proposed, including vortex generators, suction, blowing, air jets, vibrating strings and periodic excitation. Some of these have proven to be effective (such as vortex generators) and have seen practical application (Figure 2.2). Existing flow control techniques have their drawbacks, however, such as parasitic drag, mechanical complexity, and large energy consumption. Thus research in the field of separation control is ongoing.

Recently another candidate for separation control has come to the attention — dielectric barrier discharge (DBD) plasma actuators [9]. The plasma actuator is a device in a shape of a tape, which can be attached to an aerodynamic surface. By applying high-voltage signal, it generates plasma, which affects the flow in the vicinity of the actuator. It has been demonstrated in experiments that plasma actuators can postpone separation on airfoils [39, 44, 58, 63, 67]. There are two different types of DBD plasma actuators. These are defined by the kind of signal they are fed with: alternating current (AC) and nanosecond pulses (NS). The two kinds of actuators have different principles of operation and thus different flow control capabilities.

To date AC-DBD plasma actuators have been more extensively studied and thus better understood [10, 31, 44]. Their effect is found to be due to the volumetric body force that is applied by the electric field upon the ions in the plasma [10, 30, 34]. This body force can, in turn, produce a jet, which can be used to increase mixing in the boundary layer or a free shear layer, thus making it less susceptible to separation.

NS-DBD actuators, however, are much less understood, although there are several phenomenological observations from experiment demonstrating the effects they can produce [49, 58, 61, 63, 72]. It has been shown, for example, that the NS-DBD actuator can force the transition of a laminar boundary layer and postpone separation, especially in the case of a laminar leading edge separation (Figure 1.3). These experiments, although demonstrating the effectiveness of NS-DBD actuator in certain conditions, have also shown large variation in the achieved flow control authority. Thus, there are still questions unanswered, the most important of which are:

- Can a model of NS-DBD actuators be developed which is efficient enough to be used in computational simulations of flow control?
- Can such a model be used to predict the experimentally-observed effects of NS-DBD actuators on separation?
- If so, what are the most relevant physical processes for actuation?
- In what conditions are NS-DBD actuators most effective?



Figure 1.3: Example of flow separation control with the NS-DBD plasma actuators on a large scale model. top — no actuation, bottom — with actuation.

In order to address these questions, this thesis first reviews the known characteristics of NS-DBD actuators, then proposes an efficient model for their effects. The model is then evaluated for its ability to predict the phenomenology of actuation, and results from numerical studies of the effects of NS-DBD actuation on two key types of flow relevant to separation control are described. The results are compared to predictions from linear stability theory and experiments. This allows the relevant physical aspects of the phenomena to be identified, and helps to build a basis for numerical tools intended for the prediction and optimization of the performance of NS-DBD actuators in various conditions.

Thesis outline The layout of the thesis is following. Chapter 2 gives an overview of the flow control techniques and its classification. Chapter 3 discusses physics behind NS-DBD plasma actuators and their operating parameters. In chapter 4 a thermal model of ND-DBD plasma actuators is proposed. Then, the model is used for simulations of actuation effects in two flows: a laminar boundary layer (chapter 5) and a free shear layer (chapter 6). Finally, conclusions are given in chapter 7.

Chapter 2

Flow control

This chapter gives a brief introduction to flow control techniques, describing their properties and history. It starts from the general principles of flow control and classification of flow control techniques, giving a number of examples. The chapter then focuses on different types of plasma actuators. The existing experimental and theoretical results for NS-DBD actuators are discussed in detail. It is explained why there is a place for yet another method of flow control — NS-DBD plasma actuators.

Overview

In order to improve the performance of aerodynamic forms, it is desirable to change the properties of their associated flows in a controlled manner over a range of conditions. Collectively, the methods developed to do so are called *flow control* methods. Flow control methods differ by their goals, physical mechanisms and technical implementation.

Depending on the specific application, different properties are targeted. Common examples include aerodynamic lift (such as on aircraft wings and wind turbine blades [24]), aerodynamic drag (such as on aircraft and cars) and acoustic noise levels. Lift forces can be controlled by either controlling separation of the airflow at high angles of attack or controlling the circulation of the flow around an airfoil. Drag can be controlled by the moving of boundary layer transition points, and again by controlling separation. Acoustic noise can be controlled by changing the vortical features of a flow, for example by modifying of turbulent structures near the trailing edges of aerodynamic surfaces.

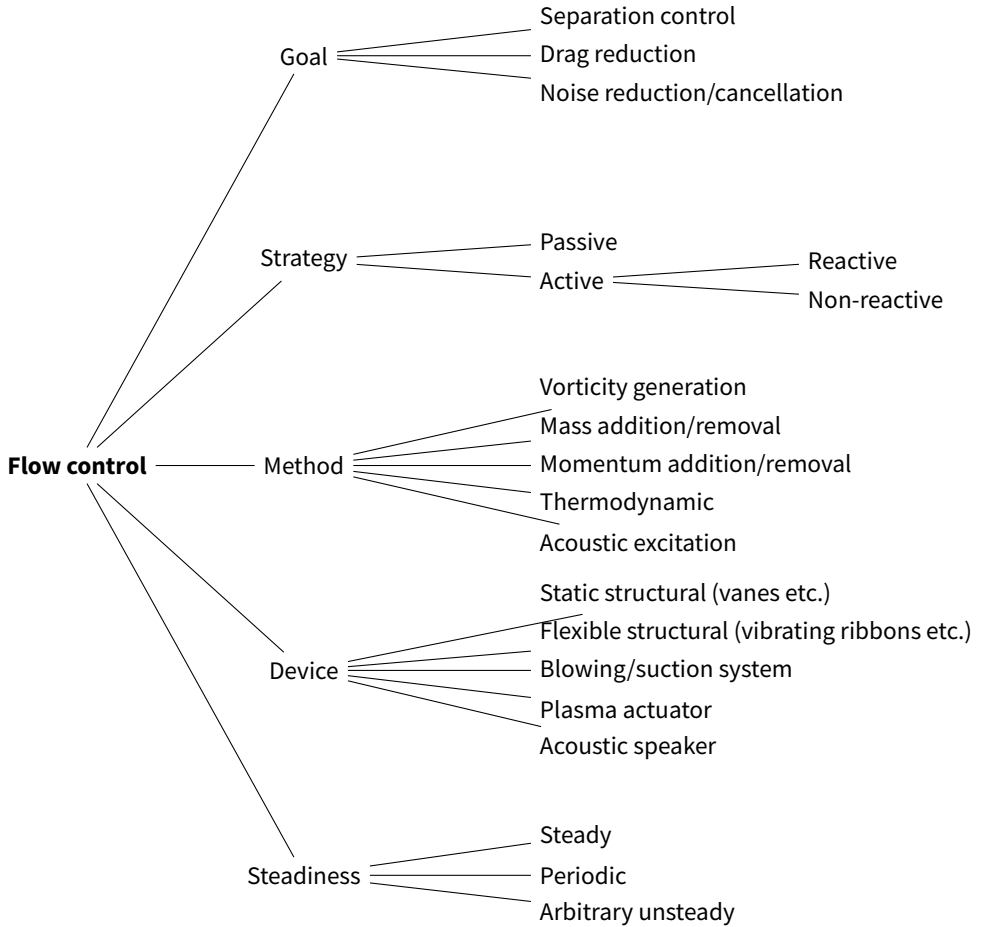


Figure 2.1: Classification of flow control

The properties of a flow can be changed using either *passive* or *active* strategies. Passive strategies do not introduce additional motion into the flow, while active strategies do. Passive strategies are generally simpler structurally and more reliable. Active strategies, on the other hand, are more expensive (in terms of energy, and usually in terms of device complexity and costs), but they generally allow for a larger degree of control, and are more easily adapted to the different flow conditions. Flow control strategies which use information about the flow state obtained from sensors (pressure transducers, hot wire velocity probes etc.) to change parameters of the control are called *reactive* flow control strategies.

Further classifications can be made by the method used and the device employed to achieve it (several examples are shown in [Figure 2.3](#)). Flow control can

be implemented using static structural devices, usually located on the surface of an aerodynamic object. These interact with the flow to change its properties. Examples of such structural devices include vanes, channels, ribbons, and ramps. Static devices are normally only effective for a limited range of flow conditions, which presents a disadvantage. On the other hand, they have the advantage of having no moving parts. This allows for better reliability, lower complexity and lower costs. An alternative is to use movable structural devices, with a generally higher, but still often limited, degree of adaptability to specific flow conditions.

Another type of the device is the *actuator*. Actuators are devices designed specifically to bring in additional types of motion into the flow. Such effects can be achieved by moving the parts of the object itself or by applying external forces to the flow medium (such as electric forces in plasma actuators).

A last type of device includes those which add or remove mass from the flow, such as blowing and suction devices. Apart from mass, these add or remove momentum, changing the velocity profile of boundary layers and other flow structures. Adding high-momentum fluid or removing low-momentum fluid makes velocity profiles fuller and helps boundary layers to overcome adverse pressure gradients, preventing separation and transition.

Finally, flow control techniques can be classified by whenever they are steady or unsteady. With steady flow control, the input to the base flow remains constant in time. With unsteady flow control, the input is non-constant, and can be either periodic or non-periodic. Periodic flow control is typically targeted on exciting natural modes of motion in the flow, for example instability modes in boundary or shear layers [23, 27]. This makes periodic flow control methods especially effective in unstable flows, where they can excite instability modes and cause flow breakup to occur earlier than happens naturally. Examples include methods which excite *Tollmien-Schlichting instability waves* in a boundary layer to promote transition. In such applications the frequency of the actuation is selected to coincide with the frequency of the targeted mode. Another example is the use of periodic flow control methods to redistribute the turbulence spectrum towards specific frequencies, changing the acoustic noise emission.

Flow control examples

Vortex generators (vanes) Vane-type vortex generators create flow-wise vortices along the surface of the airfoil, improving mixing and making the average velocity profile fuller and more resistant to separation. They are typically installed in counter-directed pairs or in spanwise rows along the suction surface of the wing. Examples include the vanes on a Boeing 737 airliner in some variants, as shown in [Figure 2.2](#). Many types of STOL aircraft also use vane-type vortex generators.



Figure 2.2: Rows of vane-type vortex generators (indicated by arrows) installed on a surface of an airliner wing.

The advantages of vanes include the possibility of applying them to existing designs, along with their low weight, cost and complexity, and good reliability. On the other hand, presence of vanes on the surface of the wing produces additional drag at cruise flight conditions, where good performance at high lift and high angles of attack is not required.

Blowing One of the first methods of flow control implemented on real aircraft was blowing. In typical examples a steady high velocity jet is injected into the main flow. This is normally implemented using compressor-driven high pressure air, or bleed air from jet engines. The air is usually directed along the flow direction through a spanwise slit in the surface (Figure 2.3, A). The additional flow introduces momentum into the lower part of the boundary layer, making its profile fuller and thus more resistant to separation. Blowing is typically applied just upstream of the expected separation point, for example on the aft suction side of a wing or over a flap.

Blowing over flaps has been used in several aircraft designs to increase maximum lift coefficient during takeoff and landing. Examples include the Blackburn Buccaneer carrier jet fighter aircraft (Figure 2.4) and the Lockheed F-104 jet fighter aircraft (Figure 2.5), for which blown flaps were used to decrease the otherwise very high landing speed due to high wing loading. Another example is the Shin Meiwa PS-1 / US-1 flying boat aircraft, which also used blown flaps for a *STOL* (*short takeoff and landing*) capability.

It has been shown that the key aspect of the effect of blowing is not the added mass, but rather the added momentum [23]. Thus to describe the strength of the

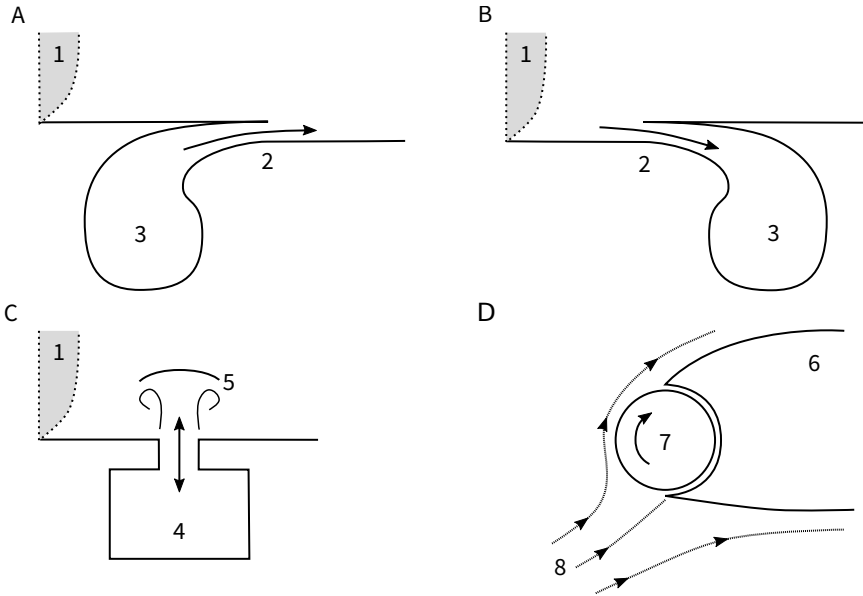


Figure 2.3: Flow control methods and devices: A — blowing (adding high-momentum flow into the lower part of the boundary layer); B — suction (removing low momentum flow from the boundary layer); C — synthetic jet / zero mass flow device (creating periodic jets in the boundary layer); D — rotating leading edge system. 1 — incoming boundary layer profile; 2 — blowing/suction slit; 3 — internal plenum; 4 — cavity with the oscillating membrane or a discharge; 5 — synthesized jet; 6 — wing; 7 — rotating cylinder; 8 — incoming freestream.

control, the momentum coefficient c_μ has been introduced, which is a ratio of the momentum added to the flow to the freestream momentum content of the unexcited flow:

$$c_\mu = \frac{\text{Added momentum}}{\text{Base flow momentum}} \quad (2.1)$$

Constant blowing has been shown to be efficient for $c_\mu > 5\%$ [23].

Although quite efficient for lift enhancement in takeoff and landing conditions, blowing has multiple drawbacks. Blowing systems are complex, heavy and bulky, and require significant power to operate (unless bleed air is available). The weight and bulk of blowing systems makes it particularly difficult to implement them redundantly, as required for safety reasons. Due to these drawbacks blowing systems have not yet seen widespread application, and remain mostly an experimental technology.

Suction Suction can be used both to prevent separation and delay transition. The idea of separation control via suction is to remove decelerated flow and thus

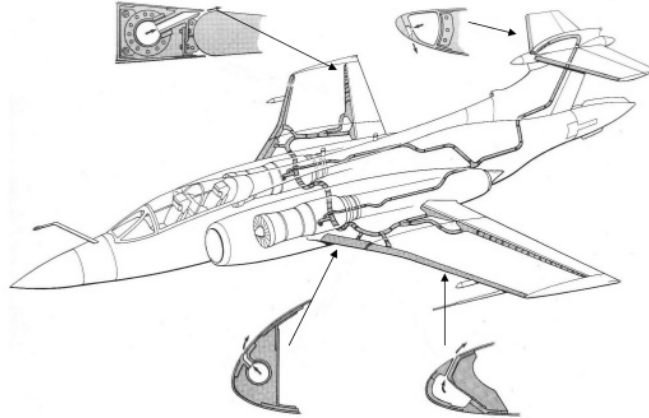


Figure 2.4: Flow control systems of the Blackburn Buccaneer jet fighter aircraft. Its bleed air ducts, blown leading edges and flaps are highlighted. [Image: *International Encyclopedia of Aviation*]

deflect higher speed flow towards the surface (Figure 2.3, B). Such systems have demonstrated remarkable effects on separation and transition, but have not found their way into mass production due to necessity of high flow rate air pumps, problems of contamination due to ingestion and the complexity of routing the exhaust air effectively. Several experimental aircraft using such technology have been built but none have entered production.

Zero mass flow and oscillating devices Zero mass flow devices, also known as *synthetic jets* (Figure 2.3, C), operate using fluid itself as an actor, but in a way that induces no net mass flow. This normally means that the flow is oscillating in periodic fashion, having phases of blowing and suction. Starting with free shear layer experiments carried out in 1970s, it has been found that periodic blowing helps to prevent separation even without mean mass flow, which eliminates the need for special compressors or the feeding of bleed air. Oscillating mechanical devices can also provide zero mass flow periodic excitation. This includes devices such as oscillating flaps or vibrating strings.

Surface motion Another method for boundary layer control is surface motion. Generally it involves the parts of the model moving with approximately the same velocity as freestream flow, thus eliminating the boundary layer. Examples of this technique include rotating cylinders on leading (Figure 2.3, D) and trailing edges, and moving floors in wind tunnels for car aerodynamic measurements.

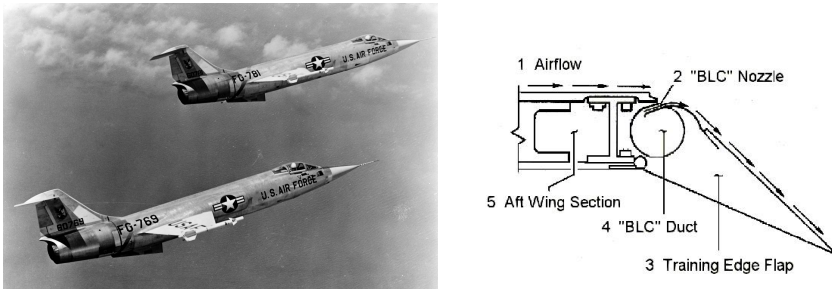


Figure 2.5: Left: a pair of Lockheed F-104A jet fighter aircraft in flight, showing their small wing areas. These aircraft used blowing flaps (right) to keep landing speeds reasonable. Image: USAF.

Acoustic excitation Using sufficient acoustic excitation, it is possible to excite Tollmien-Schlichting (TS) instability waves within a boundary layer. This delays separation, since turbulent boundary layers are less susceptible to separation than laminar ones. The effectiveness of acoustic excitation has been demonstrated on the large variety of airfoils from flat plates to 17% thick airfoils, reaching a maximum of 40% lift coefficient increase (but not in C_{Lmax}) [23]. The Reynolds numbers for which this has been demonstrated have been moderate, in the range of 0.2-0.5 million. The key parameter of such a periodic flow phenomena is *reduced frequency* F^+ also known as *Strouhal number*

$$St = \frac{fl}{U} \quad (2.2)$$

where f is a frequency of periodic motion, l is a characteristic length scale, and U is a characteristic velocity (typically equal to freestream velocity U_∞ for external flows). In the mentioned experiments St was in range of 1 to 100. Although the lift increases can be significant, there are several drawbacks. First, the sound level needed to obtain such an effect is extremely high (up to 156 dB). Second, there is evidence that in the experiments some modes of the flow of the wind tunnel itself have been excited, which makes the applicability of these results to free flight conditions questionable. An additional concern are the Reynolds numbers in these experiments, which are not high enough for realistic applications.

Plasma flow control

Flows can also be controlled using plasma effects. The advantage of using plasma is that it allows flow interactions at a distance, not only near the surface of the aerodynamic body. Plasma actuators can be made to be very thin, which has the

advantage of lower drag than would be introduced by other control devices. This is in sharp contrast to vane type vortex generators, for example, which require direct contact with the flow they control, creating both additional parasite and induced drag.

The first applications of plasma for flow control were in attempts to decrease supersonic drag of missiles, launch vehicles and hypersonic aircraft [19, 22, 62]. The idea was to create a “plasma ball” in front of the bluff body using microwaves, laser discharge, or a counter-flow plasma jet. In [22], plasma was used to change the properties of a bow shock, reducing wave drag. Researchers came to the conclusion that in this application the main effect is intensive gas heating, which leads to an increase in the local speed of sound and thus a decrease in local *Mach number*:

$$Ma = \frac{v}{c} \quad (2.3)$$

where v is the local flow velocity and c is the local speed of sound. Although considered very promising by researchers, this technique has not found any practical use, mainly due to very high power required to create a plasma ball, and the complexity of the required equipment (such as a powerful infrared laser or inductive electromagnetic transmitter).

Plasma actuators

A more practical version of plasma flow control can be achieved using *plasma actuators*. This technology has recently attracted great interest and has been rapidly developed. A common property of plasma actuators is the use of relatively low energy discharges to create plasma. The possible applications of plasma actuators include separation control, the control of skin friction (there are results both in increasing and decreasing skin friction), the tripping of boundary layers, and trailing edge noise reduction.

The most common way to create plasma for aerodynamic flow applications is by using barrier discharges. In this technology, a high voltage is applied to a system of two electrodes in shape of conductive strips, separated by a layer of insulating dielectric material. Discharges start on the edge of the exposed electrode and propagate along the surface of dielectric towards and above the covered electrode [4]. This type of discharge is called *Dielectric Barrier Discharge* or just *DBD*.

The dielectric plays an important role by not allowing the circuit to close, preventing current from flowing directly from one electrode to another. This gives several advantages. When no dielectric is used and the voltage exceeds certain threshold, the resistance of the gas between the electrodes becomes low due to

ionization (*electric breakdown*) and the energy is spent heating the electrodes. In contrast, in the presence of a dielectric layer all of the energy is put into the gas.

The dielectric barrier also keeps the discharge more uniform. In the absence of the dielectric, localized electric breakdown occurs (usually in one point due to inevitable tiny irregularities in the actuator), and all the charge will drain through the conductive channel preventing the discharge in other places of the actuator. This leads quickly to overheating and damage to the electrodes and surrounding materials. In contrast, when a dielectric is used the charge cannot drain through such a channel. In fact, uniform discharges have been demonstrated on DBD plasma actuators as long as 6 m.

DBD plasma actuators are further classified by the kind of electric signal they are fed with. The two classes are AC-DBD, using relatively low frequency alternating current, and NS-DBD, using high voltage pulses of nanosecond-scale duration. Although similar in construction, these two types demonstrate different properties and are believed to have different mechanisms of flow interaction. Both AC and NS DBD actuators are described in more detail below.

AC-DBD plasma actuators

AC-DBD plasma actuators make use of voltages applied with a periodic waveform at relatively low frequencies. The amplitudes used are typically on the order of several kilovolts to tens of kilovolts, with frequencies on the order of 10 kHz. When the instantaneous voltage exceeds the breakdown voltage, the discharge starts from the edge of the exposed electrode and propagates along the surface of the dielectric above the covered electrode. Since the voltage increases slowly relative to the time scale of discharge propagation, and the breakdown voltage is not perfectly uniform along the actuator, the discharge does not occur simultaneously along the whole actuator. This can be observed in current measurements as multiple peaks spread over time, as shown in [32]. After the discharge, the air is in an ionized state, forming a conductive sheet above the dielectric surface, increasing its capacitance [34]. At the same time, the electric field between electrodes is still present, which pulls the charged particles in the medium (positive ions and electrons) in opposite directions. This represents a volumetric body force acting upon the ionized air. The ions efficiently transfer their momentum to neutral molecules via collisions, setting the air into motion [10]. In experiments, the result has been observed as a jet along the surface, and been given the name “ionic wind”.

During the next half-period, the similar process occurs, but with opposite polarity. This creates a body force in the opposite direction, leading to a “push-pull” effect [10, 20, 31]. Forces acting in opposite directions during half-periods

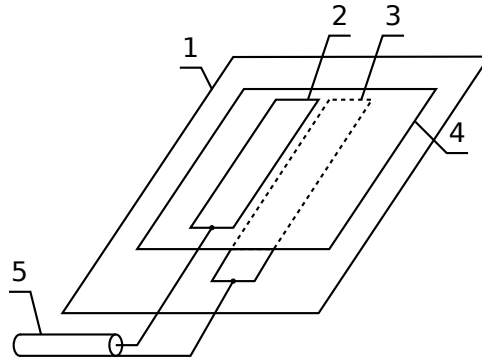


Figure 2.6: Typical layout of a NS-DBD plasma actuator. 1 — surface; 2 — exposed electrode; 3 — covered electrode; 4 — dielectric layer; 5 — coaxial cable from the generator.

partially cancel each other, although not completely, due to asymmetry of the discharge. This often represents a disadvantage for the flow control effects. Thus some researchers have used asymmetrical waveforms to mitigate this cancellation. Sine waves with a bias, sawtooth and other waveforms have proven to be more efficient than a simple sine wave in many situations [32].

It has been shown in [30] that the time-averaged effect of AC-DBD actuators can be modeled as a volumetric body force. In this reference, the magnitude and spatial distribution of the body force was determined using the PIV (particle imaging velocimetry) measurements of the velocity field in the jet [20, 30, 31].

The advantage of AC-DBD plasma actuators is that they generate a directly controllable body force. This can be used, for example, to affect the growth of the Tollmien-Schlichting waves in a boundary layer [21]. Using an adaptive electronic controller provided with a signal from a pressure transducer or a hot wire probe, researchers have shown a feasibility of suppression of T-S waves, thus delaying boundary layer transition. This in turn leads to drag reduction, a very desired effect. When tuned differently, the same setup can be used to excite instabilities and promote transition. With this effect, AC-DBD plasma actuators have been used to eliminate flow separation on an airfoil or a flap [37].

NS-DBD plasma actuators

This thesis focuses mostly on the second type of plasma actuators, the nanosecond dielectric barrier discharge (NS-DBD) actuator. The NS-DBD actuator uses extremely short high-voltage pulses, typically 10–50 ns long with voltage of 5–20 kV. The pulse repetition rate can be changed over a wide range, from zero up to 10 kHz. Nanosecond plasma actuators were first studied about 10 years ago, coincident with the introduction of suitable pulse generators.

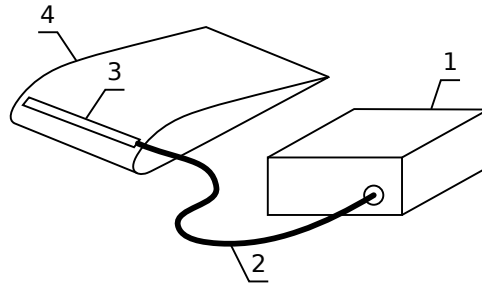


Figure 2.7: Typical system for NS-DBD plasma actuation. 1 — high voltage nanosecond pulse generator; 2 — coaxial cable; 3 — NS-DBD plasma actuator; 4 — aerodynamic shape.

Most researchers use a similar layout for NS-DBD actuators (Figure 2.6), as well as the for the remaining setup (Figure 2.7). A typical actuator consists of several dielectric (typically Kapton) and conductive (typically adhesive copper foil) layers. On the very bottom, an optional protective dielectric layer can be used which is applied directly to the aerodynamic structure (Figure 2.6, 1). The purpose of this layer is to protect the structure from electric breakdown, overheating and burning. This is not required if the surface of the structure is dielectric, can withstand the voltages applied and has good enough heat conductivity. It can also be omitted in the case of electrically conductive structure where the surface of the structure itself can act as the electrode. In such a case, however, the performance can be reduced due to higher electric capacity between electrodes.

Above the protective layer comes the covered electrode (Figure 2.6, 3), followed by the main dielectric layer (Figure 2.6, 4). The main dielectric layer plays a principal role in the formation of the discharge. The thickness of the layer should be chosen to withstand the applied voltage (typically by choosing the thickness and number of layers of Kapton). Above the dielectric layer there is an exposed electrode (Figure 2.6, 2). It consists of a adhesive copper strip parallel to the covered electrode. At this point the layouts used by different researchers differ. Electrodes can overlap, or the edges of the electrodes can coincide, or there can be a gap between electrodes. There can also be a difference in the polarity of the applied pulses. Researchers who have compared the influence of polarity have shown some differences in the net results [15, 26, 50].

The length of the pulses (tens of nanoseconds) corresponds to spatial wavelengths of $\lambda \approx 3\text{ m}$. Generating high voltage pulses which are so short is a challenging task. Several different types of generators can be used to provide the high-voltage pulses. Among the most flexible, reliable and best performing are solid state high-voltage generators which use technology based on step recovery

diodes (SRD) [40]. Taking into account the higher frequencies required for the sharp edges of the pulse, ultra-high-frequency approaches for transmission and measurement are required.

There are two main methods of connecting generator to the actuator. The first method is to use a direct connection, where wires connecting the generator to the actuator are made as short as possible. Any loops in the wiring should be avoided, as these can act as antennas emitting electromagnetic noises which can affect other equipment. In addition, if the loop has a significant inductance, then the pulse can experience significant decay. The second method is to use a long coaxial cable. If the cable is longer than the pulse, it decouples the actuator from generator. The generator thus feels a pure active load equal to the cable impedance. This type of connection make it easier to measure actual pulse energy, because knowing impedance Z and measuring voltage, the incident pulse energy can be calculated as

$$E = \int \frac{U^2}{Z} dt. \quad (2.4)$$

The reflected pulse can also be measured if the cable is long enough, and the pulses are separated in time. This allows calculation of the energy input to the actuator. Instead of (or in addition to) voltage, the current can also be measured. For that, a back current shunt or current probe can be utilized. A back current shunt is small (in order of 0.1Ω) resistor installed into a cut in the shield of the cable. The voltage over the resistor is proportional to the current flowing through the shield which is equal but opposite to the current of the pulse.

[63] gives an extensive overview of numerous experiments with NS-DBD actuators. It includes a review of data on controlling boundary layer attachment by a nanosecond plasma actuator with high-voltage pulsed-periodic nanosecond excitation. It also presents the first attempt to study the mechanisms of nanosecond plasma actuation. First, the ionic wind effect was studied. It was found that DBD actuator induced gas velocities have near-zero values for nanosecond pulses, which suggests that ionic wind plays minor if any role in NS-DBD separation control. The measurements also showed overheating in the discharge region with fast ($\tau \approx 1 \mu\text{s}$) thermalization of the plasma input energy. The mean values of such heating of the plasma layer were shown to reach 70, 200, and 400 K for 7, 12, and 50 ns pulse durations, respectively.

As a result of each pulse a shock wave together with a secondary vortex were introduced into the main flow (Figure 2.9). Both the intensity of the shock wave and its propagation speed were measured, and images depicting its propagation pattern were obtained using a Schlieren technique. From numerical simulations used to reconstruct the spatial distribution of the energy deposition from the shape of wave front, two regions were identified. The first near the edge of the



Figure 2.8: Separation elimination with NS-DBD plasma actuators. Left: actuation off; right: actuation on.

exposed electrode with stronger heating, and the second spanning rest of the area with somewhat lower heating. Pulsed-periodic vortical disturbances were found to cause efficient transverse momentum transfer into the boundary layer and promote flow attachment to the airfoil surface. The NS-DBD experiments showed effective control of boundary layer separation, and thus lift and drag. There was also acoustic noise reduction in the Mach number range of 0.05 to 0.85. The main mechanism of the NS-DBD was summarized as its energy transfer to and heating of the near-surface gas layer, which is accompanied by pulse-periodic vortex movement which stimulates redistribution of the main flow momentum.

The electrical properties of the discharge, such as voltage/current shapes and energy input, were also measured during the experiments, and high speed imaging of the discharge was performed. The discharge was observed to consist of two phases. The first occurring on rising edges (when dielectric surface is charged) and falling edges (when it is discharged) of the voltage pulse. The spatial structure of the discharge was not found to be perfectly uniform, but to instead consist of channels with a pitch on the order of 0.5 mm. Additionally, some differences in the discharge structure between cases with positive and negative pulses were observed. As far as vertical structure goes, optical measurements showed that at atmospheric pressure the maximum emission intensity occurs at a height of 0.2–0.5 mm, depending on the voltage. The spatial distribution of the deposited energy was measured using emissions of the second positive system of nitrogen molecules N_2 . Dependency on the discharge frequency was studied, which showed that the maximum efficiency occurs at reduced frequencies of $F^+ \approx 1$, based on the chord length and free stream velocity.

Aerodynamic measurements were carried out using the C16 airfoil (symmetrical with thickness of 16%), with a NS-DBD actuator on the leading edge. The flow velocity was 15–25 m/s, with a model chord of 0.5 m and span of 1 m. In stall

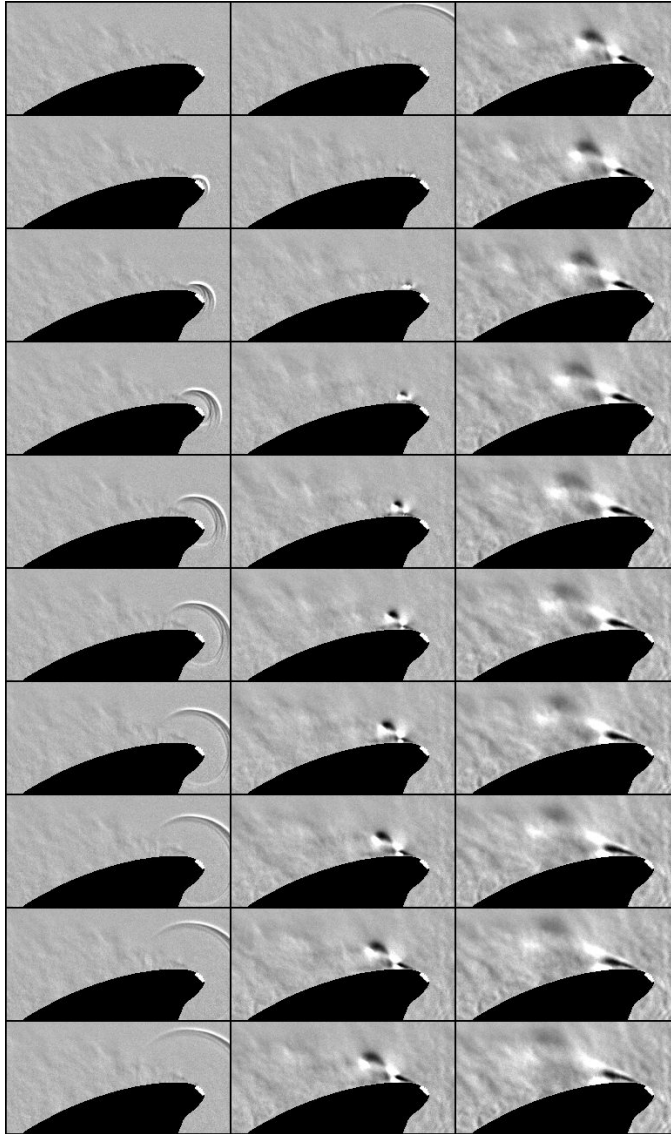


Figure 2.9: Sequence of schlieren images showing compression waves and coherent vortical structures generated by the NS-DBD plasma actuator. Left column, from top to bottom: formation and propagation of compression waves, $8\mu\text{s}$ per frame; middle and right columns: formation of coherent vortex structures, $80\mu\text{s}$ per frame. [13]

conditions (at an angle of attack of 22 degrees) lift increases of up to 30% and drag decrease of 45% were observed.

In the paper [63] an effect of NS-DBD actuation on acoustic noise level has been observed. A model has been placed in high speed flow ($M = 0.85$), and pressure fluctuations in the wake of the model have been measured. This observation suggests the capability of the NS-DBD actuator to modify turbulence structure in the turbulent boundary layer. It is assumed that the actuator can organize the vorticity in coherent way, with specific temporal and spatial frequencies, thus modifying the sound emitting characteristics of the flow at the trailing edge. However, there were no more experimental or theoretical studies on this topic.

Summary

Plasma actuators represent a promising alternative to current flow control techniques. It has been demonstrated that they are able to postpone laminar leading edge separation, improving the performance of airfoils. The effects of NS-DBD actuation have been observed using tuft visualization, schlieren imaging, PIV (particle imaging velocimetry) and force measurements. The results of the experiments demonstrate that NS-DBD plasma actuation is capable of eliminating leading edge separation [13, 42]. Promotion of early boundary layer transition and separation delay have also been observed. In perspective, NS-DBD plasma actuators can replace or be used together with more complex systems, like leading edge slats. Plasma actuators possess a unique set of properties, making them attractive for separation control applications, namely:

- No moving parts;
- Small size and low weight;
- Low energy consumption;
- The possibility to retrofit them to existing designs;
- Controllability and fast response.

In addition, there are studies indicating applicability of plasma actuators for other tasks, such as transition control, dynamic load control and acoustic noise control. The performance and effectiveness NS-DBD plasma actuators, however, remains not studied exhaustively. All this makes NS-DBD plasma actuators an important topic to study.

Chapter 3

NS-DBD plasma actuators

This chapter gives an introduction to the physical characteristic of NS-DBD (nanosecond dielectric barrier discharge) plasma actuators, and discusses their physical principles of operation, layout, and operation parameters. Practical ranges of their parameters are defined, and design limitations, both physical and technical, are identified. Electrical measurements are presented to establish important properties of the actuator, including the energy input per pulse, effective length, and minimum operational voltage. These are crucial for both modeling and application.

The NS-DBD plasma actuator is a device which produces electrical discharge, a physical phenomenon occurring when electric field in a gap between two electrodes exceeds the breakdown value for the medium filling the gap [60]. During discharge, the electric field ionizes the particles of the medium, creating plasma. This forms a conductive *plasma channel* between the electrodes. Within the channel, electrical energy is transferred to potential energy of ionization, excited states of electrons in atoms and molecules, and rotational and vibrational degrees of freedom of molecules. The process itself is extremely complex, consisting of many individual reactions between neutral molecules, positive and negative ions and electrons. Eventually, these excited states and degrees of freedom relax, transferring the energy to translational degrees of freedom, or in other words, heat.

In NS-DBD plasma actuators, discharges are created by applying high voltage electric pulses to a pair of parallel copper foil strips acting as electrodes, as shown in [Figure 3.1](#). These electrodes are separated by a layer of dielectric, which prevents a short circuit. This makes the discharges DBD (dielectric barrier

discharges), limiting electric currents and preventing the rapid erosion of the electrodes. The result is an extremely fast and efficient means of depositing energy into the flow.

The physics of plasma

Plasma is special state of matter, which does not consist of neutral particles such as atoms and molecules, but instead of charged particles: ions (positive and negative) and free electrons. In the past it was believed to be a fourth state of matter, along with solid, liquid and gaseous states, but recent experiments [69] revealed that “liquid plasma” can exist as well. This makes plasma more a property of the medium rather than separate state. There are several different types of plasmas, distinguished by their temperature, density and the way they are produced. The kind of plasma produced in NS-DBD actuators is high-pressure (at atmospheric pressure) low-temperature ($< 1000\text{ K}$) plasma.

In the simplest case, plasma can be represented as a mixture of electrons, ions, and neutral gas [36, 60]. Because of their very low mass and relatively little interaction with other particles, electrons have their own temperature and concentration. The concentration of ions may be assumed to be the same as that of electrons. In the simplest case it can be assumed there are only singly-charged ions, which implies:



$$n_i = n_e \quad (3.2)$$

where M is some molecule, n_i is the particle density of positive ions, and n_e the is particle density of electrons.

More complex models consider more species (all the species of the original gas, their most significant excited states, all kinds of ions (negative and positive, singly and multiply charged)), and many reactions between them, including ionization, recombination, chemical reactions, excitation, and relaxation [5, 17, 28, 29, 43, 73]. An example of a set of reactions used for discharge simulations is shown in Figure 3.3 (only 52 of total 72 reactions are shown). Each reaction contributes a term to the time evolution equations for species concentrations

$$\frac{\partial n}{\partial t} + \mathbf{v}\nabla n = D\Delta n + \sum P_i \quad (3.3)$$

where $n(t, x)$ is the volumetric particle density, \mathbf{v} is the convection speed, D is a diffusion coefficient and P_i is the particle production/consumption rate due to reaction i . For example, if there is a reaction



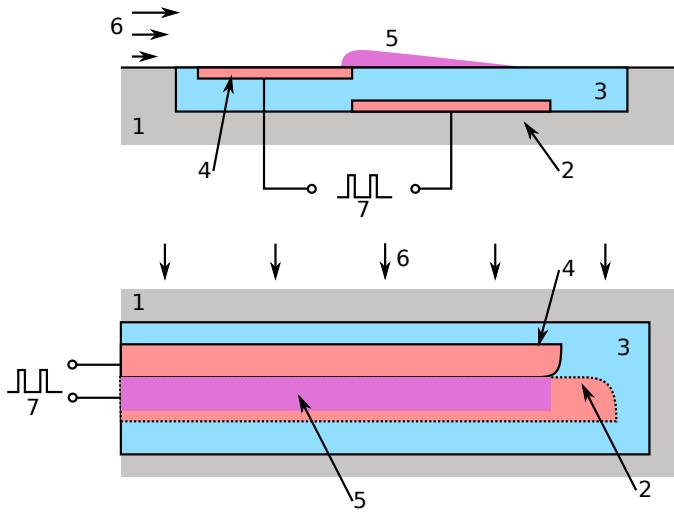


Figure 3.1: Layout of an NS-DBD plasma actuator, cross-section and top view (1 — substrate, 2 — covered electrode, 3 — dielectric layer, 4 — exposed electrode, 5 — discharge (plasma) volume, 6 — flow direction, 7 — electric pulse input from high-voltage pulse generator).

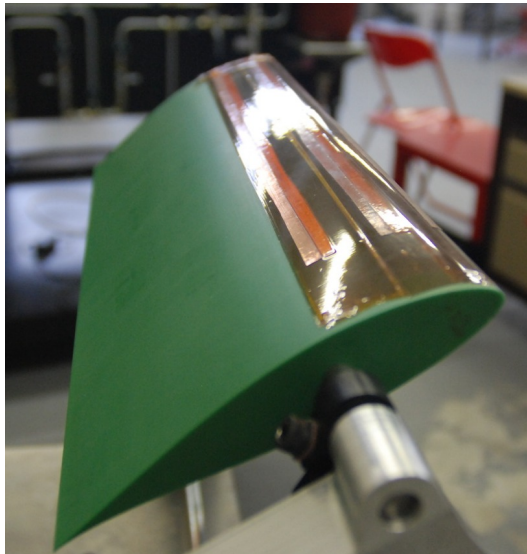


Figure 3.2: Three NS-DBD plasma actuators installed on a surface of a model airfoil.

No	Reaction	Rate coefficient ($\text{cm}^3 \text{s}^{-1}$, $^* \text{cm}^6 \text{s}^{-1}$)
<i>Electron-impact excitation and dissociation</i>		
(R1)	$e + \text{N}_2 \rightarrow e + \text{N}_2(A^3\Sigma_u^+)$	$f(E/N)$
(R2)	$e + \text{N}_2 \rightarrow e + \text{N}_2(B^3\Pi_g)$	$f(E/N)$
(R3)	$e + \text{N}_2 \rightarrow e + \text{N}_2(a'^1\Sigma_u^-)$	$f(E/N)$
(R4)	$e + \text{N}_2 \rightarrow e + \text{N}_2(C^3\Pi_u)$	$f(E/N)$
(R5)	$e + \text{N}_2 \rightarrow e + \text{N}_2(\Delta E = 13 \text{ eV})$ $\text{N}_2(\Delta E = 13 \text{ eV}) \rightarrow \text{N}(\text{}^4\text{S}) + \text{N}(\text{}^2\text{D}) + \varepsilon_5$	$f(E/N)$
(R6)	$e + \text{O}_2 \rightarrow e + \text{O}_2(A^3\Sigma_u^+, C^3\Delta_u)$ $\text{O}_2(A^3\Sigma_u^+, C^3\Delta_u) \rightarrow \text{O}(\text{}^3\text{P}) + \text{O}(\text{}^1\text{D}) + \varepsilon_6$	$f(E/N)$
(R7)	$e + \text{O}_2 \rightarrow e + \text{O}_2(B^3\Sigma_u^-)$ $\text{O}_2(B^3\Sigma_u^-) \rightarrow \text{O}(\text{}^3\text{P}) + \text{O}(\text{}^1\text{D}) + \varepsilon_7$	$f(E/N)$
(R8)	$e + \text{O}_2 \rightarrow e + \text{O}_2^*$ $\text{O}_2^* \rightarrow \text{O}(\text{}^3\text{P}) + \text{O}(\text{}^1\text{S}) + \varepsilon_8$	$f(E/N)$
<i>Electron-impact ionization</i>		
(R9)	$e + \text{N}_2 \rightarrow 2e + \text{N}_2^+$	$f(E/N)$
(R10)	$e + \text{O}_2 \rightarrow 2e + \text{O}_2^+$	$f(E/N)$
<i>Quenching of excited particles</i>		
(R11)	$\text{N}_2(A^3\Sigma_u^+) + \text{O}_2 \rightarrow \text{N}_2 + 2\text{O}(\text{}^3\text{P}) + \varepsilon_{11}$	1.7×10^{-12}
(R12)	$\text{N}_2(A^3\Sigma_u^+) + \text{O}_2 \rightarrow \text{N}_2 + \text{O}_2(b^1\Sigma_g^+, v)$	7.5×10^{-13}
(R13)	$\text{N}_2(A^3\Sigma_u^+) + \text{H}_2\text{O} \rightarrow \text{N}_2 + \text{OH} + \text{H} + \varepsilon_{13}$	5×10^{-14}
(R14)	$\text{N}_2(A^3\Sigma_u^+) + \text{N}_2(A^3\Sigma_u^+) \rightarrow \text{N}_2(v) + \text{N}_2(B^3\Pi_g)$	7.7×10^{-11}
(R15)	$\text{N}_2(A^3\Sigma_u^+) + \text{N}_2(A^3\Sigma_u^+) \rightarrow \text{N}_2(v) + \text{N}_2(C^3\Pi_u)$	1.6×10^{-10}
(R16)	$\text{N}_2(A^3\Sigma_u^+) + \text{O}(\text{}^3\text{P}) \rightarrow \text{N}_2(v) + \text{O}(\text{}^1\text{S})$	3.0×10^{-11}
(R17)	$\text{N}_2(B^3\Pi_g) + \text{O}_2 \rightarrow \text{N}_2 + 2\text{O}(\text{}^3\text{P}) + \varepsilon_{17}$	3.0×10^{-10}
(R18)	$\text{N}_2(B^3\Pi_g) + \text{N}_2 \rightarrow \text{N}_2(A^3\Sigma_u^+) + \text{N}_2(v)$	1.0×10^{-11}
(R19)	$\text{N}_2(B^3\Pi_g) + \text{H}_2\text{O} \rightarrow \text{N}_2 + \text{OH} + \text{H}$	3×10^{-10}
(R20)	$\text{N}_2(a'^1\Sigma_u^-) + \text{O}_2 \rightarrow \text{N}_2 + \text{O}(\text{}^3\text{P}) + \text{O}(\text{}^1\text{D}) + \varepsilon_{20}$	2.8×10^{-11}
(R21)	$\text{N}_2(a'^1\Sigma_u^-) + \text{N}_2 \rightarrow \text{N}_2(v) + \text{N}_2(v)$	2.0×10^{-13}
(R22)	$\text{N}_2(a'^1\Sigma_u^-) + \text{H}_2\text{O} \rightarrow \text{N}_2 + \text{OH} + \text{H}$	3×10^{-10}
(R23)	$\text{N}_2(C^3\Pi_u) \rightarrow \text{N}_2(B^3\Pi_g) + h\nu$	$3.0 \times 10^7 \text{ s}^{-1}$
(R24)	$\text{N}_2(C^3\Pi_u) + \text{O}_2 \rightarrow \text{N}_2 + \text{O}(\text{}^3\text{P}) + \text{O}(\text{}^1\text{S}) + \varepsilon_{24}$	3.0×10^{-10}
(R25)	$\text{N}_2(C^3\Pi_u) + \text{N}_2 \rightarrow \text{N}_2(a'^1\Sigma_u^-) + \text{N}_2(v)$	1.0×10^{-11}
(R26)	$\text{N}_2(C^3\Pi_u) + \text{H}_2\text{O} \rightarrow \text{N}_2 + \text{OH} + \text{H}$	3×10^{-10}
(R27)	$\text{N}_2(\Delta E = 13 \text{ eV}) + \text{O}_2 \rightarrow \text{N}_2 + \text{O}(\text{}^3\text{P}) + \text{O}(\text{}^1\text{S}) + \varepsilon_{27}$	2.8×10^{-11}
(R28)	$\text{N}_2(\Delta E = 13 \text{ eV}) + \text{N}_2 \rightarrow \text{N}_2(a'^1\Sigma_u^-) + \text{N}_2$	2.0×10^{-13}
(R29)	$\text{N}_2(\Delta E = 13 \text{ eV}) + \text{H}_2\text{O} \rightarrow \text{N}_2 + \text{OH} + \text{H}$	3×10^{-10}
(R30)	$\text{O}(\text{}^1\text{D}) + \text{N}_2 \rightarrow \text{O}(\text{}^3\text{P}) + \text{N}_2(v) + \varepsilon_{30}$	$1.8 \times 10^{-11} \times \exp(107/T)$
(R31)	$\text{O}(\text{}^1\text{D}) + \text{O}_2 \rightarrow \text{O}(\text{}^3\text{P}) + \text{O}_2(b^1\Sigma_g^+, v)$	$2.6 \times 10^{-11} \times \exp(67/T)$
(R32)	$\text{O}(\text{}^1\text{D}) + \text{H}_2\text{O} \rightarrow \text{OH} + \text{OH} + \varepsilon_{32}$	2.2×10^{-10}
(R33)	$\text{O}(\text{}^1\text{S}) + \text{O}_2 \rightarrow \text{O}(\text{}^3\text{P}) + \text{O}_2(A, c, C)$	$3.0 \times 10^{-12} \times \exp(-850/T)$
(R34)	$\text{O}(\text{}^1\text{S}) + \text{O}_2 \rightarrow \text{O}(\text{}^1\text{D}) + \text{O}_2(v)$	$1.3 \times 10^{-12} \times \exp(-850/T)$
(R35)	$\text{O}(\text{}^1\text{S}) + \text{N}_2 \rightarrow \text{products}$	$5.0 \times 10^{-17} \times \exp(-850/T)$
(R36)	$\text{N}(\text{}^2\text{D}) + \text{O}_2 \rightarrow \text{NO} + \text{O}(\text{}^3\text{P}) + \varepsilon_{36}$	$1.5 \times 10^{-12} \times (T/300)^{0.5}$
(R37)	$\text{N}(\text{}^2\text{D}) + \text{O}_2 \rightarrow \text{NO} + \text{O}(\text{}^1\text{D}) + \varepsilon_{37}$	$6 \times 10^{-12} \times (T/300)^{0.5}$
(R38)	$\text{N}(\text{}^2\text{D}) + \text{N}_2 \rightarrow \text{N}(\text{}^4\text{S}) + \text{N}_2$	6×10^{-15}
<i>Charge exchange and conversion</i>		
(R39)	$\text{N}_2^+ + \text{O}_2 \rightarrow \text{N}_2 + \text{O}_2^+ + \varepsilon_{39}$	$6 \times 10^{-11} \times \exp(300/T)^{0.5}$
(R40)	$\text{N}_2^+ + 2\text{N}_2 \rightarrow \text{N}_2^+ + \text{N}_2 + \varepsilon_{40}$	$5 \times 10^{-29} (^*)$
(R41)	$\text{O}_2^+ + 2\text{O}_2 \rightarrow \text{O}_2^+ + \text{O}_2 + \varepsilon_{41}$	$2.4 \times 10^{-30} (^*)$
(R42)	$\text{O}_2^+ + 2\text{N}_2 \rightarrow \text{O}_2^+ \text{N}_2 + \text{N}_2 + \varepsilon_{42}$	$0.9 \times 10^{-30} \times (300/T)^2 (^*)$
(R43)	$\text{N}_2^+ + \text{O}_2 \rightarrow 2\text{N}_2 + \text{O}_2^+ + \varepsilon_{43}$	2.5×10^{-10}
(R44)	$\text{O}_2^+ \text{N}_2 + \text{N}_2 \rightarrow \text{O}_2^+ + 2\text{N}_2 + \varepsilon_{44}$	$1.1 \times 10^{-6} \times (300/T)^{5.3} \times \exp(-2357/T)$
(R45)	$\text{O}_2^+ \text{N}_2 + \text{O}_2 \rightarrow \text{O}_2^+ + \text{N}_2 + \varepsilon_{45}$	10^{-9}
(R46)	$\text{O}_2^+ + \text{H}_2\text{O} \rightarrow \text{O}_2^+ \text{H}_2\text{O} + \text{O}_2 + \varepsilon_{46}$	1.5×10^{-9}
(R47)	$\text{O}_2^+ \text{H}_2\text{O} + \text{H}_2\text{O} \rightarrow \text{H}_3\text{O}^+ + \text{OH} + \text{O}_2 + \varepsilon_{47}$	3×10^{-10}
(R48)	$\text{O}_2^+ + \text{H}_2\text{O} + M \rightarrow \text{O}_2^+ \text{H}_2\text{O} + M + \varepsilon_{48}$ $M: \text{N}_2, \text{O}_2, \text{H}_2\text{O}$	$2.8 \times 10^{-28} \times (300/T_i)^3 (^*)(p \rightarrow 0)$
(R49)	$\text{H}_2\text{O}^+ + \text{O}_2 \rightarrow \text{H}_2\text{O} + \text{O}_2^+ + \varepsilon_{49}$	4.3×10^{-10}
(R50)	$\text{N}_2^+ + \text{H}_2\text{O} \rightarrow \text{N}_2 + \text{H}_2\text{O}^+ + \varepsilon_{50}$	2.2×10^{-9}
(R51)	$\text{N}_2^+ + \text{H}_2\text{O} \rightarrow 2\text{N}_2 + \text{H}_2\text{O}^+ + \varepsilon_{51}$	2.2×10^{-9}
(R52)	$\text{H}_2\text{O}^+ + \text{H}_2\text{O} \rightarrow \text{H}_3\text{O}^+ + \text{OH} + \varepsilon_{52}$	1.8×10^{-9}

Figure 3.3: A part of a set of reactions used in [5] to simulate the energy conversion process in discharge.

then contribution to C's density would be proportional to product of the particle densities of A and B

$$P_C = kn_A n_B \quad (3.5)$$

where k is a *reaction constant*, which for chemical reactions typically depends on temperature through *Arrhenius equation*

$$k \sim Z \exp(E_a / k_B T) \quad (3.6)$$

where Z is a collision rate, E_a is activation energy of the reaction, k_B is Boltzmann's constant, and T is temperature.

For electrons, it is necessary to consider a distribution over energies, since the collision rate Z is strongly dependent on the electron energy via the *reaction cross-section* σ :

$$Z(E) = N_A \sigma(E) \overline{v'} \quad (3.7)$$

where $N_A = 6.02 \cdot 10^{23}$ is the Avogadro number and $\overline{v'}$ is the average relative velocity of colliding particles. The reaction cross-section is a parameter of a reaction or collision, such that the probability of the reaction is equal to the probability of a collision with a solid ball with cross-section σ . To account for this dependence, a *Boltzmann equation* for electrons is used, which describes the evolution of particle density in space-velocity variables

$$\frac{\partial f}{\partial t} + \mathbf{v} \cdot \nabla f + \frac{q\mathbf{E}}{m} \nabla_{\mathbf{v}} f = \left(\frac{\partial f}{\partial t} \right)_{\text{coll}} \quad (3.8)$$

where $f(t, \mathbf{x}, \mathbf{v})$ is a distribution density function, \mathbf{v} is the particle velocity, ∇ is the spatial gradient, q is particle charge, m is its mass, \mathbf{E} is electric field, $\nabla_{\mathbf{v}}$ is the gradient in velocity coordinates ($\nabla_{\mathbf{v}} f = \sum \mathbf{e}_i \partial f / \partial v_i$), and right hand side is a change of particle density due to collisions, including both elastic and non-elastic collisions (reactions) [60].

In the presence of boundaries, such as dielectric boundaries and surfaces of conductive electrodes, there are even more processes involved, such as accumulation of charge on the surface, photoemission and emission processes caused by electron and ion impacts [52, 65, 71].

The physics of discharges

A typical discharge consists of several phases, each having different properties [50, 60]. First is a *streamer* phase, in which avalanches of electrons propagate from the negative electrode (*cathode*) to the positive electrode (*anode*), ionizing the medium (Figure 3.4, B). Once a conductive plasma channel has bridged the

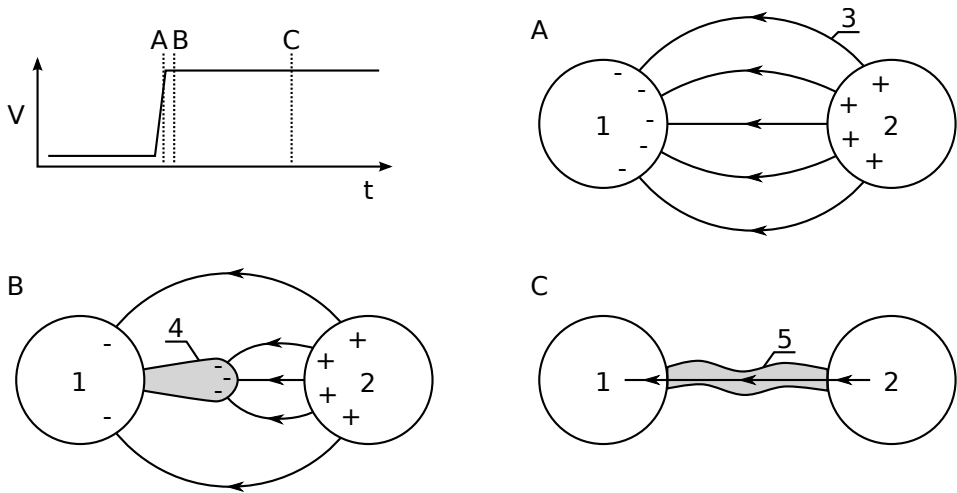


Figure 3.4: Discharge development: A — initial electric field between generic spherical electrodes; B — streamer phase; C — arc phase (current flows freely between electrodes). (1 — negative electrode (cathode), 2 — positive electrode (anode), 3 — electric field lines, 4 — streamer, 5 — plasma channel)

gap, current can flow between the discharges unobstructed, further increasing the ionization and temperature of the plasma channel (Figure 3.4, C). The current then rises to very high values. This is called the *arc phase*. The main difference between this phase and the streamer phase is the increased conductivity of the discharge channel [1]. During the streamer phase, the voltage across the gap is still high, the current is relatively low, and almost all electric energy is transferred to the discharge itself. During the arc phase, the conductivity of the discharge channel is very high (due to the high conductivity of ionized gas), making the current very high and voltage low. In this phase, most of the electric energy is dissipated in heating the electrodes themselves. Therefore, if high energy input into the medium between electrodes is desired, the streamer phase is more efficient than the arc phase.

Two solutions have been proposed to reduce the duration of the arc phase. One is to cover one of the electrodes with a layer of dielectric to prevent closing the circuit, and allow a high current to flow through the electrodes and the discharge gap (Figure 3.5). The second solution is to use shorter electric pulses. If we make the pulse duration just enough for a streamer to reach the other side of the gap, the inefficient arc phase of the discharge is eliminated. NS-DBD plasma actuators use both of these solutions to achieve high energy input to the medium.

After the discharge is ended, the energy stored in the plasma is converted to translational degrees of freedom of the molecules — a thermal form of energy.

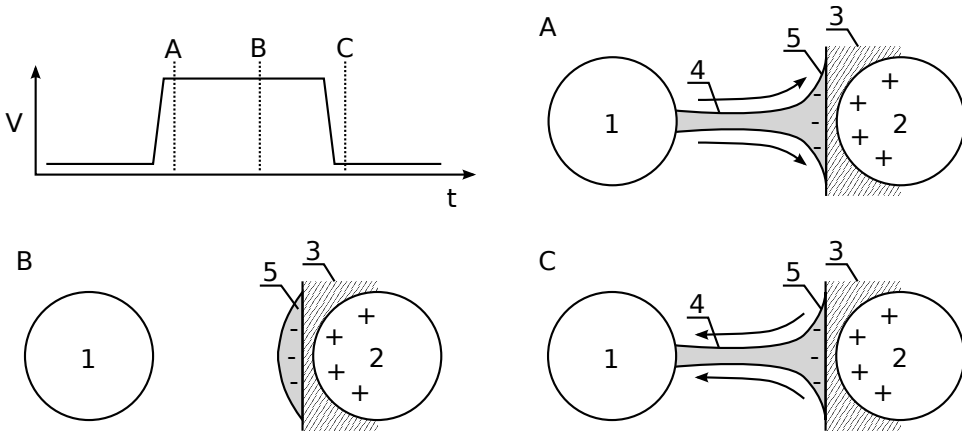


Figure 3.5: DBD discharge development in a generic spherical electrodes geometry: A — direct phase, the surface of the dielectric is charged by means of the discharge; B — “dark” phase (no discharge, the surface of the dielectric is charged); C — reverse phase (after the pulse has ended, the charge from the surface of the dielectric flows back to the electrode). (1 — negative electrode (cathode), 2 — positive electrode (anode), 3 — dielectric barrier, 4 — plasma channel, 5 — charged surface of the dielectric)

This happens via recombination (reattachment of the electrons to positive ions), relaxation (return to normal state of molecule from excited state) and other processes. The detailed mechanisms of such energy conversions are discussed in [5, 45, 68]. The plasma then recombines back to a neutral non-conductive gas.

The layout of NS-DBD actuators

Most researchers use a similar layout for NS-DBD plasma actuators, although the details can differ. NS-DBD plasma actuators normally consist of two long parallel electrodes, which are implemented as strips of copper foil (Figure 3.1). The electrodes are separated by a layer of dielectric material, although in the recent experiments [12] actuators with a semiconductive material (silicon) instead of dielectric one have been used. One of the electrodes is exposed to the flow, while the other remains covered. The discharge develops from the edge of the exposed electrode along the surface of the dielectric towards and above the covered electrode (Figure 3.6). NS-DBD actuators are normally applied to an aerodynamic surface in the span-wise direction. Figure 3.2 shows three actuators installed on a model airfoil used for a wind tunnel test. On one end the electrodes are connected to a high-voltage pulse generator by the means of high-voltage coaxial cable. The other end of the actuator is left unconnected.

The quality of manufacturing greatly affects the performance of the actua-

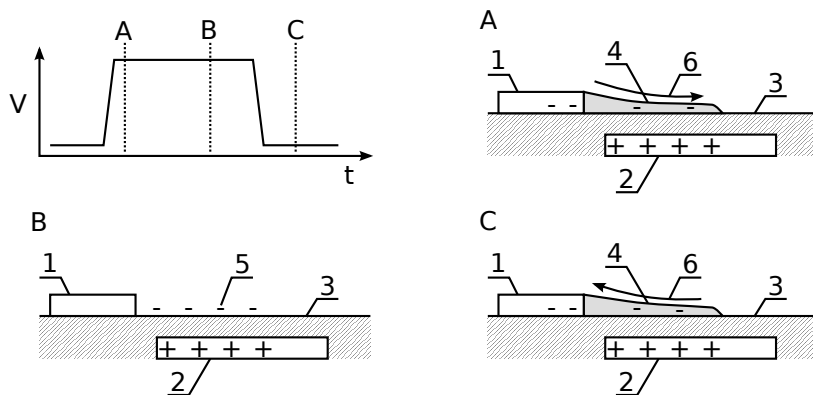


Figure 3.6: DBD discharge development in the actuator geometry: A — forward phase, the surface of the dielectric is charged by means of the discharge; B — “dark” phase (no discharge, the surface of the dielectric is charged); C — backward phase (after the pulse has ended, the charge from the surface of the dielectric flows back to the electrode). (1 — negative electrode (cathode), 2 — positive electrode (anode), 3 — dielectric barrier, 4 — plasma channel, 5 — charged surface of the dielectric, 6 — direction of charge movement)

tor. For example, irregularities on the edge of the electrodes can cause higher electric fields at particular points and thus can cause premature breakdown of the dielectric layer. The offset of the electrodes is preferably uniform along the whole actuator. Recently it was demonstrated that NS-DBD actuators can be manufactured using the same technologies as used for PCB (printed circuit board) manufacturing [12]. This allows for much better manufacturing precision, although it limits the choice of materials and some important parameters, such as dielectric thickness.

Care should be taken to prevent the breakdown of the actuator. Generally, sharp corners on the electrode edges should be avoided, because on corners the electric field is higher and can overload the dielectric. Corners at the open end of the actuator are particularly venerable, because the voltage there doubles, increasing the chances of electric breakdown of the dielectric layer. Recently, specific shapes for actuator electrodes have been developed to decrease this phenomenon.

Operating parameters

The performance of an NS-DBD plasma actuator depends greatly on the choice of its design and operation parameters, including the

- offset of the electrodes

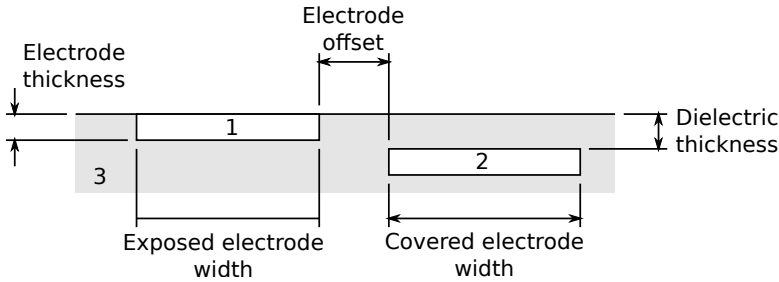


Figure 3.7: Dimensions of a NS-DBD plasma actuator (1 — exposed electrode, 2 — covered electrode, 3 — dielectric substrate). Flush-mounted variant shown. (Sketch in scale).

- thickness and material of the dielectric layer
- positioning of the actuator on the surface
- parameters of the electric pulses (voltage, frequency, pulse duration)

In this section we will discuss practical ranges and the general impact of the choice of the offset, dielectric thickness, and dielectric material on the performance of the actuator. The positioning of the actuator and its operating frequency should be chosen based on fluid dynamic considerations, as discussed in the following chapters. An experimental parametric study of electrical properties of the actuator can be found in [47], although for relatively long pulses of 250 ns.

The *offset* is the distance between edges of the electrodes measured along the surface to which the actuator is applied, Figure 3.7. Due to historical reasons, it is sometimes called “gap width”, despite the fact that it is not the same as the shortest distance between the electrodes. The offset affects the electric field strength between the electrodes — the smaller the offset, the higher the electric field. Generally, higher electric fields are preferable, and offsets are made with the smallest width possible — zero millimeters. Negative offsets are possible as well, meaning overlapping electrodes, but this increases electric capacitance of the actuator, thus decreasing the voltage.

The dielectric layer thickness and dielectric material are chosen in combination. The thickness of the dielectric affects strength of the electric field in the same way as the offset — a thicker dielectric means a lower electric field strength. A thin dielectric layer makes the electric field stronger and is preferable, because it makes the discharge easier to start and propagate. On the other hand, the breakdown voltage of the layer has to be enough to withstand the applied voltage for prolonged periods of time. The breakdown voltage of the layer can be calculated as a product of the breakdown electric field of the material and the thickness of

the dielectric layer.

$$V_{bd} = E_{bd}\delta = n_l E_{bd}\delta_1 \quad (3.9)$$

where V_{bd} is the breakdown voltage of the whole dielectric barrier, E_{bd} is the breakdown electric field strength of dielectric material used, δ is the total dielectric barrier thickness, n_l is the number of layers and δ_1 is the thickness of a single layer. The breakdown voltage should exceed the voltage of the pulse with some margin, allowing the layer not only to withstand the voltage of the pulse, but also the higher electric fields caused by irregularities and corners near the edges of the electrode, and voltage doubling due to pulse reflection on the open end of the actuator. The dielectric layer should also provide resistance to the temperatures caused by the discharge itself. Experiments have shown that a long series of pulses with a high frequency is more likely to cause breakdown, while a low pulse frequency can be applied for prolonged periods of time without consequences. This implies that the choice of material also depends on the intended pulse frequency.

As a material for the dielectric layer, self-adhesive Kapton tape of different thicknesses is normally used due to its high dielectric strength. A typical choice is Kapton tape with a dielectric strength of 106–165 kV/mm, and a layer thickness of 25 or 50 μm , giving minimum breakdown voltage of 2.5 and 5 kV per layer accordingly. However, other materials, including resistive materials based on silicon, have also been tried. These have demonstrated some interesting properties [12].

The width of the electric pulse is dictated by two types of considerations: plasmadynamic and technical. As the arc phase of the discharge is less efficient for the deposition of energy into the flow, it should be minimized. In DBD plasma actuators, the arc phase is prevented by presence of a dielectric barrier. During the streamer phase, the surface of the dielectric layer is charged up to the potential of the exposed electrode (Figure 3.6, A). After that, further application of the electric field can only affect the ions already present in the flow, accelerating them. This effect, called *ionic wind*, is utilized in the AC-DBD plasma actuators, where electric field is present for very long times. Since for NS-DBD actuators, the pulse is made just long enough for the streamer phase, the optimum pulse length is equal to the time needed to charge the surface of the dielectric completely to the pulse voltage. Experimentally, this time has been identified to be on the order of 10–30 ns. The pulse then ends and the charge from the dielectric surface flows back, making the second phase of the discharge the release of additional energy into the flow (Figure 3.6, C). If the pulse is made too short, however, the discharge does not have enough time to propagate along the surface and charge the entire actuator, and the energy of the pulse itself becomes very small, making the actuator ineffective for flow control purposes.

Technical considerations dictating pulse parameters include the availability of pulse generators with specific performance characteristics. Currently, there is a

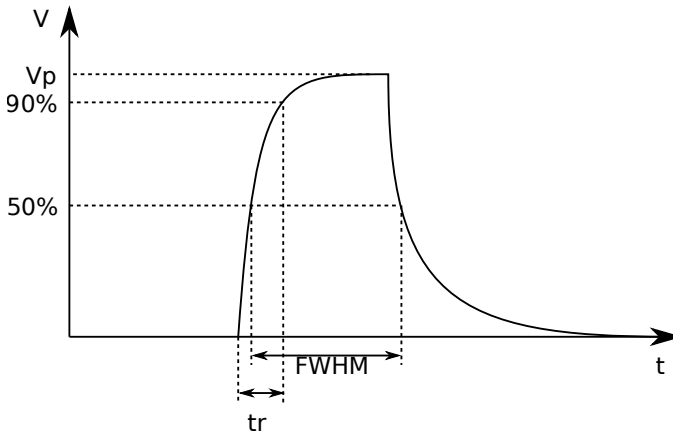


Figure 3.8: Typical nanosecond pulse shape used in NS-DBD plasma actuators. V_p — pulse voltage; t_r — rise time; t_{FWHM} — full width at half maximum.

wide range of pulse generators available for laboratory use. In most cases their choice involves a tradeoff between the maximum voltage and pulse frequency. The following table shows an example of available options for NS-DBD plasma actuators produced by the *FID Technology* company (for pulse parameters see [Figure 3.8](#)):

Model	Output voltage	Rise time	Pulse width	Repetition frequency
FPG 5-N	5 kV	1–2 ns	1–2 ns	300 kHz
FPG 10-N	10 kV	1–2 ns	1–2 ns	100 kHz
FPG 20-N	20 kV	1–2 ns	1–10 ns	10 kHz
FPG 50-N	50 kV	1–2 ns	1–10 ns	2 kHz

For commercial applications these generators are relatively expensive, bulky and provide some unneeded functionality, such as adjustability and protection. Pulse generators can be designed specifically for NS-DBD actuators, as demonstrated by NEQLab Research BV, where a cheap (on order of hundreds of euro) version was developed, which traded the pulse length (> 100 ns, longer than optimal) and rising time for low cost, small size and simplicity of construction, using an approach similar to [40].

As mentioned previously, the pulse frequency is limited by the durability of the dielectric layer, both in terms of resistance to high electric field and high temperatures arising from repetitive discharges at high frequencies. In many cases, however, a high pulse frequency is not needed. For example, flow instabilities have relatively low natural and receptivity frequencies, and can often normally

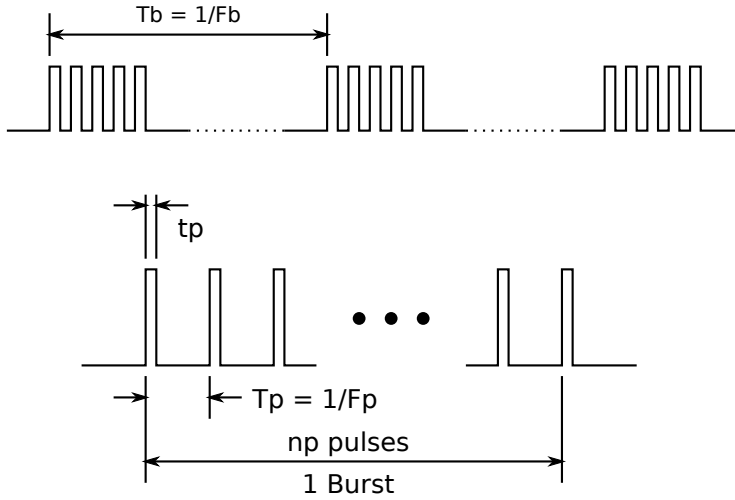


Figure 3.9: Burst mode of actuator operation: T_b — burst period; F_b — burst frequency; t_p — pulse length; T_p — pulse period; F_p — pulse frequency; n_p — number of pulses in a burst.

be amplified by depositing energy into the flow at these frequencies. In this case a *burst mode* can be used, as opposed to *continuous mode*. In a burst mode, as shown in Figure 3.9, pulses are repeated with a high rate within each burst, with a long time interval between bursts. If the *pulse frequency* in a burst is considerably higher than typical flow dynamic frequencies, each burst is equivalent to a single pulse with proportionally higher energy. Thus in a burst mode the *actuation frequency*, defined as a frequency at which the actuator affects (excites) the flow, is equal to the *burst frequency*. In a continuous mode, however, the actuation frequency is equal to pulse frequency.

Electrical measurements of NS-DBD actuators¹

Introduction

A pulse generator, a feeding cable, an actuator and a discharge comprise a complex electric circuit with non-trivial behavior, as has been observed in [48, 49]. For practical purposes, knowledge of the electrical properties of the actuator is needed in order to make correct design decisions. First, knowledge of how much energy is put into the actuator with given pulse parameters is needed. This is a key quantity for the numerical modeling of the actuator using a thermal model. Sec-

¹Experiments described in this section were done at NEQLab Research BV by Ilya Popov and Giuseppe Correale.

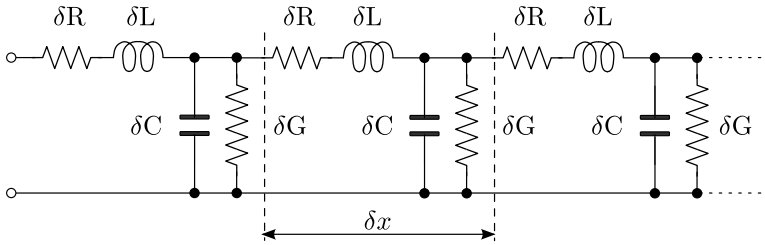


Figure 3.10: Transmission line equivalent circuit representation using lumped elements.

only, knowledge of the maximum length of the actuator for a given set of design parameters is required. We now describe experiments with which the behavior of the pulse propagating along the actuator is examined in order to determine these quantities.

For nanosecond pulses, the actuator behaves as a *transmission line*. A transmission line is a circuit with capacitance and inductance distributed along its length. The most common example of transmission line is a coaxial cable. Dividing the transmission line into small pieces, and substituting localized (*lumped*) capacitance and inductance values for distributed ones, we arrive at the equivalent circuit shown in [Figure 3.10](#).

The propagation of electric signals in the transmission line is governed by the *telegrapher's equations*:

$$\begin{aligned}\frac{\partial V}{\partial x} &= -L \frac{\partial I}{\partial t} \\ \frac{\partial I}{\partial x} &= -C \frac{\partial V}{\partial t}\end{aligned}\tag{3.10}$$

or, combining these:

$$\frac{\partial^2 V}{\partial t^2} - v^2 \frac{\partial^2 V}{\partial x^2} = 0\tag{3.11}$$

where $V(x, t)$ is the voltage, $I(x, t)$ is the current, L is the inductance per unit length, C is the capacitance per unit length and v is the wave speed

$$v = \frac{1}{\sqrt{LC}}\tag{3.12}$$

The resulting equation (3.11) is a wave equation, which has a solution composed of the superposition of two waves traveling with velocities $+v$ and $-v$. The direction of propagation is determined by the sign of the product $I \cdot V$, which is equal to local energy transfer rate.

Along with propagation speed, another parameter describing a transmission line, such as an actuator or a coaxial cable, is its *impedance*. Impedance is equivalent to resistance for signals of specific frequency. In general, its value is a complex number, which shows not only proportionality between voltage and current, but also phase shift between them. For transmission lines, impedance has real value, independent of frequency:

$$Z = \sqrt{\frac{L}{C}} \quad (3.13)$$

For example, typical coaxial cables have impedance in the range 50...100 Ω . When transmission lines with different impedances are connected to each other, the pulses are partially reflected at the connection point. This implies that for the best efficiency, the impedance of the actuator should match that of the feeding coaxial cable.

A pulse traveling in one direction (for example, in direction of the increasing x coordinate), will initially travel without changing its shape and magnitude. On reaching the end of the line, the pulse may be reflected back, depending on the impedance of the end of the actuator. If the impedance is infinite (open circuit), the pulse is reflected with the same polarity of voltage and a changed polarity of current. If the impedance of the end of line is equal to the impedance of the line itself, there is no reflection. If the impedance is zero (a short circuit), the polarity of voltage is changed, but the current remains unchanged. For all the cases mentioned, the shape and magnitude of the pulse remain unchanged. For any other impedance, the result is a blend between these three cases.

When a high-voltage pulse propagates along the actuator, a discharge develops, which dissipates some pulse energy into the air. The magnitude of the pulse thus decays along the actuator. After some length, the voltage of the pulse may drop lower than needed for discharge to start, which limits the effective length of the actuator.

Experimental setup

One of the goals of the measurements presented here is to identify the relation between the pulse voltage and achieved length of the discharge. Additionally, the effect of voltage doubling on the end of open transmission line is examined.

The 1.6 m long actuator used in these experiments had electrodes 10 mm wide and 0.15 mm thick and a dielectric layer about 0.3 mm thick. The offset between electrodes was about 0.1–0.2 mm. A high-voltage pulse generator was connected with a feeding coaxial cable to the actuator section through an inductive current probe (Figure 3.11). A second 1.6 m long actuator could optionally be connected to the end of the first one, making it a 3.2 long actuator. The voltage was measured

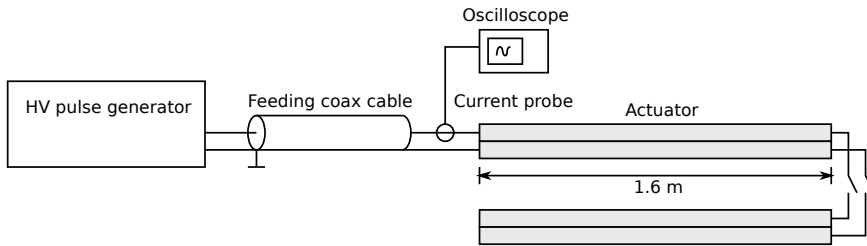


Figure 3.11: Schematic of the experimental setup.

using a high-voltage probe at three different positions: at the beginning of the actuator, at the point between two sections and at the end of the actuator.

Low voltage measurements

First, a series of measurements using low voltage pulses was conducted to determine the impedance of the actuator, pulse propagation velocity and impedance matching quality. A low voltage was chosen to avoid additional effects associated with the discharge, making the signals clearer and the interpretation of the results easier. A Tektronix AFG 3252 function generator was used as a pulse source. The pulse magnitude was 5 V, and the width was 10 ns with 2.5 ns edges. The pulse was fed to the actuator with a 50 Ohm coaxial cable approximately 1 m long. The voltage was recorded using a Tektronix TDS 3054C oscilloscope and a low voltage probe. The measurements were synchronized using a trigger output of the function generator.

Second, the voltage on the end of open 50 Ohm cable was recorded as reference. Then the cable was connected to the actuator, and the voltage on the beginning of the actuator was recorded. Finally, the voltage on the end of the actuator was recorded. These voltages are shown in [Figure 3.12](#).

According to theory, the voltages on the end of the open coaxial cable and on the open end of the actuator are expected to be double the voltage of the incident pulse. Thus, in order to make comparison more clear, the voltage at the beginning of the actuator is plotted doubled, so that all the curves should have the same magnitude and shape. Additionally, and all four pulses (in the coaxial cable, at the beginning of the actuator, superposition of incident and reflected pulses at the end of the actuator, and reflected pulse at the beginning of the actuator) were aligned with each other in time. The resulting plot is shown in [Figure 3.13](#). It can be seen that the pulses coincide well, which means no dissipation is present in these conditions. Also, all of the pulse from the coaxial cable is passed into the actuator, since the pulse at the end of the actuator and at the end of the open

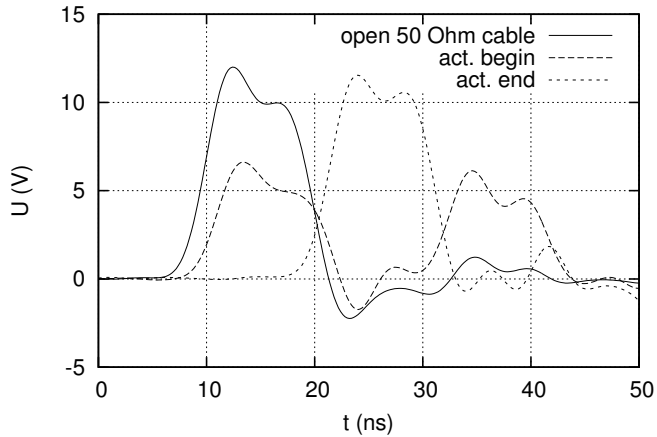


Figure 3.12: Voltages in the open cable, at the beginning of the actuator and at the end of the actuator plotted over time.

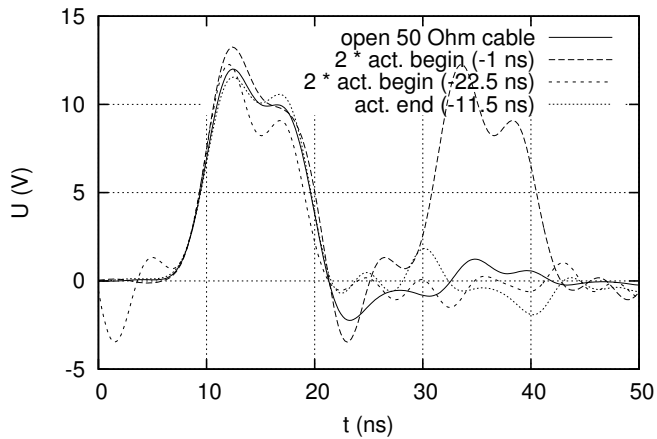


Figure 3.13: Beginning and end pulses (same as in [Figure 3.12](#)) plotted aligned with each other (pulses at the beginning of the actuator plotted with double their values).

cable coincide. Thus we can conclude that the impedance of the actuator matches the impedance of the cable

$$Z \approx 50 \Omega \quad (3.14)$$

The pulse propagation times in both the forward and backward directions along the actuator were equal to 10.5 ns which translates to a propagation speed of

$$v = \frac{L}{\Delta t} = \frac{1.6 \text{ m}}{10.5 \text{ ns}} = 1.52 \cdot 10^8 \text{ m/s} = 0.51c \quad (3.15)$$

where $c = 3 \cdot 10^8 \text{ m/s}$ is the speed of light in vacuum. The measured pulse propagation speed implies a pulse delay of 6.6 ns/m.

The low-voltage measurements confirm that the NS-DBD actuator exhibits properties of a transmission line with an impedance of 50 Ohm and a wave propagation speed of $v = 0.51c$. The pulse was found to be reflected from the end of the actuator with the same voltage polarity as is expected from an open end. During propagation, the shape of the pulse was found to be undistorted and the magnitude unchanged.

High voltage measurements

A series of measurements of high-voltage behavior was also carried out. Here, high voltage implies voltages on the order of several kilovolts. The voltages in this series of experiments were measured using an oscilloscope with a special high-voltage probe and a current probe connected between the feeding coaxial cable and the actuator. The measurements thus include all the effects of the discharge. Of interest is: how fast the high voltage pulse decays, what is the minimum voltage needed for the discharge to develop, how long the actuator can be powered with certain pulses, and how these properties depend on pulse voltage and repetition frequency.

Short (1.6 m) actuator

The experiments on the 1.6 m long actuator were carried out using a FID solid state nanosecond high-voltage generator. The voltage used was the maximum the pulse generator could produce (about 12 kV). The actuation frequencies used were 100 Hz, 1 kHz, 3.3 kHz, 5 kHz, 10 kHz.

The current at the beginning of the actuator and the voltages at the beginning and at the end of the actuator were measured. The current was measured using a current probe, and the voltage using a LeCroy high-voltage probe. The measurements were synchronized using a signal from the divider output of the high-voltage generator. The current and voltage measurements had different delay times and were aligned before comparison. A typical plot of the data measured

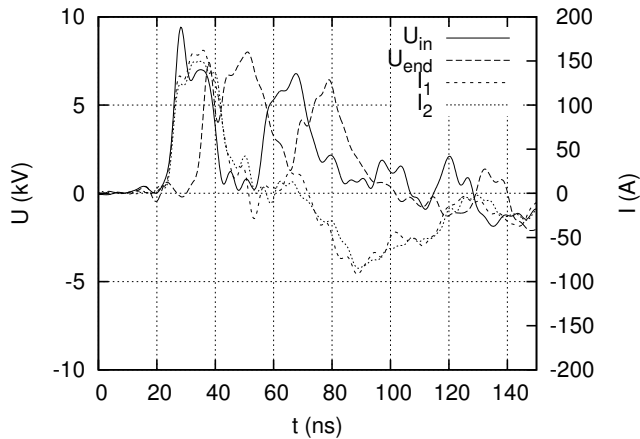


Figure 3.14: Example of high voltage measurements for one frequency (5 kHz), 1.6 m actuator.

is shown in the [Figure 3.14](#). The voltage measurements were made in separate experiments, so two current traces are present on the plot. These two traces coincide, indicating there is a good repeatability of the data between different experiments.

[Figure 3.15](#) compares the voltages at the beginning of the actuator at different repetition frequencies. [Figure 3.16](#) and [Figure 3.17](#) show analogous data for the voltage at the end of the actuator and the current at the beginning. It can be seen that the voltage at the end is roughly equal in magnitude to the voltage pulse at the beginning (9 kV peak at beginning v. 8 kV peak at the end). However, it should have been doubled due to the infinite load at the end. This means that the pulse lost roughly half of its voltage during propagation along the actuator.

It can also be seen ([Figure 3.14](#)) that the pulse shape is not affected by the actuation frequency until $t \approx 100$ ns. Since this time is much longer than the round-trip time of the pulse, this difference cannot be solely the result of the difference in propagation properties. The exact reason of this difference is not known, and is hypothesized to arise from differences in the properties of the output circuits of the high-voltage pulse generator. We can conclude that the electrical properties of the actuator do not depend on the repetition frequency. This in turn suggests that the influence of one pulse on the next is small.

The forward propagation time is the same as for the low voltage case, meaning that the propagation speed is the same and the electrical properties (such as capacitance and inductance) are the same. However, the backward propagation time of the reflected pulse is much longer. This can be attributed to an increase

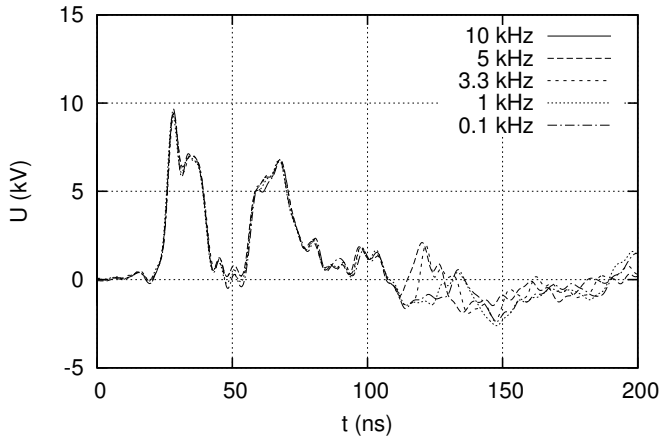


Figure 3.15: Voltage at the beginning of the 1.6 m actuator for different actuation frequencies.

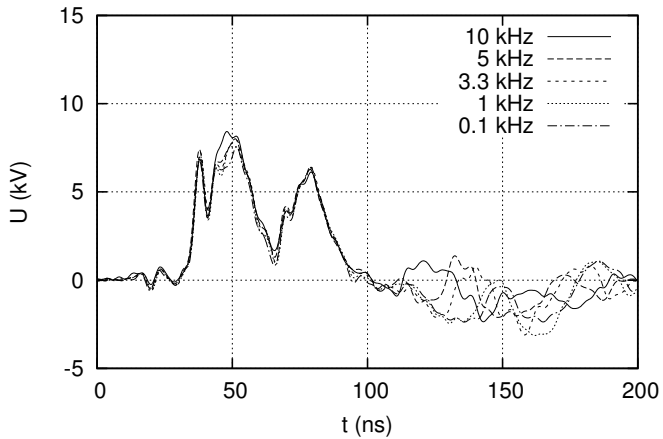


Figure 3.16: Voltage at the end of the 1.6 m actuator for different actuation frequencies.

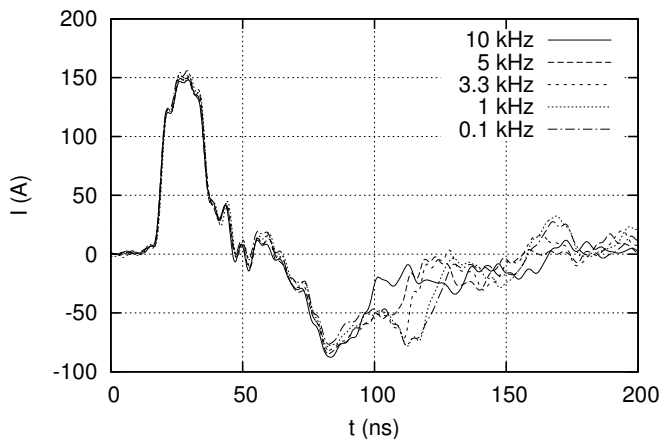


Figure 3.17: Current at the beginning of the 1.6 m actuator for different actuation frequencies.

of the capacitance of the actuator due to the additional conductive surface area formed by the plasma layer above the covered electrode. By the time the reflecting pulse arrives at the beginning of the actuator, there are already multiple reflections along with electromagnetic interference (EMI), which can obscure the results. What is also interesting is that the pulse at the end of the actuator is much wider than that at the beginning (22 ns v. 15 ns).

Long ($L = 3.2$ m) actuator

The same measurements were carried out for a 3.2 m actuator. In this case the voltage was measured at three locations: at the beginning, at the middle (1.6 m) and at the end of the actuator. The results of the measurements are presented in [Figure 3.18](#)–[Figure 3.22](#).

On these plots we see two distinct pulses. Comparing the timings of these two pulses at three different positions, we conclude that both pulses propagate in the forward direction. Thus we can conclude that the second pulse is a reflection of the pulse from the beginning of the actuator, rather than from the output circuits of the generator. The delay between two pulses agrees with an approximation based on cable length (2.7 m) and propagation speed (about 5 ns/m) which gives 27 ns (the measured delay is about 32 ns). The propagation speed of the pulse in the actuator agrees with that of the low voltage measurements.

The mean magnitude of the pulse at the beginning is ≈ 8 kV with peaks up to 10 kV, in the middle — 5 kV / 6 kV (mean/peak), and at the end — 5 kV / 7 kV with some pulse widening. Thus we can estimate voltage losses as about 40% for each

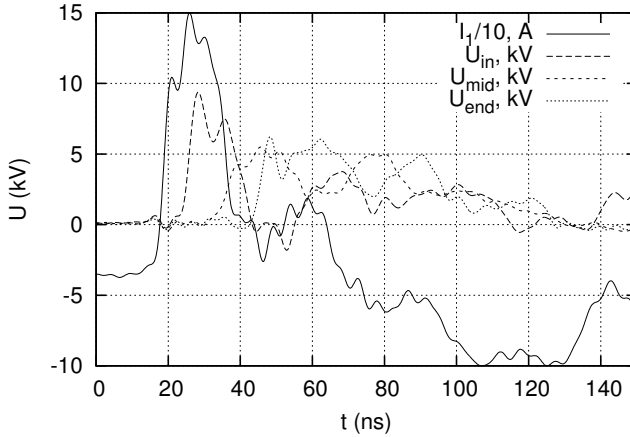


Figure 3.18: Example of measurements for one actuation frequency (5 kHz), 3.2 m actuator.

leg of 1.6 m (taking into account that the voltage at the end should be doubled).

The analysis of later parts of the time history is complicated because of the superposition of several pulses traveling in different directions.

Sensitivity to voltage change

The same measurements were conducted for a 3.2 m long actuator at single low actuation frequency (100 Hz) at lower voltages. The goal of these measurements was to determine minimum voltage needed to achieve the discharge along the whole actuator.

Two voltages were tried. In the first case, the voltage of the pulse (3.5 kV measured) was too low to initiate the discharge directly. Thus discharge was seen only on the last 78 cm of the actuator, which coincides with the expected area of voltage doubling calculated given the propagation speed (measured in low voltage tests) and pulse width. Plots of the voltage and current are shown in [Figure 3.23](#). Here, the pulse in the middle of the actuator is about 90% of the pulse at the beginning, which means that only a minor loss in amplitude was observed. This agrees with the lack of the visible discharge at that position. The pulse at the end had voltage about 1.3 times more than in the middle, meaning that there was about a 30% loss of voltage along the second half of the actuator, a significant increase of the voltage loss compared to the first half of the actuator. The total voltage loss was about 40% in this case.

The voltage was then increased until the discharge appeared along the whole actuator, occurring at about 6 kV. The corresponding plots are presented in [Fig-](#)

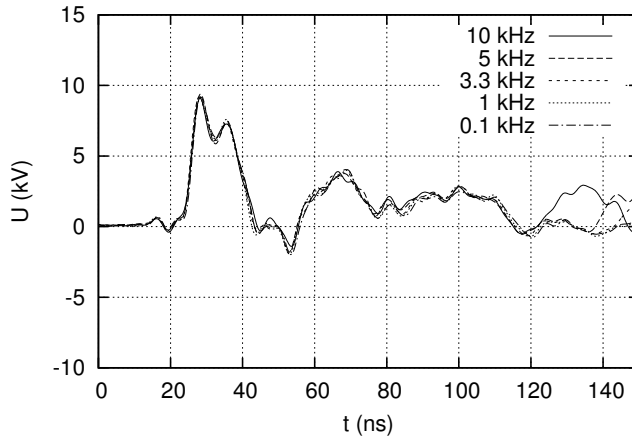


Figure 3.19: Voltage at the beginning of 3.2 m actuator at different actuation frequencies.

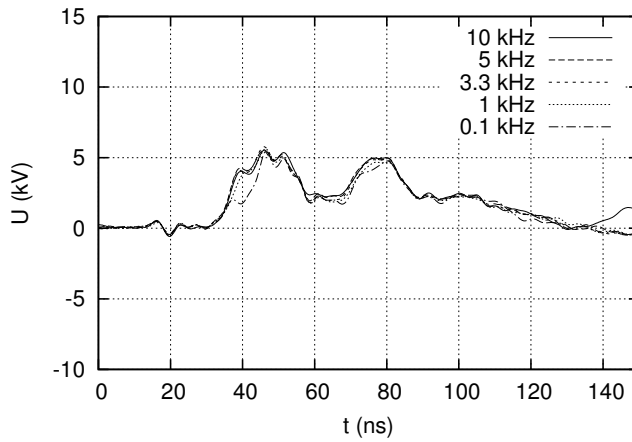


Figure 3.20: Voltage at the middle of 3.2 m actuator at different actuation frequencies.

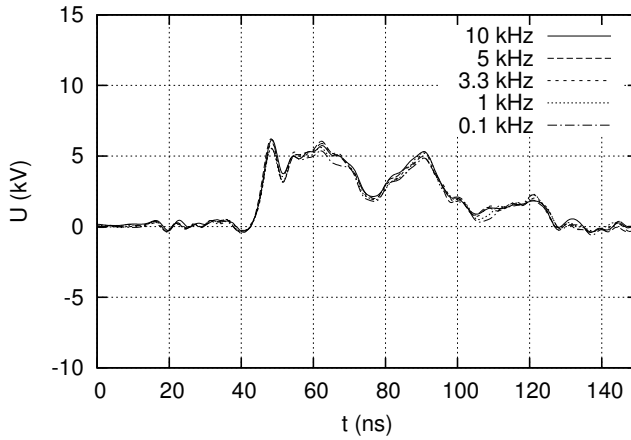


Figure 3.21: Voltage at the end of 3.2 m actuator at different actuation frequencies.

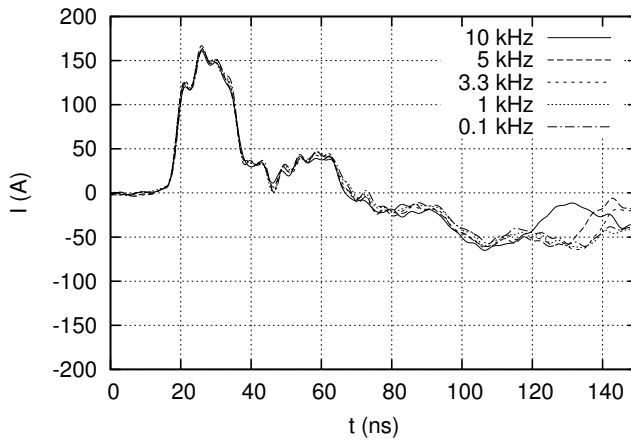


Figure 3.22: Current at the beginning of 3.2 m actuator at different actuation frequencies.

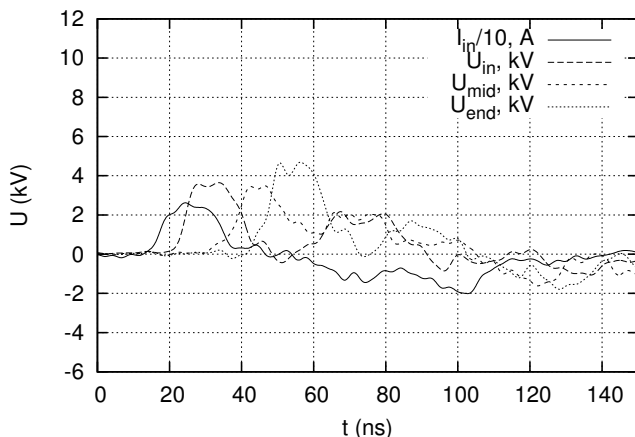


Figure 3.23: Voltage at three locations and current for a 3.5 kV pulse with the 3.2 m long actuator.

[ure 3.24](#). In this case the voltage in the middle is about 70% of the voltage at the beginning, and the voltage at the end was about the same as at the beginning, giving total voltage loss of 50%. It is interesting that the voltage at the end was the same as in previous experiment, despite the significant difference in the input voltage. This is a consequence of voltage threshold associated with the discharge. Once the local voltage drops below this threshold, its rate of decay becomes very low.

Spark gap generator

The feasibility of using a simpler, cheaper and compact spark gap generator developed at NEQLab Research has also been studied. This type of generator uses a spark gap as a switching device instead of semiconductor diodes used in more sophisticated generators. The generator produced a pulse with good rising edge, but very slow decay. This type of generator does not allow the user to control voltage, pulse shape or repetition frequency without modifying the internal components of the generator. Therefore, the measurements were done with only one set of parameters. The voltage was measured at the same three positions on the actuator. The results of the measurements presented in [figures Figure 3.25](#) and [Figure 3.26](#).

This generator was found to be capable of charging a 3.2 m long actuator to 6 kV (with a peak up to 8 kV). Discharge was observed along the whole actuator.

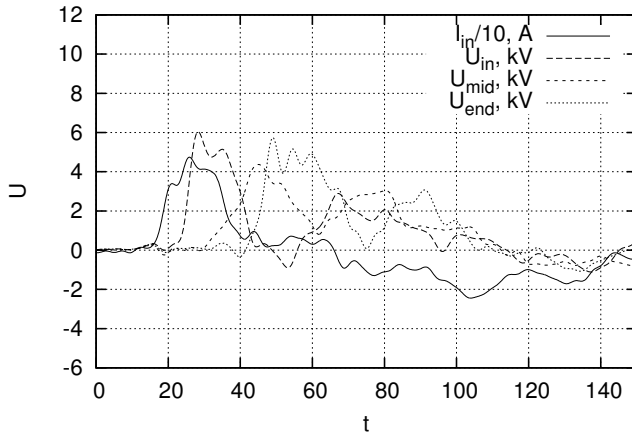


Figure 3.24: Voltage at three locations and current for a 6 kV pulse with the 3.2 m long actuator.

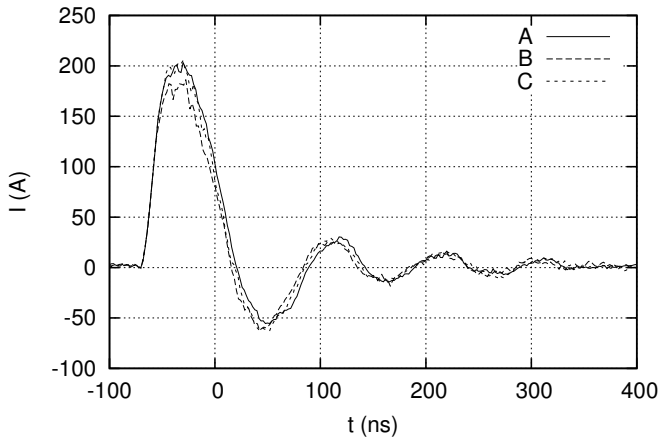


Figure 3.25: Current plot taken in three experiments using the spark gap generator.

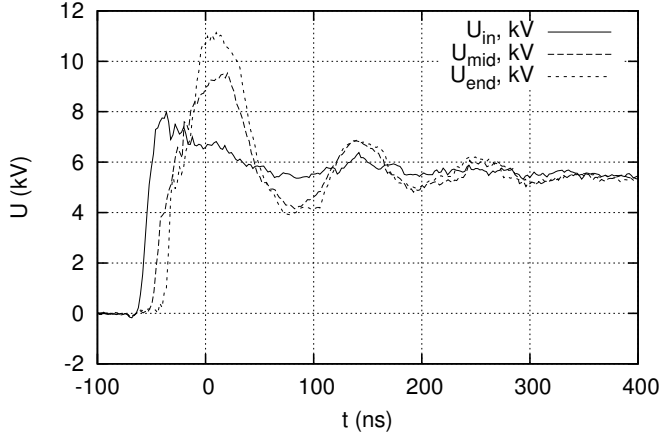


Figure 3.26: Voltage at three locations using the spark gap generator.

Energy per pulse

The voltage and current data obtained with the experiments allows computation of the energy of the pulse, reflected energy, and energy deposited into the discharge. Voltage and current probes have their own internal time delays, and there was a difference in lengths of the cables connecting the probes to an oscilloscope. Because of this, the voltage and current signal were shifted 6.5 ns in time relative to each other. Thus, before the computations, the voltage and the current were aligned using the first rising edge of the pulse as a reference. Additionally, there was a bias in the current signal. To eliminate it, the current signal was averaged for a period prior to the pulse and the result subtracted from the signal.

Given the final voltage and current histories, the instantaneous power can be computed as:

$$P(t) = V(t) \cdot I(t) \quad (3.16)$$

and total energy can be computed as an integral of the power:

$$E = \int V I dt = \sum_i V_i I_i \cdot (t_i - t_{i-1}) \quad (3.17)$$

The total charge transferred into the actuator is then computed by integrating the current:

$$Q = \int I dt = \sum_i I_i \cdot (t_i - t_{i-1}) \quad (3.18)$$

where $V(t)$ is voltage measured at the beginning of the actuator and $I(t)$ is the aligned current value. Integration was done for 200 ns starting at the beginning of

the pulse. This long period was selected in order to ensure that all the reflected pulses are taken into account. Thus, the result of (3.17) shows the amount of energy left in the actuator. For short pulses, this is equal to the discharge energy, but in the case of long pulses (as produced by the spark gap generator), there is an amount of energy stored in capacitance of the actuator. The results are shown in the following table.

Case	Energy input
1.6 m max voltage	15.2 mJ
3.2 m max voltage	15 mJ
3.2 m 6 kV	6.2 mJ
3.2 m 4 kV	2.2 mJ
3.2 m spark gap generator	64 mJ

The energy of the discharge is only marginally dependent on the length of the actuator, meaning that increasing actuator length without changing pulse parameters will make the discharge energy density proportionally lower.

In order to estimate the discharge energy of the spark gap generator, the total capacitance and energy stored in the actuator were estimated. Since pulse length was much longer than the propagation time, the actuator was eventually uniformly charged. For this case, integration time was 400 ns. At the end of this period, the voltage was stabilized at $V = 5.5$ kV, while the total charge passed into the actuator was $Q = 9.2 \cdot 10^{-6}$ C, and the transferred energy was $E_t = 64$ mJ. Given this data, we can estimate capacitance (assuming no breakdown and thus no charge loss) as:

$$C = \frac{Q}{V} = 1.66 \text{ nF} \quad (3.19)$$

and stored energy as

$$E_s = \frac{QV}{2} = 25.4 \text{ mJ} \quad (3.20)$$

which yields a discharge energy of

$$E_d = E_t - E_s = 40 \text{ mJ} \quad (3.21)$$

The reliability of these results is, however, limited by the fact that on these time scales the voltage was slowly dropping, although without any back current detected by the current probe. This might be result of the limited sensitivity of the current probe to low-frequency signals (≤ 400 Hz) or of some unidentified current leak in the actuator.

Conclusions from the experiments

The actuator was shown to behave as a transmission line with a propagation speed $v = 0.51c$ and impedance $Z = 50 \text{ Ohm}$ for both low (5 V) and high (3–10 kV) voltage. This particular actuator matched the feeding cable well, so no significant losses were observed in the connection. Voltage doubling was observed on the open end of the actuator, as predicted by theory. For low-voltage pulses no pulse decay along the actuator was observed.

For high-voltage pulses there was no dependency of the electric parameters on the actuation frequency, suggesting that discharges from consecutive pulses interact only marginally. The minimum voltage needed to ignite discharge along the whole actuator was found to be about 6 kV. At lower voltages (4 kV), discharge was observed only on last 78 cm of the actuator, where voltage doubling takes place. The ratio of the voltages at the end and the beginning of the actuator was found to be dependent on the initial voltage because the discharge intensity and thus the decay rate of the pulse rise quickly as the voltage exceeds the discharge threshold. Pulses having voltage higher than the discharge threshold decayed while propagating along the actuator, as shown in the table.

Length, m	V_{in} , kV	Discharge	$V_{1.6}/V_{\text{in}}$	$V_{3.2}/V_{\text{in}}$
1.6	9	full	0.5	—
3.2	9	full	0.6	0.3
3.2	6	full	0.7	0.4
3.2	4	partial	0.9	0.6

The value of energy input into the discharge was calculated, and amounted to 15 mJ at full voltage independent of the actuator length. This energy value will be used for a thermal model of the actuator presented in [chapter 4](#).

A cheap compact spark gap pulse generator was also tested. This generator produced pulses with peak voltage of about 7 kV, with fast rising times and a long decay ($> 1 \mu\text{s}$). Due to the long duration of the resulting signal, the input amounted to 40 mJ per pulse.

Chapter 4

NS-DBD actuator modeling

This chapter describes the development of a simplified model of the NS-DBD actuator suitable for use in numerical simulations. After a brief overview of the model requirements, the most significant physical effects produced by NS-DBD actuators are considered in turn. For each of these, experimental observations are reviewed, their relevance to the modeling of actuator effects described. Finally the model is proposed, and some aspects related to its numerical implementation are discussed.

Introduction

In [chapter 3](#) the physical processes which occur in NS-DBD plasma actuation were described. In principle, all of these processes can be modeled in detail as is done in [\[50–52\]](#). Although such simulations are useful for examining the underlying mechanisms of actuation, they involve very small length and time scales [\[28, 65, 71\]](#). As the fluid phenomena to be controlled have relatively long length and time scales, coupling detailed models of NS-DBD to flow simulations is prohibitively expensive, particularly in the design context. Thus, the development of a simplified model of NS-DBD actuators for fluid-dynamical simulations is necessary. Such a model should:

- be able to reproduce the relevant physical phenomena observed in experiments;
- be computationally cheap and easily inserted into any simulation framework;

- contain parameters which allow accurate calibration over a range of conditions.

In the following sections the physical phenomena observed in experiments are considered, and the implications for the model developed here discussed. Then the design options are addressed. Next, we describe numerical implementation of the actuator model and discuss its integration into finite volume numerical simulations using OpenFOAM. Then we discuss additional requirements the model places on the parameters of the simulation, such as spatial and temporal resolution. Finally, we present selected observations of the behavior of the model.

NS-DBD effects and model assumptions

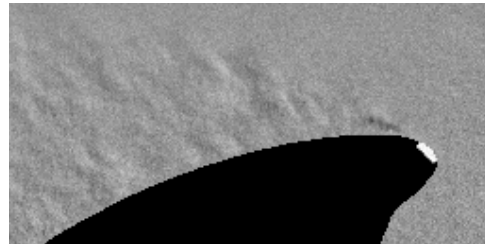
As already discussed in [chapter 2](#) and [chapter 3](#), there are numerous experiments demonstrating various effects of NS-DBD actuators. In this section we review these effects and discuss their implications for the model design.

Compressible and thermodynamic effects

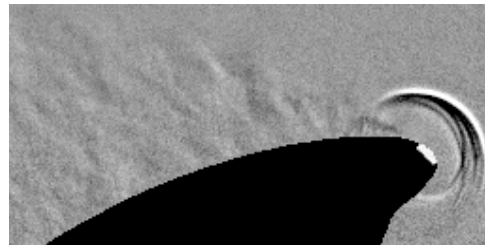
One of the more distinctive properties of the NS-DBD plasma actuators the strong compressible flow effects they produce. NS-DBD plasma actuators result in significant local heating of the flow and have been observed to generate compression waves. The observation of compression waves is particularly clear when using Schlieren imaging. In this technique, a parallel beam of light passes through the flow. The beam is then focused into a knife edge, thus cutting off the light deflected in one direction. The index of refraction index of gas depends on the density gradient, so the the beam is defected in the positive density gradient direction. The areas with gradients of density are then seen in the resulting image as lighter or darker areas. This technique allows to clear visualization of shock waves, strong vortices, areas with temperature variation and areas with high turbulence levels.

Examples of schlieren imaging of NS-DBD plasma actuators can be found in [[11](#), [13](#), [58](#), [67](#), [70](#)]. A typical set of images is shown in [Figure 4.1](#). The black shape is the airfoil model, which was installed in a wind tunnel at a high angle of attack. In A, the airflow (coming from the right) experiences leading edge separation. The separated region can be seen as an area with higher fluctuations in brightness (indicating high turbulence level).

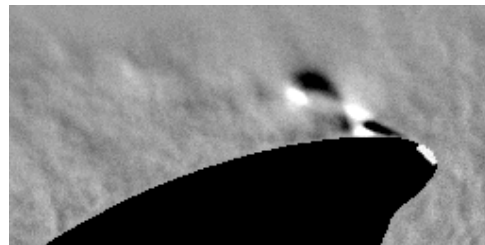
In B, we see the initial effects of the actuator, which has been placed on the surface of the airfoil close to its leading edge. The most prominent effect is a compression wave occurring after the discharge. This wave is a distinctive feature of NS-DBD plasma actuation when compared to the other types of the plasma



A



B



C

Figure 4.1: Example of schlieren imaging results. From top to bottom: 1 — unactuated flow; 2 — compression wave; 3 — coherent vortex structure. Flow direction from right to left. Black shape is the airfoil, and white mark at the leading edge indicates the position of the actuator [13].

actuators, such as the AC-DBD actuator. This is the reason why compression waves attracted significant attention from researchers, and was hypothesized as being a main actor in actuator's effects. Parameters of the wave have been measured by several researchers. Immediately after the discharge, the speed of this wave is slightly higher than a speed of sound (wave speed $\approx 400\text{m/s}$), but after several millimeters of travel, it becomes equal to the speed of sound. This means that at first it is only a weak shock wave, and later becomes an ordinary acoustic wave.

The presence of the compression wave emphasizes the thermal nature of the NS-DBD phenomena, which motivates the use of compressible flow simulations when examining their effects. To resolve the wave accurately in such a simulation, sufficient spatial and temporal resolution is required. However, as will be shown in [chapter 6](#), that the main flow effects observed in such simulations are insensitive to the wave being well resolved or not. This leads to the conclusion that the wave itself does not play a major role in determining the effect of the actuator. Nonetheless, the compression wave pattern is a valuable source of information about the spatial structure of the energy deposition during the process of actuation.

The presence of an expanding compression wave indicates that there is thermal energy deposition involved [[1](#), [13](#), [70](#)]. Indeed, the observed wave pattern is similar to that which would be obtained if some amount of thermal energy was instantly (compared to fluid-dynamic time scales) deposited into the flow. This is supported by the theoretical plasmaphysical considerations [[5](#), [29](#), [43](#), [59](#)]. Theoretical analysis and modeling on NS-DBD type of discharge indicates that the energy of electric field, first stored in plasma in the form of ionization and excitation, is mostly released into the thermal form on the time scale of 1 microsecond after discharge.

Taking into account theoretical considerations, we get the following sequence of events and associated temporal scales:

- 20ns (time scale of the voltage pulse and discharge) — The energy of the voltage pulse is stored in the plasma via the ionization and excitation of molecules.
- $\sim 1\mu\text{s}$ — The energy stored in the plasma is converted into thermal energy. A small area of high-temperature gas is formed.
- $\sim 1\text{ms}$ — The high temperature area of gas expands, forming the compression wave observed in the experiments. The wave carries away part of the energy. After the wave is gone, pressure is equalized and there is an expanded area of gas left with temperature higher than the background temperature.

- $\sim 10\text{ms}$ (a typical fluid-dynamical time scale, corresponding frequencies on the order of 100 Hz) — Large scale vortical structures form in the flow and evolve according to the flow stability properties.

Conclusions NS-DBD plasma actuators are characterized by presence of thermal effects, as implied by observations of the compression wave and the area of heated gas. The time scale of thermal energy deposition is on the order of $\sim 1\ \mu\text{s}$. There is large separation of scales between the discharge, thermal effects and fluid-dynamical effects.

Momentum deposition

In experiments involving another type of plasma actuators, AC-DBD plasma actuators, momentum deposition into the flow has been observed. This momentum deposition is caused by so-called ionic wind. Researchers first expected to see similar effects with NS-DBD plasma actuators. However, the momentum deposition, although present, was found to be very weak. In still air or low speed flows, the maximum observed velocity change was found to be on the order of 2 m/s [30], much lower than in the case of AC-DBD plasma actuators. This value too low to cause any significant fluid-dynamical effects in the much higher speed flows typical of flow control applications.

The difference in the momentum deposition between NS and AC plasma actuators is due to difference in time intervals during which the electric field interacts with the ions in plasma. In the case of AC-DBD plasma actuators, the electric field is present for a long time after the plasma is generated, pulling the ions and electrons in opposite directions and transferring momentum into the flow [31]. For AC-DBD actuators, the momentum transfer can be successfully modeled using a volumetric source term in the momentum equation [20]. In the case of NS-DBD plasma actuators, the pulse is just long enough to generate the ions, but ends immediately afterwards. Thus the action of the electric field on the ions is too short to have a significant effect on flow momentum.

Conclusions Momentum transfer in the case of NS-DBD plasma actuators is relatively low (compared to the AC-DBD actuators), and is not considered to play major role in their control effect. Thus, there is no requirement for the model to reproduce momentum transfer in most cases of interest. Should the modeling of the momentum transfer be required, however, it can be done with the source term in the momentum equation, as has been demonstrated for AC-DBD plasma actuators.

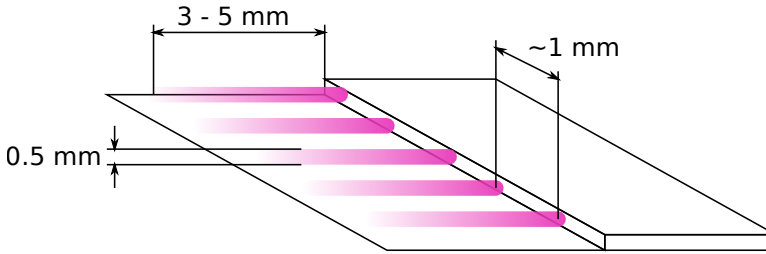


Figure 4.2: Simplified discharge structure showing filaments.



Figure 4.3: Photographic image of the discharge structure (top view; inverted grayscale). Image source: Giuseppe Correale.

Spanwise uniformity of the actuator effects

Detailed observations reveal that discharge itself is not spanwise-uniform, but consists of the number of *filaments* — small elongated channels starting from one of the electrodes. Inside these filaments, the intensity of the discharge is higher. The filaments are traces of the streamers, which start concurrently from edges of the electrode. For typical actuation parameters (voltage about 10 kV, pulse length about 20 ns) filaments are spaced at about 1 mm from each other. Their approximate thickness is several tenths of a millimeter, and their lengths on the order of ~ 5 millimeters. These values vary with the voltage, air pressure and the quality of the electrode edge. In general, lower pressures or a faster rising time make the discharge more uniform. A schematic of the discharge structure is shown in [Figure 4.2](#).

Each of these filaments acts as a center of heat release after the discharge, making heat release non-uniform. This non-uniformity can be observed in schlieren images as multiple overlapping circular waves starting at each filament [38]. The individual waves combine after a very short distance (on the order of millimeters) to form a single cylindrical wave, as sketched in the [Figure 4.4](#).

Despite the fact that the discharge itself is not locally uniform, the large-scale

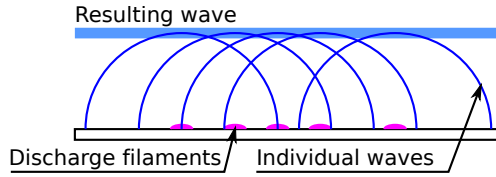


Figure 4.4: Observed overlapping waves sum up to form an overall cylindric wave.

flow-dynamic effects of the actuation appear to be spanwise uniform. In Figure 4.1 B and C, compression waves and an initial shear layer are clearly defined. In C, (taken several milliseconds after the pulse), *vortex structures* also appear in the separation region. Schlieren imaging produces an optical average of information in the span-wise direction, since the beam of light passes along the whole span of the model, integrating the density gradients along its path. As the vortex structures are clearly visible, they must be quasi-coherent in the spanwise direction, otherwise they would be filtered out by the optical integration. Furthermore, the vortex structure is highly reproducible from pulse to pulse. Another important observation is that the spatial scale of the vortex structure is much larger than the natural scales of turbulence in the flow (in the separated region). The vortex structure propagates along the boundary of the separation region and grows, exhibiting convective instability behavior. Summarizing all these observations, discharge leads to the generation of large scale spanwise-uniform vortex structure in the separation region, which propagates downstream, mostly along the boundary of separation region.

Conclusions Many relevant flow situations, such as boundary-layer transition and leading edge separation are initially two-dimensional. From experimental observations, it seems that NS-DBD actuators also produce disturbances which are initially spanwise uniform. In these regions, where there is a clear separation between the scales of the dominant flow phenomena and those of localized turbulence, it should be possible to consider two-dimensional flow simulations, allowing for the efficient initial evaluation of actuator models.

Cross-sectional distribution of energy

The cross-sectional distribution of the discharge and its energy release is difficult to observe directly. However, there are two ways to measure it indirectly.

The first method is based on the light emission of the nitrogen molecules. By comparing the emission levels of certain spectral lines of Nitrogen molecules, it is possible to calculate the local temperature of the gas.

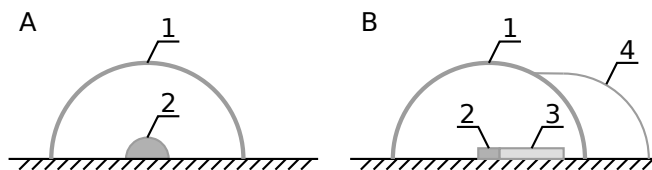


Figure 4.5: Examples of wave patterns in the case of symmetric (A) and asymmetric (B) sources. 1 — main compression wave, 2 — main energy deposition region, 3 — additional asymmetric energy deposition region, 4 — additional weaker wave.

The second method is based on the analysis of the compression wave patterns. For linear or axisymmetric source (such as a cylinder), the shape of the produced wave is cylindrical and leaves a (semi)circular trace on a schlieren image (Figure 4.5, A).

In some of the experiments, however, more complex patterns have been observed, as shown in Figure 4.5, B. In this case, the wave pattern consists of two distinct parts: a stronger cylindrical compression wave (1) originating from the edge of the exposed electrode, and a weaker additional wave shifted to the side, having a somewhat lower speed (4). This wave pattern corresponds to the distribution of the heat release in two regions - one small region (2) with higher energy density at the edge of the exposed electrode, and another longer region (3) with lower energy density. Several numerical studies have shown energy release distribution produces wave patterns similar to ones observed in experiments [63, 71].

Conclusions Experimental observations show a clear cross-sectional variation in the discharge of the actuator, occurring on the scale of the actuator length. It therefore seems necessary to represent not only the location but the influence of the geometric length of the actuator during the flow simulations.

Temporal properties

On the fine scale, the temporal distribution of energy release is determined by the rates of plasmadynamic processes which convert the energy stored in the ionized state (plasma) to translational degrees of freedom of molecules via recombination, relaxation and reattachment. Such processes have been studied by plasma physicists, who have found that a large part of the energy is converted into thermal form in the period within about $1\mu\text{s}$ after the discharge [68]. The details of the energy release process are complex, but they occur at time scales well below whose to which the flow can respond.

Conclusions In view of the difference between the plasma dynamic and fluid dynamic time scales, it is proposed to model the temporal profile of energy release as uniform within the actuation time interval. It will be confirmed in chapters 6 and 5, that the details of the temporal distribution of the energy release influence the results only to a minor degree. In some experiments pulses are generated in a burst mode, as shown in the Figure 3.9. This mode could be modeled as a sequence of uniform pulses, but the repetition frequency of the pulses in a burst is still much higher than typical fluid-dynamic frequencies. This suggests the details of the energy release within the burst can also be decoupled from the fluid dynamic response, allowing the series of pulses to be replaced with a continuous equivalent energy release. This assumption will be investigated further in chapter 6.

Proposed model

Based on the observations above, it is proposed to model the effects of NS-DBD plasma actuation using a *pulsed volumetric spanwise-uniform heat source*. During each pulse, the energy transfer will be uniform in time, and uniformly distributed in the area of the flow domain adjacent to the actuator. The vertical dimensions of the area will be estimated from experimental observations of NS-DBD actuators operating with similar design parameters.

The total amount of energy deposited during a pulse will be based on experimental values, such as those determined in section 3.5. These were obtained by measuring current and voltage in the feeding cable, allowing the energy to be computed as:

$$E = \int_{-\infty}^{+\infty} I \cdot V \, dt \quad (4.1)$$

In general the time histories of I and V depend on the high voltage pulse generator, the voltage, and the actuator design. For the experiment considered in section 3.5, $E = 20 \text{ mJ}$. This value was found to be insensitive to the length of the actuator and external conditions.

The procedure for estimating total energy described above is prone to several sources of error, such as the effect of electromagnetic noise in the signal, the presence of signal reflections, as the uncertainty of how large a portion of input electric energy is effectively converted to the air's thermal energy in vicinity of the actuator. Thus this calculation can only be considered as a rough estimation.

Given the assumptions of a uniform spanwise distribution and the previously described discharge cross-sectional distribution, we can compute the volumetric

thermal source density as:

$$A = \frac{E}{V} = \frac{E}{LS} \quad (4.2)$$

where A is a volumetric thermal density, V is a discharge volume, L is an actuator length and S is the discharge cross-section. In the experiment described in [63] $S \approx 0.5 \times 0.5 \text{mm}^2$. This gives, for example, for an actuator length of $L = 40 \text{cm}$:

$$A = 10^5 \frac{\text{J}}{\text{m}^3} \quad (4.3)$$

The effect of the actuator on the flow will be computed using the compressible Navier-Stokes equations, with the pulsed volumetric spanwise-uniform heat source represented as a source term in the energy equation. The compressible Navier-Stokes equations consist of a scalar equation expressing conservation of mass, a vector equation for the conservation of momentum, and a scalar equation for the conservation of energy. An additional equation of state links the pressure to density and temperature of the medium. This system can be written as:

$$\begin{aligned} \frac{d\rho}{dt} + U\nabla\rho &= 0 \\ \frac{d(\rho U)}{dt} + U\nabla(\rho U) &= \nabla(\mu\nabla U) - \nabla p \\ \frac{d(\rho E)}{dt} + U\nabla(\rho E) &= \nabla(\alpha\nabla T) - \nabla(U p) + S_E \\ p &= P(\rho, T) \end{aligned} \quad (4.4)$$

where ρ is fluid density, U is fluid velocity, μ is dynamic viscosity coefficient, E is total energy per unit mass, α is a thermal conductivity coefficient, p is pressure, T is temperature. The term S_E is the energy source term used to represent the actuator. This is zero everywhere in the flow domain except within within the discharge cross-section region S , where it has a constant value.

Numerical implementation aspects

The model described above makes no explicit assumptions on the state of the flow being laminar or turbulent. In principle it could be applied in either condition, but in practice issues of resolution, particularly for the turbulent flow case, constrain what can be represented. Aside from the issues of actuator modeling, current computing hardware is incapable of directly simulating the large range of scales present in turbulent flows, except at very low Reynolds numbers. For the high Reynolds numbers of interest in flow control applications, this leads to two

alternatives. In the first, called large-eddy simulation (LES) the largest scales of turbulence are resolved, while the effects of the unresolved scales (which represent the majority of the wave number range) are represented with a turbulence model, known as a sub-grid scale (SGS) model [53–55]. In the second, known as the Reynolds-averaged Navier-Stokes approach (RANS), the effects of all turbulent fluctuations on the mean are represented by a model for the Reynolds stress tensor [8, 16, 33, 66].

Application of the proposed model for the NS-DBD actuator within a LES introduces approximations that are difficult to quantify if the resolved turbulent scales are smaller than the discharge cross-section. On the other hand, application of the actuator model in a RANS computation does not lead to scale separation issues, but does require that the model for the Reynolds-stress tensor be recalibrated or reformulated to have the correct response to the actuator's input. Pursuing either of these alternatives would require a significant research effort, both on the numerical and experimental side. Given all mentioned above, special care shall be taken while running RANS or LES simulations with an actuator model. Calibration of the actuator model and turbulence model are considered necessary for every case. Additionally, such simulations tend to be sensitive to quality of the mesh, which acts in the simulations as a spatial filter limiting the resolved scale ranges. Several examples of such simulations are considered in [Appendix A](#). To limit the scope of the present work, we will thus limit the application of the proposed model to laminar regions of the flow.

Even with this restriction, there are still strict temporal and spatial resolution requirements which must be maintained. To adequately resolve the compressible effects induced by the actuator, such as creation and propagation of the compression wave, the time step should satisfy a CFL (Courant-Friedrichs-Lewy) criterion based on the speed of sound in the medium:

$$\Delta t < \frac{\Delta x}{u_s} \quad (4.5)$$

where u_s is the speed of sound. For example, given a desired spatial resolution at the location of the actuator of $\Delta x = 0.05$ mm (such as the spatial resolution is at least 10 times smaller than the size of the discharge volume) the estimated maximum time step is $\Delta t \approx 1.7 \cdot 10^{-7}$ s.

The required spatial resolution is determined by the two considerations: the size of the discharge itself and the need to resolve flow features which emerge in nearby laminar boundary or shear layers. As the typical spatial scale of the discharge is about 0.5 mm in the wall-normal direction, a resolution of about 1/10 of the discharge region size is required for representing the formation of the compression wave and resolving the distribution of energy.

Chapter 5

NS-DBD actuator in a laminar boundary layer

In this chapter, the model of the NS-DBD actuator is applied to the case of a laminar boundary layer on a flat plate. First, the results are compared to those from an experiment with similar conditions, demonstrating that the model is capable of reproducing the dominant flow responses associated with NS-DBDs. Then, a POD analysis of the simulation data is compared to the results of linear stability theory. This demonstrates that the actuator produces flow disturbances which are primarily in the form of Tollmien-Schlichting waves. This implies that the main effect of the actuator is the excitation of natural instability modes, which evolve according to the standard stability properties of the boundary layer.

Introduction

NS-DBD (nanosecond dielectric barrier discharge) plasma actuators have been shown to be effective for postponing laminar leading edge separation on airfoils. One of the possible mechanisms of this effect is the tripping of laminar boundary layer, although the manner in which this is accomplished has been unknown to date.

In this chapter, simulations of the response of a laminar boundary layer to NS-DBD actuation will be performed using the model for the actuator developed in the previous chapter. The latter is implemented as a pulsed volumetric source

Work presented in this chapter was done at TUDelft with financial support from Plasma Technology Developemnt BV. Parts of this chapter have been published in [\[56\]](#)

term in the energy equation of the compressible Navier-Stokes equations. The amount of energy deposited is derived from electrical measurements of the energy in the high-voltage pulse, while the geometry of the discharge is derived from experimental observations. The spatial distribution of the energy input is based on experimental observations and results of plasmaphysical studies. First the simulations are validated using experimental data, and then the mechanisms by which actuation effects the laminar boundary layer are investigated.

Simulation setup

Simulation domain

The domain used for the simulations, shown in [Figure 5.1](#), resembles the setup of the experiment described in paper [11]. Along the lower boundary of the domain the geometry of a flat plate was defined a super-elliptic leading edge [46]. The half-thickness of the plate was 6 mm. The length of the super-elliptic part of the plate was 36 mm, followed by a flat part with length of 150 mm. As in the experiments, the simulations used a zero angle of attack inflow with free-stream velocity of 5 m/s.

The base mesh used was a structured mesh of quadrilaterals with 110.5 k cells. The size of the first near-wall cell was $h_1 = 4 \cdot 10^{-5}$ m, which corresponds to $y_1^+ = 0.24$ wall units in the middle of the observation region.

The simulation used the 2D laminar compressible Navier-Stokes equations (without any turbulence model). As the experimental results showed the formation of coherent spanwise vortex structures within the extent of the domain as a response to actuation, the simulation was performed in 2D. Consequently, the simulation does not consider the transition itself, but rather only growth on disturbances in the laminar boundary layer before transition. Transition itself is essentially three-dimensional phenomena which falls out of scope of the current study.

On the surface of the plate, a no-slip boundary condition was applied. Non-reflecting boundary conditions were applied on the inlet, top and outlet boundaries. Mesh coarsening towards outflow boundary was used to damp strong gradients in order to limit the strength of reflections caused by multi-dimensional effects from vortices leaving the domain. For numerical method, a second order central differencing spatial discretization scheme and second order BDF2 time integration scheme (“backward” in OpenFOAM), were used along with the PISO coupling method.

In the reference experiments, the actuator was placed 25 mm downstream of the beginning of the flat part of the plate, and thus 61 mm downstream the

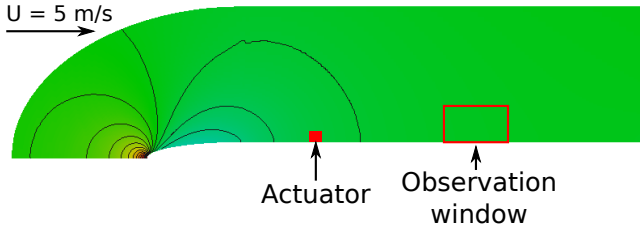


Figure 5.1: Simulation domain (with isobars and pressure in color).

leading edge of the plate (here x coordinates are given relative to the beginning of the flat part of the plate). The Reynolds numbers in the middle of the observation window were $Re_\delta = 391$ and $Re_\theta = 145$ based on the displacement thickness and momentum thickness, respectively. The observation window, where velocity fields were captured using PIV techniques, was located from $x = 60$ mm to $x = 100$ mm with a height of 17 mm. For the numerical simulations, the same positions of the actuator model and observation window were used.

Actuator model

The model of the NS-DBD actuator described in [chapter 4](#) was used, applied with the same burst discharge mode as used as in the experiment. Each burst, as illustrated in [Figure 5.2](#), consisted of a sequence of many pulses at a high frequency (in this case 50 pulses at 10 kHz). The duration of each pulse was set to $1 \mu\text{s}$, based on plasmaphysical considerations. As the pulse repetition frequency was much higher than typical fluid dynamic frequencies, each burst can be considered to be a single input to the flow.

In the following, we study the response to one single burst which starts at model time 1 ms and ends at 6 ms model time. We consider in particular the velocity profiles sampled along several wall normal lines placed between $x = 65$ mm and 95 mm, each spanning the wall-normal direction from the surface to a height of 17 mm. We also consider a time series analysis, with velocities sampled in several probe locations at a distance of 2 mm from the surface.

Comparison to experimental measurements

The results of the simulations are first compared to the *particle imaging velocimetry* (PIV) measurements described in [11]. PIV (particle imaging velocimetry) is an

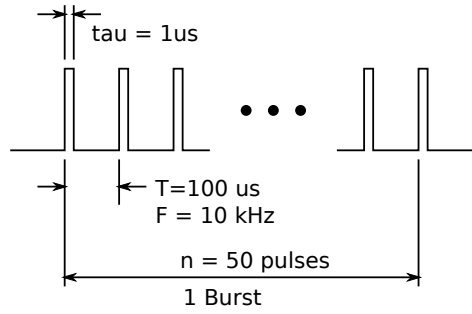


Figure 5.2: Burst mode of operation.

experimental method to measure instantaneous velocity fields of the flow using sequence of images of particles seeded in the flow and illuminated by a laser beam [2, 3, 64]. In [11], the velocity field was measured using PIV in the observation region at several time instants after NS-DBD actuation. The resulting snapshots of the velocity field are presented in Figure 5.3, together with simulation results for the same conditions.

For both the experiments and simulations, the propagation velocity of the disturbance was measured to be approximately $c = 2 \text{ m/s}$. The corresponding dominant wavelength of the disturbance was $\lambda = 21 \text{ mm}$, with an estimated dominant frequency of $f \approx c/\lambda = 95 \text{ Hz}$. The absolute values of the velocities were different. In the case of PIV measurements, the maximum magnitude of the vertical velocity component was about 0.3 m/s , while in the simulation the magnitude of the vertical velocity component disturbance was 0.18 m/s . The difference is likely due to uncertainty associated with estimating the energy input into the flow. This uncertainty includes measurement uncertainty in the amount of electrical energy transferred by the electric pulse into the discharge, the efficiency of the energy conversion by the discharge into the thermal form, and the uncertainty in the heat losses to the wall. In order to compare the phenomena qualitatively, however, the illustrated fields have each been normalized with their largest value of velocity magnitude. The images show that the position, speed, wavelength and shape of disturbances are very similar. They are also small enough in magnitude to presume that linear theory may be applicable for their analysis.

Comparison to linear stability theory

The natural instabilities of the laminar boundary layer are described by linear stability theory, which predicts flow responses in the form of Tollmien-Schlichting (TS) waves. These waves are either amplified or damped as they travel down-

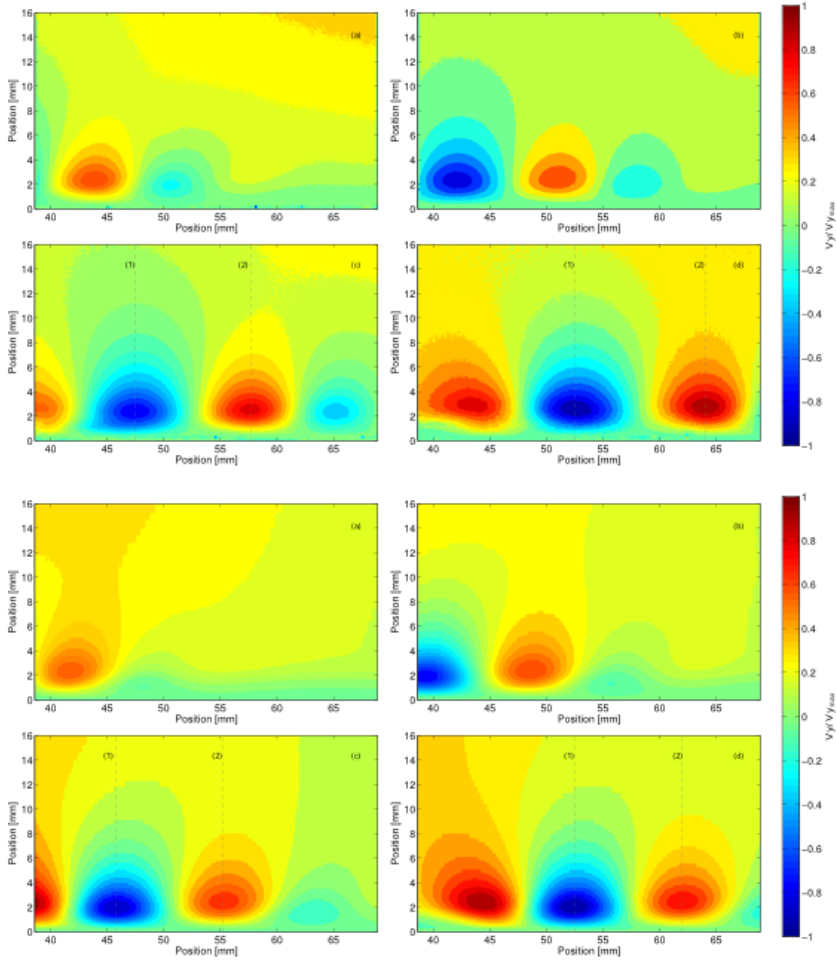


Figure 5.3: Flow field in observation window. Experimental PIV field (top) [11] and numerical simulations (bottom) at the same time instants.

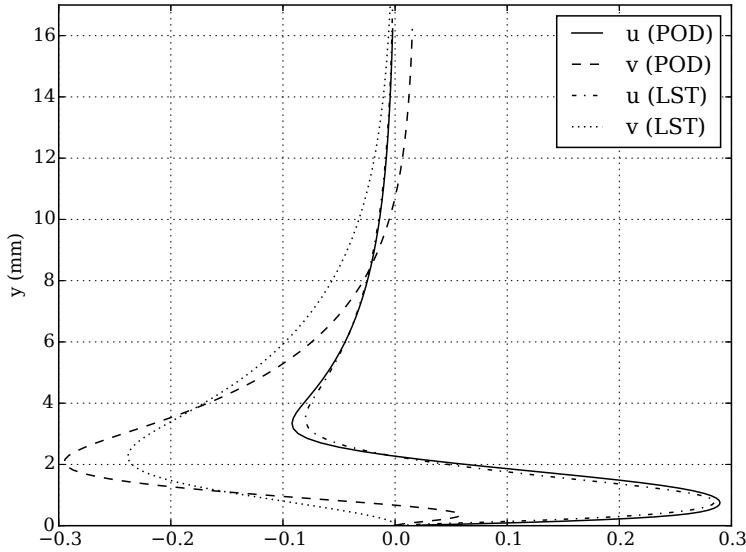


Figure 5.4: Comparison of the first POD mode and theory-predicted Tollmien-Schlichting wave at $x = 75$ mm and energy per pulse $E = 0.5E_0$.

stream. Once TS waves are amplified to large enough amplitudes, transition is initiated. It should be noted at this point that there are several other mechanisms for transition (see for example [18]). However, given the magnitude of the experimentally observed disturbances it is logical to first compare the simulated response to those induced by TS waves.

For each vertical profile ($x = \text{const}$), 200 snapshots of the velocity were recorded with equal time intervals of 10^{-4} s. These were then used for a Proper Orthogonal Decomposition (POD) [6] to extract the most energetic modes of the flow. The sampling was started after the end of the burst until the disturbance produced by the burst was convected downstream of the measurement window. The resulting mode shapes were compared to the shape of Tollmien-Schlichting waves predicted by solving the Orr-Sommerfeld equation for the Blasius boundary layer at the least stable frequency. The result of the comparison is presented in Figure 5.4.

The curves show a good agreement, with only some minor differences. It should be noted, however, that the procedure and assumptions used when determining modes via a POD differs from those used when determining modes from linear stability theory. The procedure and assumptions for linear stability

theory (LST) are:

1. The flow is considered to be incompressible, two-dimensional (span-wise uniform) and parallel.
2. The stream function of the flow is decomposed into sinusoidal waves:

$$\phi = \phi(y)e^{i(\omega t - \alpha x)} \quad (5.1)$$

3. The Navier-Stokes equations are linearized about mean flow field, yielding Orr-Sommerfeld equation:

$$\frac{1}{iRe\alpha} \left(\frac{d^2}{dy^2} - \alpha^2 \right)^2 \phi = (U - c) \left(\frac{d^2}{dy^2} - \alpha^2 \right) \phi - U'' \phi \quad (5.2)$$

4. For every temporal frequency ω a spatial stability problem is solved to obtain complex wavenumbers $\{\alpha\}$ (as eigenvalues) and corresponding mode shapes (as eigenvectors).

The procedure for the POD employs snapshots of the flow field obtained from a 2D Navier-Stokes simulation $\{U(t_i)\}$, which are not strictly parallel. These are used as columns in a matrix $A = (U(t_i))$. The POD is then defined by the singular value decomposition (SVD) of the matrix A or, equivalently, by eigen decomposition of the correlation matrix $C = A^* A$. As a result, there are several potential sources of discrepancy between LST and POD of simulation data:

1. The assumption of incompressibility.
2. The effects of linearization.
3. The assumption of parallel flow.
4. The difference between the POD and the eigenfunction analysis of the Orr-Sommerfeld equation.
5. Numerical errors of the simulation.

In the following sections we will address these potential sources of error one by one.

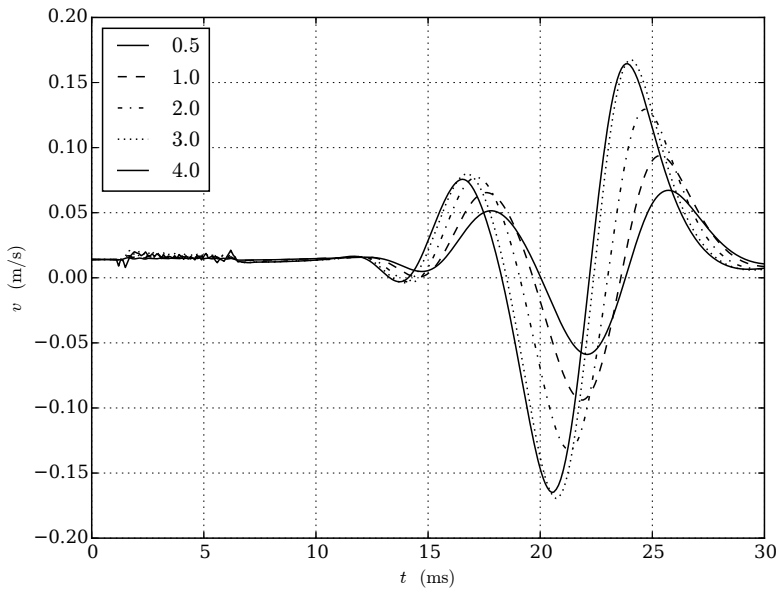


Figure 5.5: Comparison of time evolution of flow velocity in simulation for different discharge energies.

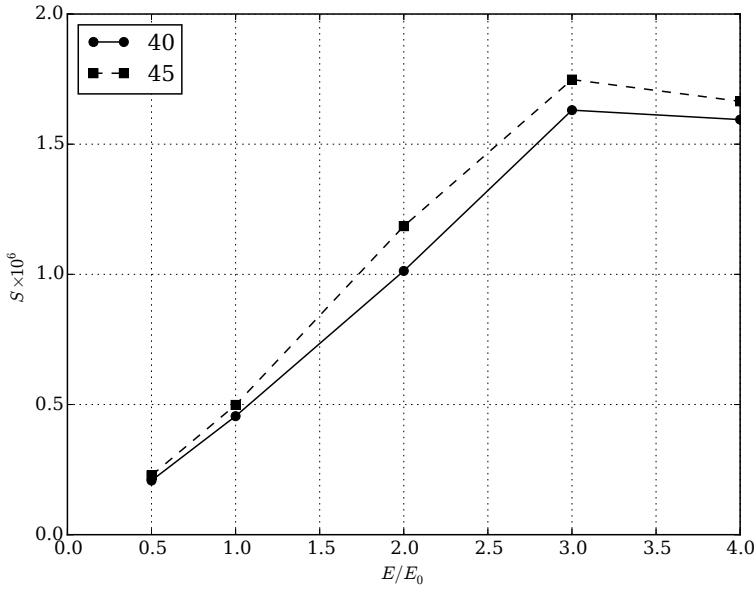


Figure 5.6: Dependence of the squared-velocity integral S on the input pulse energy for positions 40 and 45 mm downstream the actuator ($x = 65$ mm and $x = 70$ mm correspondingly). Profiles in Figure 5.4 are computed for $E/E_0 = 0.5$, well below the linearity threshold.

Linearization error

To estimate linearization error we can compare results of the simulation with different modeled pulse energies. Time evolution of flow velocity for several discharge energies is presented in Figure 5.5.

To quantify the disturbance in the flow, we can use integral of the velocity disturbance squared over the vertical profile, which reflects total kinetic energy of the disturbance

$$S = \int \left(U(x, y, t) - \bar{U}(x, y) \right)^2 dt dy. \quad (5.3)$$

The dependence of the value of S on the input energy per pulse for two different positions is presented in the Figure 5.6. In the range of energies from 0.5 to 3.0 the response is linear, but after that there is saturation. As a result, for actuation with $E/E_0 < 3.0$ the linearization error is expected not to be large.

Parallel flow assumption

Linear stability theory assumes the flow is parallel. For the case considered, the shape of the model (thick flat plate with super-elliptic leading edge) makes the flow non-parallel in the region close to the leading edge. At the point where the actuator is placed (25 mm downstream the beginning of the flat part of the plate), at the wall distance 2 mm, the vertical component of the velocity in the unactuated case is $v = 0.02$ m/s, which is still very small compared to the horizontal component $u = 4.65$ m/s. This implies the parallel flow assumption is not a significant source of error in the comparisons.

The difference between the POD and LST analysis

Assuming the flow is parallel, the disturbance can be decomposed into harmonic waves written as (using complex notation):

$$U(x, y, t) = U_0(y)e^{i(\omega t - \alpha x)} \quad (5.4)$$

For simplicity we will use the correlation matrix notation, and our POD will be done at only one x location. In this matrix, each element is an inner product of the pair of snapshots:

$$M_{ij} = (U(t_i) \cdot U(t_j)) = \int U^*(x, y, t_i)U(x, y, t_j) \, dy \quad (5.5)$$

where star (*) denotes complex conjugate.

Let's further assume that the flow field consists of only one wave of the form (5.4) and the time instants at which snapshots are taken are equally spaced, $t_i = i\Delta t$. Thus

$$\begin{aligned} M_{ij} &= \int |U_0(y)|^2 e^{-i(\omega t_i - \alpha x) + i(\omega t_j - \alpha x)} \, dy \\ &= \|U_0(y)\|^2 e^{i\omega(t_j - t_i)} \\ &= \|U_0(y)\|^2 e^{i\omega(j-i)\Delta t} \end{aligned} \quad (5.6)$$

Consider the eigenvalue problem for this matrix:

$$M\phi = \lambda\phi \quad (5.7)$$

For this particular matrix (5.6) the solution can be found analytically in a following form:

$$\phi_j = e^{-i\omega\Delta t j} \quad (5.8)$$

Then, substituting it into (5.7) and taking into account (5.6):

$$\begin{aligned}
 (M\phi)_i &= \sum_j M_{ij}\phi_j \\
 &= \sum_j \|U_0(y)\|^2 e^{i\omega\Delta t(j-i)-i\omega j} \\
 &= \|U_0(y)\|^2 \sum_j e^{-i\omega i\Delta t} \\
 &= n \|U_0(y)\|^2 e^{-i\omega i\Delta t} \\
 &= \lambda\phi_i
 \end{aligned} \tag{5.9}$$

we can conclude that

$$\lambda = n \|U_0(y)\|^2 \tag{5.10}$$

where n is the number of snapshots used and thus the size of the matrix M . The mode shape can be reconstructed as follows:

$$f(y) = \sum_k \phi_k U(y, t_k) = U_0(y) e^{-i\omega k\Delta t + i\omega k\Delta t} = U_0(y) \tag{5.11}$$

The result means that in the case there the flow field consists of only one harmonic wave, the POD procedure recovers that wave exactly, and the result should coincide with the linear stability theory.

Thus, if the flow is parallel, the disturbances are small enough to be linear, and the first mode dominates the response, the POD and LST will lead to the same first mode shape. To check the last assumption, the magnitudes of the singular values determined by the POD are considered. The spectrum is shown in the [Figure 5.7](#). The ratios of the first three eigenvalues are

$$\lambda_1/\lambda_2 = 3.12 \tag{5.12}$$

$$\lambda_2/\lambda_3 = 22.9 \tag{5.13}$$

and the fraction of energy containing in the first two modes

$$E_1/E_{\text{tot}} = \lambda_1/\sum \lambda_i = 0.693 \tag{5.14}$$

$$E_2/E_{\text{tot}} = \lambda_2/\sum \lambda_i = 0.274 \tag{5.15}$$

From POD theory, it is known that for periodic motion eigenvalues come in pairs, each pair corresponding to one harmonic mode. Thus, both first and second eigenvalues correspond to one wave, with an energy fraction

$$(E_1 + E_2)/E_{\text{tot}} = (\lambda_1 + \lambda_2)/\sum \lambda_i = 0.967 \tag{5.16}$$

This implies that the disturbances can be approximated as unimodal, for which the POD should produce modes similar to those obtained from LST, making their comparison justified.

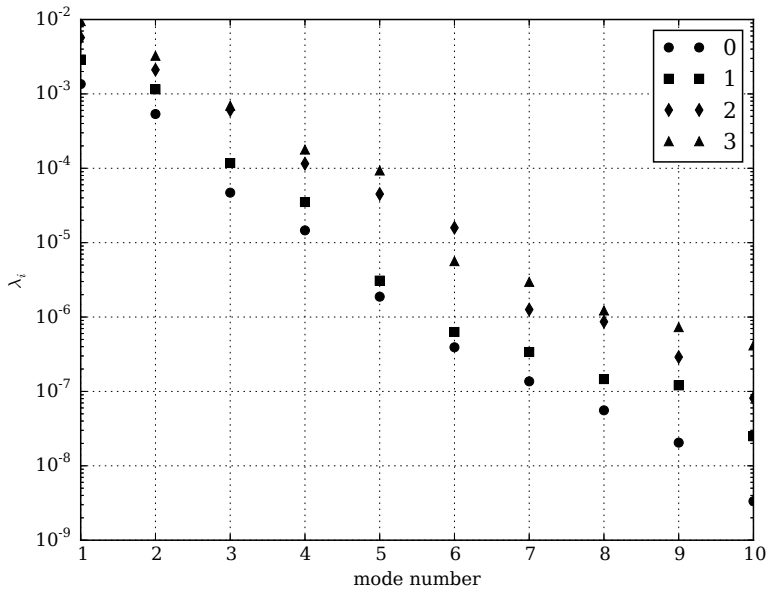


Figure 5.7: First ten POD eigenvalues of the simulation flow field at $x = 65\text{mm}$ and different energy per pulse values: 0 — $E/E_0 = 0.5$; 1 — $E/E_0 = 1.0$; 2 — $E/E_0 = 2.0$; 3 — $E/E_0 = 4.0$.

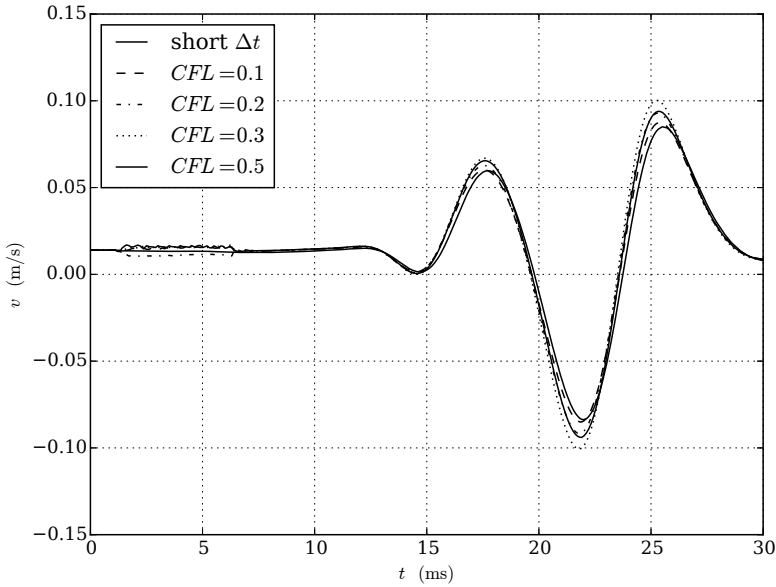


Figure 5.8: Comparison of time evolution of flow velocity in simulation for different time steps.

Numerical errors of the simulation

Numerical errors can be assessed by studying solution convergence with cell size and time step. The results of these studies are presented in [Figure 5.8](#) and [Figure 5.9](#). It can be seen that in the range $CFL < 0.5$ change of time step does not influence the results of the simulation. Similarly, the analysis of the cell size study shows that the results of the simulation do not change with mesh refinement. Thus the mesh resolution is considered satisfactory for the simulation.

Conclusions

In the current chapter we applied the proposed NS-DBD actuator model to numerical simulations in a laminar boundary layer, and compared the results to experimental data. Good qualitative agreement was found for the mode shapes of the resulting fluid dynamic responses. Direct comparison of the magnitudes was hampered by uncertainties in the determination of the total energy added to the flow.

Motivated by the generally small disturbance amplitudes in the experimental

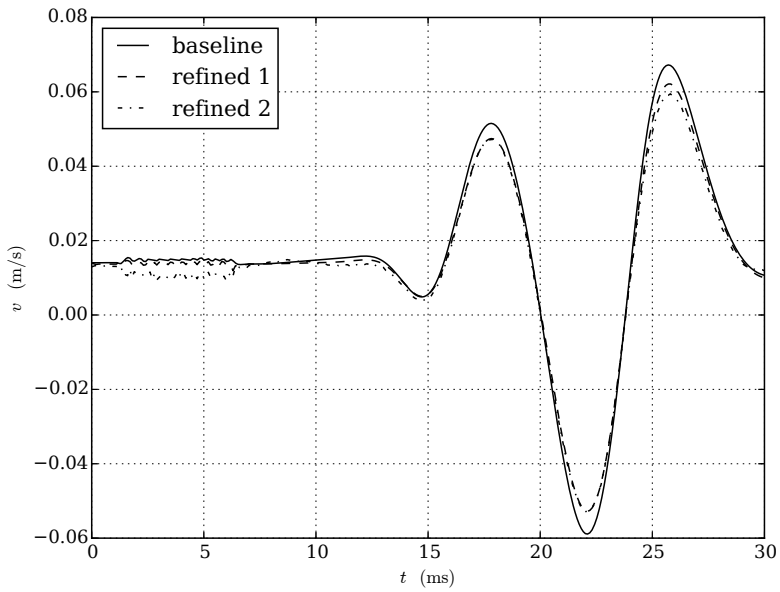


Figure 5.9: Comparison of time evolution of flow velocity in simulation for three different meshes.

results, the results from representative simulations were also compared to those of linear stability theory. Specifically, modes identified from a POD analysis were compared to Tollmien-Schlichting waves predicted by solving the Orr-Sommerfeld equation. The correspondence was good, which implies that the flow control mechanism observed in the experiments is due to the excitation of natural instability modes in the flow.

Chapter 6

Dynamics of disturbances in a free shear layer introduced by NS-DBD plasma actuator

Given the performance of the actuator for the promotion of transition of laminar boundary layer as discussed in [chapter 5](#), the NS-DBD actuator appears to be effective as a non-intrusive boundary layer trip. Another application of this effect can be used for the transition of a laminar shear layer. This application is important in practical applications for laminar leading edge separation control on airfoils. In this chapter we study the performance of the NS-DBD actuator in this context.

Introduction

Recent experiments with nanosecond dielectric barrier discharge (NS-DBD) actuators [\[63\]](#) have demonstrated their ability to influence airflow separation patterns at higher Reynolds numbers. The manner in which they do so, however, is not yet fully understood. A number of mechanisms for their effectiveness have been proposed, including the promotion of boundary layer transition, the induction of a small but critical change of momentum, and the promotion of instabilities in the shear layer adjacent to the separated region. This chapter focuses on the last of these proposed mechanisms, motivated by the experimental observation of large coherent structures appearing in shear layers following NS-DBD actuation.

Work presented in this chapter was done at TUDelft with financial support from NEQLab research BV and Plasma Technology Development BV. Parts of this chapter have been published in [\[57\]](#)

The geometry of the coherent structures observed in [38] can be related to the geometry of the actuator, which was constant along the span of wing tested. As a result, the initial behavior of the shear layer prior to break-up appeared to be two-dimensional. In order to study the effect of NS-DBD actuators in the absence of other factors present in the experiment, a generic two-dimensional laminar shear layer problem is proposed. As it is known that NS-DBD discharge produces a significant shock wave [1, 63], compressible Navier-Stokes simulations are employed for its investigation.

The layout of the chapter is the following: The actuator model is discussed in section 6.2. Then the simulation setup is described in section 6.3. The results are presented and discussed in section 6.4. Finally, conclusions are given in section 6.5.

Actuator model

As discussed in chapter 4, the modeling of the actuator in current work is focused on thermal effects. The actuator is modeled as a enthalpy source, with distribution constant in square discharge area of size 0.5 by 0.5 mm. The density of the enthalpy output is estimated given the total energy input to the discharge (directly determined in experiments by measuring voltage and current of the incident and reflected pulses in the feeding coaxial cable) and the approximate volume of the discharge. The base value used in the present work is an energy density per pulse of $A = 10^5 \text{ J/m}^3$, corresponding to a linear energy per unit span of $E \sim 25 \text{ mJ/m}$.

For the current simulations, the energy input is assumed to be uniform in time during energy deposition period τ . A value of $1 \mu\text{s}$ was used according to kinetic model estimations [68] and previous measurements. This actuation was repeated with period T , with the corresponding repetition frequency F being in the range 100–1500 Hz, corresponding to the range used in experiments [13]. In all cases shown, the first discharge occurs 1 ms after the start of the simulation.

Simulation description

The simulation domain is a square two-dimensional box with outer dimensions of $0.2 \text{ m} \times 0.2 \text{ m}$. On the inflow boundary, the following velocity profile is applied:

$$U(y)|_{x=0} = \frac{1}{2}(U_1 + U_2) + \frac{1}{2}(U_2 - U_1) \tanh \frac{y}{d} \quad (6.1)$$

where U_2 and U_1 are free-stream flow velocities above and below the shear layer, and d is a shear layer thickness parameter. In the current work, the values used

were: $U_2 = 30\text{ m/s}$, $U_1 = 5\text{ m/s}$, $d = 0.25\text{ mm}$, which roughly correspond to the experimental conditions.

The momentum thickness of the shear layer is defined as

$$\theta = \int_{-\infty}^{\infty} \frac{U - U_1}{U_2 - U_1} \left(1 - \frac{U - U_1}{U_2 - U_1} \right) dy \quad (6.2)$$

for the inlet profile θ is equal to $d/2 = 0.125\text{ mm}$. This gives a value for the Reynolds number of

$$Re = \frac{(U_2 - U_1)\theta}{\nu} = 208 \quad (6.3)$$

which corresponds to an unstable shear layer. According to linear stability theory, the most unstable frequency is given by $f_n\theta/\bar{U} = 0.032$ which for the inlet profile gives $f_n = 4480\text{ Hz}$. Corresponding wavelength is $\lambda = \bar{U}/f = 3.9\text{ mm}$.

On the remaining boundaries of the simulation domain, wave transmissive boundary conditions were used. Strong mesh coarsening was also applied in the vicinity of these boundaries, to ensure that vortical structures were dissipated before leaving the domain.

The high resolution core of the mesh had a length of 30 mm in the flow-wise direction, and a width of 10 mm. This size allowed for the formation of vortices, but ended before the first vortex pairing occurs. No refinement was used downstream of the core domain makes little sense, since in reality this area would contain strong 3D effects and a transition to 3D turbulence, which would be missed by a 2D simulation. The influence of the downstream region on the dynamics in the core region was quantified using comparisons with simulations using a longer core region. These have shown that there are no significant effects if downstream coarsening begins after position $x = 25\text{ mm}$. The region of interest was thus limited to $x \in [0, 25]\text{ mm}$, $y \in [-5, 5]\text{ mm}$.

Three different meshes were used in order to study the convergence of the simulation with increasing refinement. The number of cells in the default mesh was 135K cells, the low-resolution mesh consisted of 33750 cells, and the high-resolution mesh consisted of 540k cells. The layout of the meshes is shown in the [Figure 6.1](#).

For the results presented here, there were no sources of instability excitation other than the actuation and the natural feedback from the evolving shear layer. The initial condition used for each of the simulations was the same, and was obtained as a result of separate long simulation without actuation.

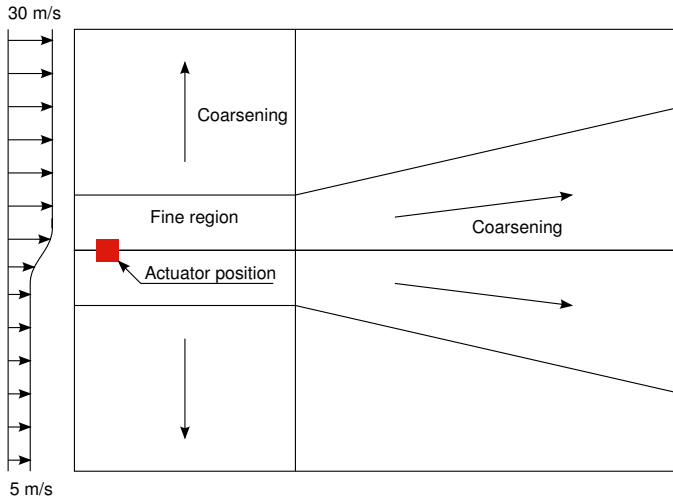


Figure 6.1: Simulation domain layout. The inlet is on the left side of the domain.

Results

Acoustic wave

The first phenomena which appears in simulation after the actuation is an acoustic wave. Using “numerical microphones” (e. g. recording pressure in specified points as a function of time), arrival times of the wave at different positions were used to estimate the wave propagation velocity along the midline of the shear layer. The results are presented in figure [Figure 6.2](#).

In the [Figure 6.3](#), velocity is plotted vs. time for several positions, demonstrating propagation of the acoustic wave. The estimated values of the acoustic wave velocity (defined as distance between consecutive positions divided by propagation delay between these positions) lie between 360 and 400 m/s (the straight line on the figure represents constant velocity of 400 m/s).

Velocity oscillations and vortex structure

After the propagation of the shock wave, the flow field becomes disturbed. The perturbations grow while convecting downstream in the form of vortical structures. An example snapshot of the flow field is shown in [Figure 6.4](#). Vortex pairs formed by the actuation which are similar to what was observed in experiments [\[13\]](#).

[Figure 6.5](#), [6.6](#) and [6.7](#) show the time evolution of velocity at different positions (5 mm, 10 mm, and 20 mm) without actuation and with actuation at repetition

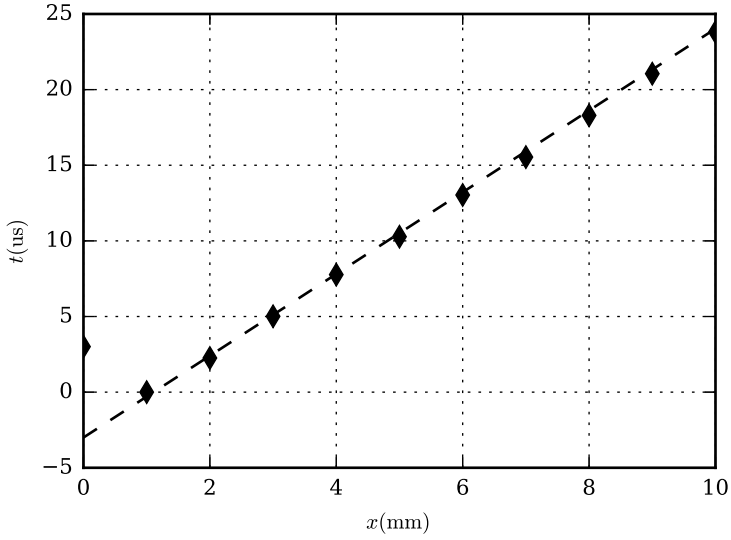


Figure 6.2: Wave arrival time vs. x . The dashed line corresponds to propagation velocity of $v = 370\text{ m/s}$.

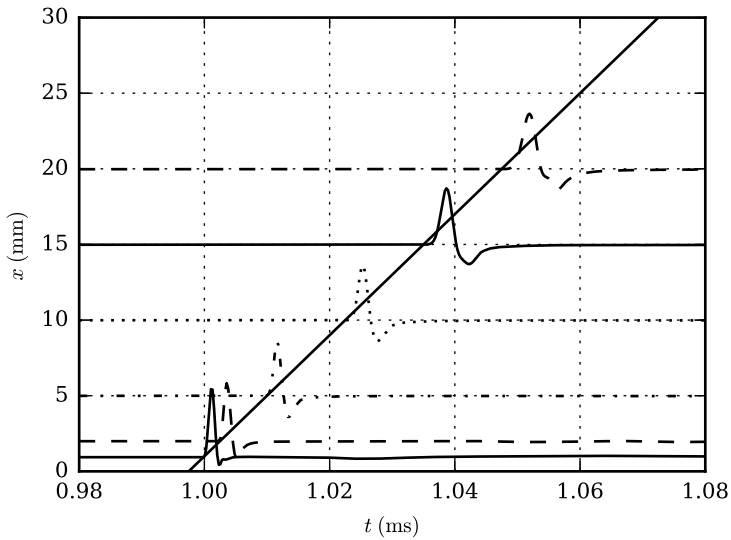


Figure 6.3: Propagation of the shock wave along the shear layer. The line indicates a constant velocity $c = 400\text{ m/s}$. For every position, normalized U is plotted over time.

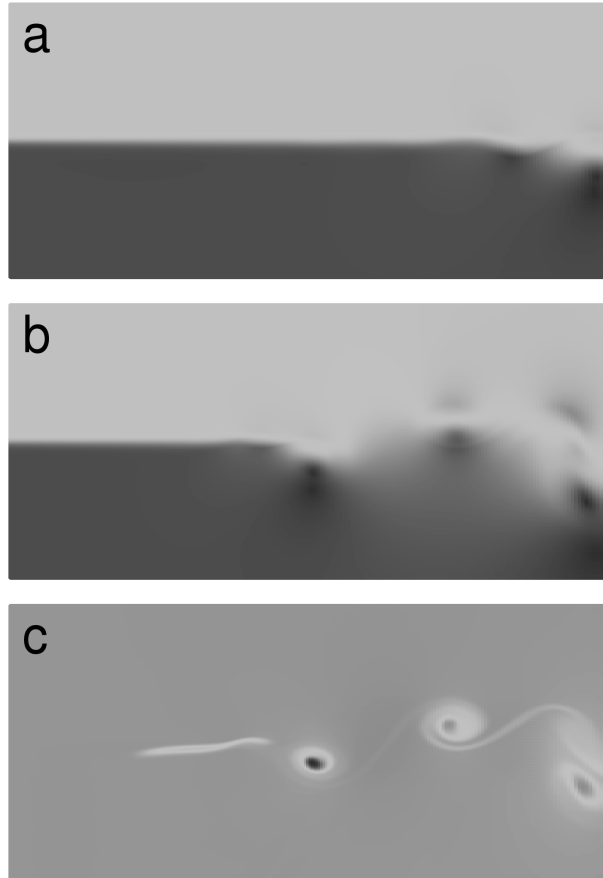


Figure 6.4: Snapshots of the flow field at time $t = 5$ ms. From top to bottom: a — magnitude of the velocity, reference case without actuation, b — magnitude of the velocity, actuation at 1000 Hz, c — density, actuation at 1000 Hz,

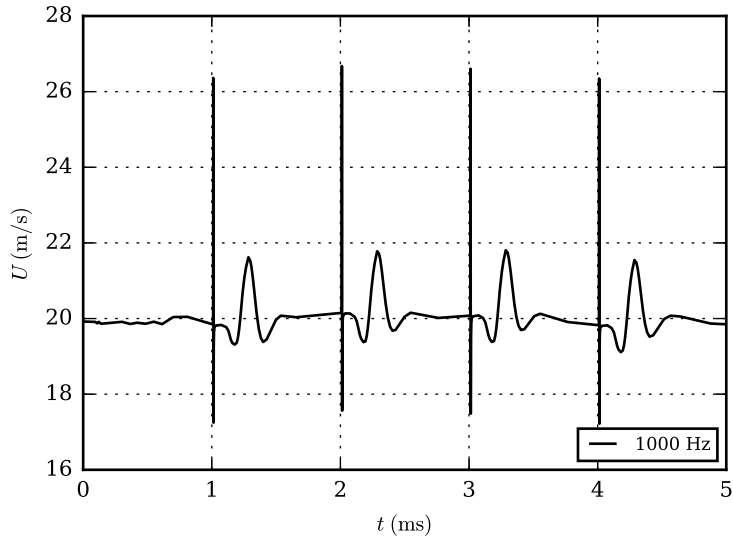


Figure 6.5: Comparison of the time evolution of the U component of the velocity at the point 5 mm far from the inlet on the midline of the shear layer. Top to bottom: actuation at 1500 Hz, 1000 Hz, 667 Hz, no actuation

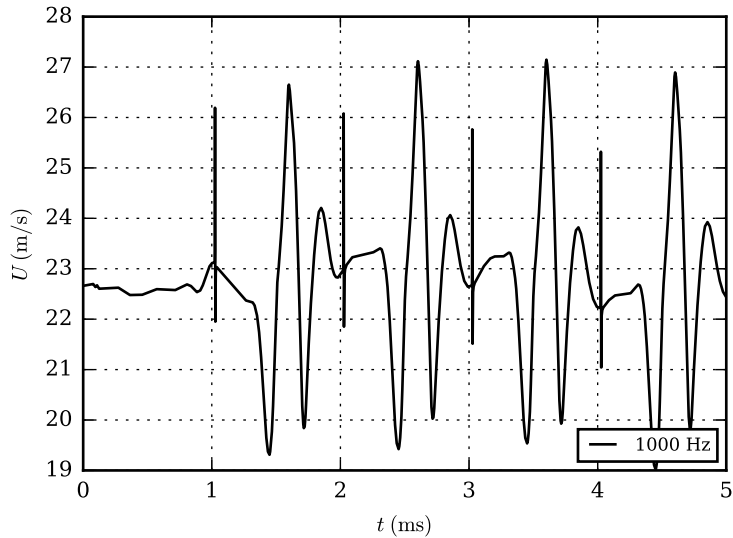


Figure 6.6: Comparison of the time evolution of the U component of the velocity at the point 10 mm far from the inlet on the midline of the shear layer. Top to bottom: actuation at 1500 Hz, 1000 Hz, 667 Hz, no actuation

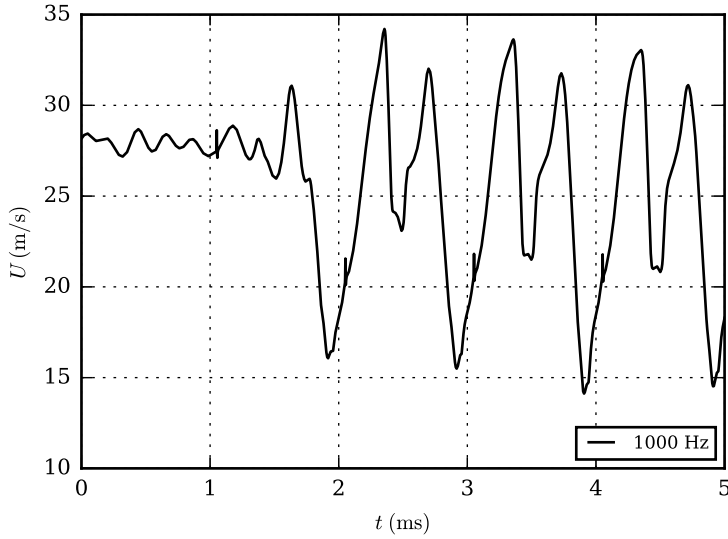


Figure 6.7: Comparison of the time evolution of the U component of the velocity at the point 20 mm far from the inlet on the midline of the shear layer. Top to bottom: actuation at 1500 Hz, 1000 Hz, 667 Hz, no actuation

frequencies of 667 Hz, 1000 Hz, and 1500 Hz. As can be seen on [Figure 6.5](#) (which corresponds to a point $x = 5$ mm) after each discharge (corresponding to a spike of velocity) the flow velocity experiences a perturbation. The shape of the perturbation does not depend on the repetition frequency, and is the same for every actuation repetition. Between actuation events the flow is undisturbed. This means that the flow structures created by the actuation event do not interact with each other at this location.

At the position $x = 10$ mm ([Figure 6.6](#)), the vortices produced at a repetition frequency 1500 Hz do start to interact with each other, but without changing their shape. At lower frequencies, the vortices remain separated from each other. Further downstream, at $x = 20$ mm, the vortices interact with each other at all three repetition frequencies. At this position the changes in shape are significant.

The described evolution corresponds well with that of a convected instability. [Figure 6.8](#) illustrates this by showing velocity versus time for several positions along the midline of the shear layer for one simulation. The propagation of the vortex could be seen, as well as its growth along the streamwise direction and eventual merging of individual vortices into a continuously disturbed flow. The straight lines indicate the propagation of the head and the tail of a single vortical perturbation, with speeds 25 and 11 m/s, respectively. Thus the mean velocity of

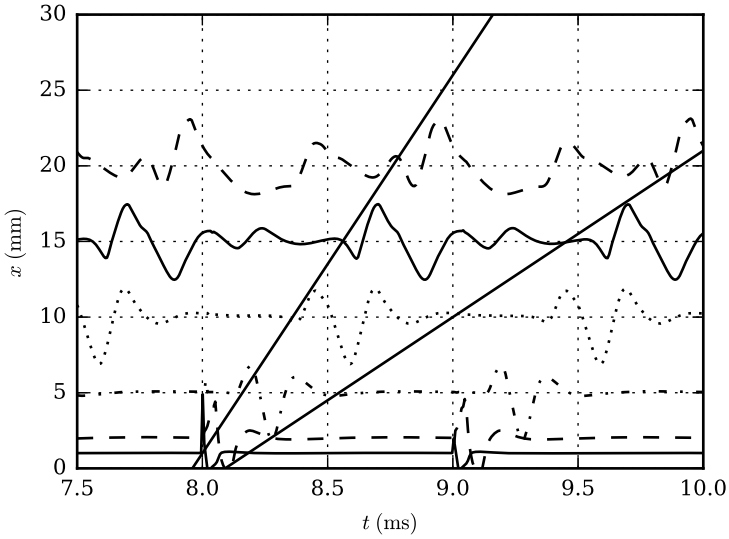


Figure 6.8: Propagation of the vortex structure along the shear layer. Lines indicate constant velocities $c = 11 \text{ m/s}$ and 25 m/s . For every position normalized U is plotted over time.

vortical disturbance propagation can be estimated as $\frac{1}{2}(25 + 11) = 18 \approx \bar{U}$. At this repetition frequency (1000 Hz) vortex interaction occurs after position $x \approx 15 \text{ mm}$.

Entropy spot

After the discharge, there is a region of heated air which is convected with the flow. The motion of this region is correlated with the motion of the main vortex structure formed by the actuator. This can be seen in [Figure 6.4](#) as a region with lower density. It is not clear for the moment if this “entropy spot” plays any role in determining the main effects of the actuator.

Flow statistics

The dependence of the momentum thickness of the shear layer on x is presented in [Figure 6.9](#). It can be seen that momentum thickness grows much faster in the case of actuation. The growth is initially dependent on actuation frequency, but at higher frequencies saturation occurs. This seems to be caused by the strong interaction of vortical structures in closely-spaced actuation events.

Components of the Reynolds stress tensor along the middle line of the shear layer are shown in figures [6.10–6.12](#). The change in RMS variations caused by

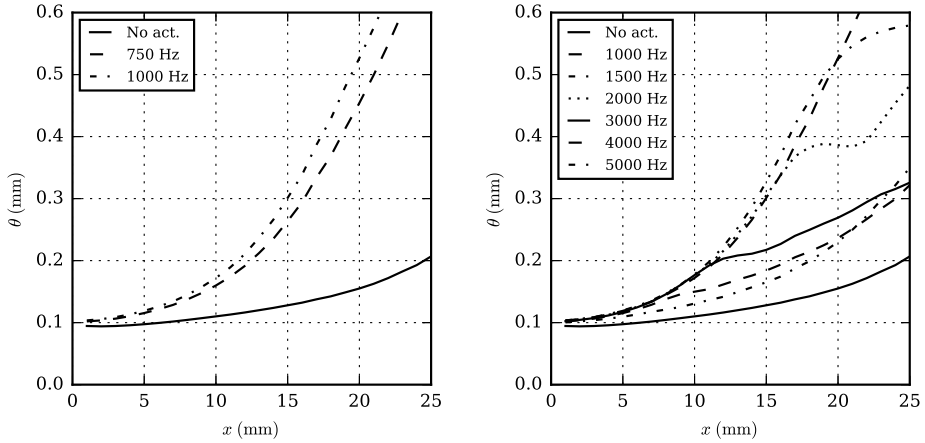


Figure 6.9: Comparison of momentum thickness growth for cases without actuation and with actuation at different actuation frequencies.

actuation is particularly significant. It can be seen that at lower actuation frequencies ($F \leq 1000$ Hz) the growth of shear layer (as indicated both by momentum thickness and Reynolds stress) is monotonic. At higher frequencies there is a point after which the growth of shear layer slows, and the Reynolds stresses stop increasing. The higher the actuation frequency, the closer this effect is to the inlet. This can also be attributed to vortical structures caused by individual actuation events interacting with each other.

Comparison with linear stability theory

Given the results of [chapter 5](#), it may be anticipated that the primary effect of NS-DBD actuation in a boundary layer is the excitation of natural instability modes. We would like to know if the same applies to the free shear layer case. The computed disturbance growth rate in the frequency domain is therefore calculated for the current problem and compared to linear stability theory.

Figures [6.13](#) to [6.16](#) show spectra of the computed velocity without and with actuation, at different repetition frequencies. In the absence of actuation, the spectrum is continuous and there are no preferential frequencies. Once actuation is applied, almost all of the energy becomes contained in multiples of the actuation frequency. For smaller value of x ($x = 5$ mm), the envelope of the spectrum has a maximum at about 4–5 kHz, independent of the actuation repetition rate. This corresponds to the most unstable frequency of inlet shear layer profile. At positions further downstream, the maximum of the envelope of the spectrum

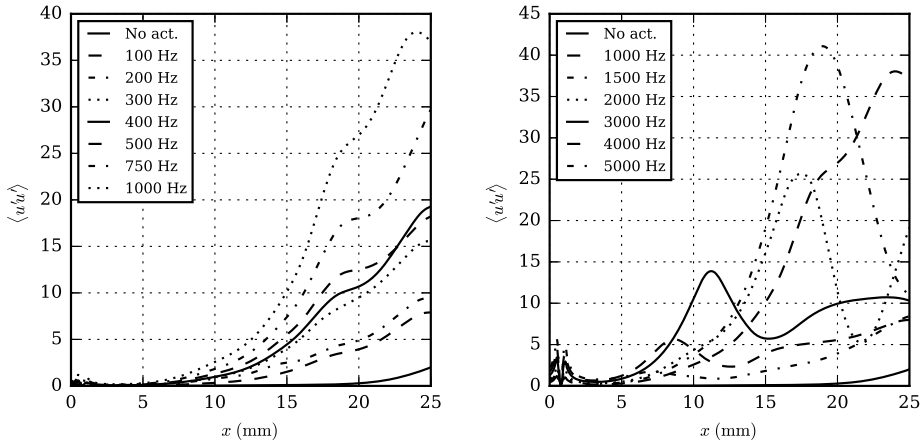


Figure 6.10: Reynolds stress component $\langle u'u' \rangle$ along the midline of the shear layer for cases without actuation and with actuation at different frequencies.

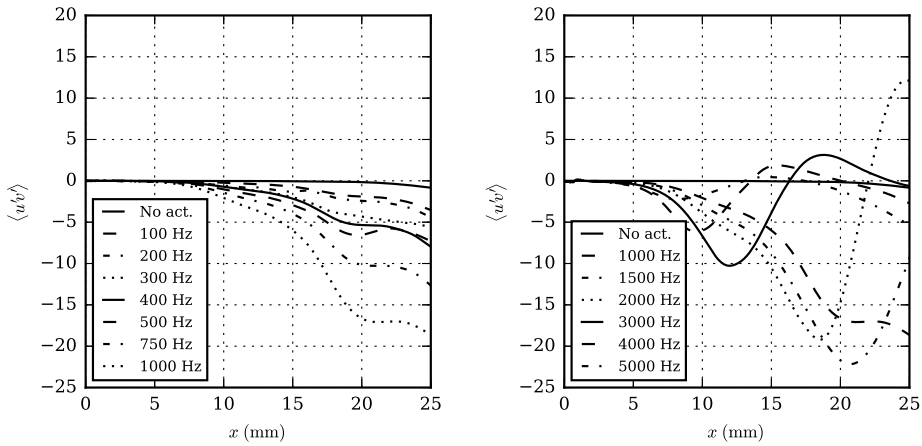


Figure 6.11: Reynolds stress component $\langle u'v' \rangle$ along the midline of the shear layer for cases without actuation and with actuation at different actuation frequencies.

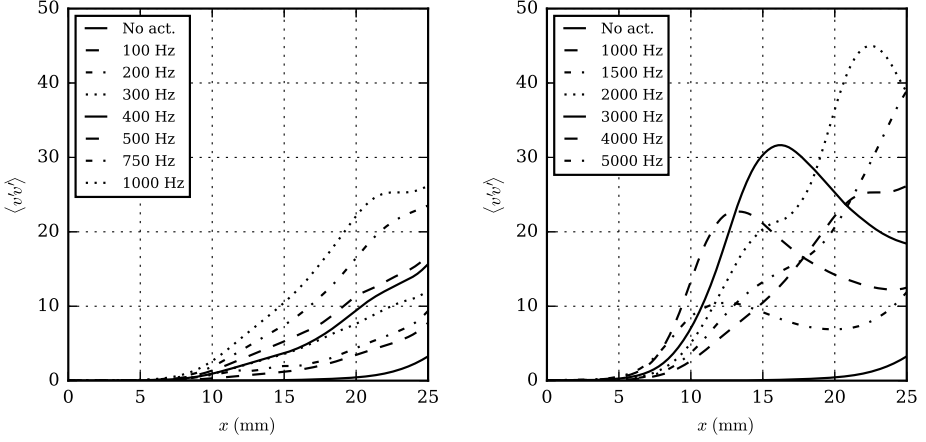


Figure 6.12: Reynolds stress component $\langle v'v' \rangle$ along the midline of the shear layer for cases without actuation and with actuation at different actuation frequencies.

shifts towards lower frequencies.

To compare the results more closely with linear stability theory, spatial growth rate coefficients have been determined from the computed results. In linear stability theory, the disturbance to the mean flow is expressed in the form

$$\psi(x, y, t) = \phi(y)e^{i(ax - \omega t)} \quad (6.4)$$

where a is a spatial wavenumber and ω is an angular frequency. To identify these waves in the computed results, a Fourier transform in time is used:

$$U(x, t) = \sum_j \hat{U}_j(x)e^{i\omega_j t} \quad (6.5)$$

where $\omega_j = 2\pi j f_0$, f_0 is the spectral resolution, and $\hat{U}_j(x)$ is Fourier component corresponding to frequency component number j . Given the Fourier transforms of the velocity at two points x and $x + \Delta x$, the complex wavenumber of j th frequency component can be estimated using

$$a_j = \frac{\partial}{\partial x} \log \hat{U}_j \approx \frac{\log \hat{U}_j(x + \Delta x) - \log \hat{U}_j(x)}{\Delta x} \quad (6.6)$$

and the growth rate using

$$g_j = -\text{Im } a_j \quad (6.7)$$

Linear stability theory is normally expressed in terms of the non-dimensionalized growth rate $g\theta/R$ (where $R = (U_2 - U_1)/(U_2 + U_1)$) and the Strouhal number $St =$

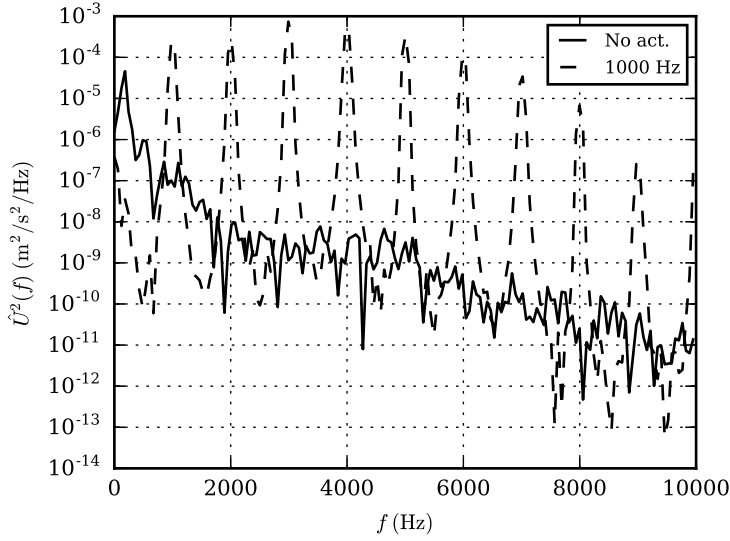


Figure 6.13: Spectra of the U component of the velocity at a point 5 mm downstream of the inlet on the midline of the shear layer.

$f\theta/\bar{U}$. According to the theory, all the Strouhal numbers from 0 to 0.079 are unstable, the most unstable being $St = 0.032$ [25]. This depends only marginally on R . The growth rate of the most unstable frequency is approximately $g_n\theta/R \approx 0.1$. Theoretical growth rates are calculated by solving Orr-Sommerfeld equation [7] based on a mean velocity profile obtained in simulations.

Growth rates observed in the simulation and predicted using linear stability theory (LST) at locations $x = 3, 5, 7$ and 10 mm are compared in Figure 6.17. Here the growth rates are computed and plotted for frequencies which are harmonics of the actuation frequencies. The unactuated plot indicates the level of uncertainty associated with the computational procedure of growth rate determination. It can be seen that the growth rates show good correspondence with the theoretical predictions within the level of uncertainty, especially at smaller x locations. Downstream of $x = 10$ mm the growth rates (not shown in the figures) deviate significantly from the theoretical values due to non-linear effects. These effects appear due to large magnitude of the velocity fluctuations and the size of the vortices.

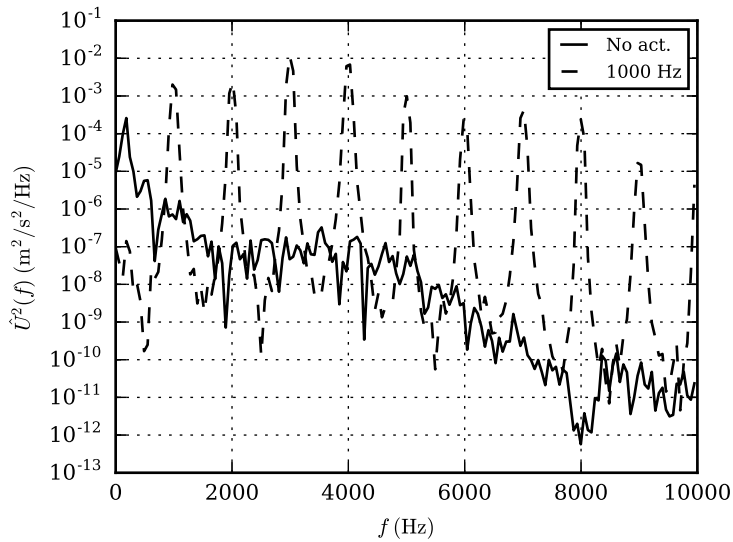


Figure 6.14: Spectra of the U component of the velocity at a point 10 mm downstream of the inlet on the midline of the shear layer.

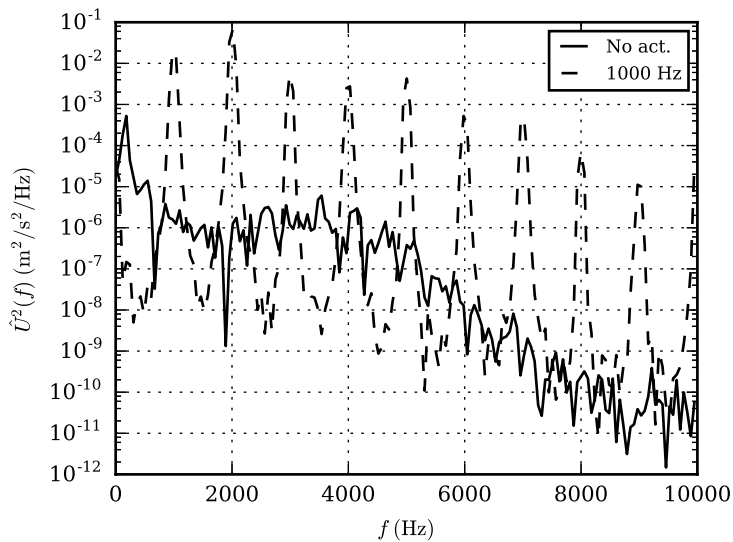


Figure 6.15: Spectra of the U component of the velocity at a point 15 mm downstream of the inlet on the midline of the shear layer.

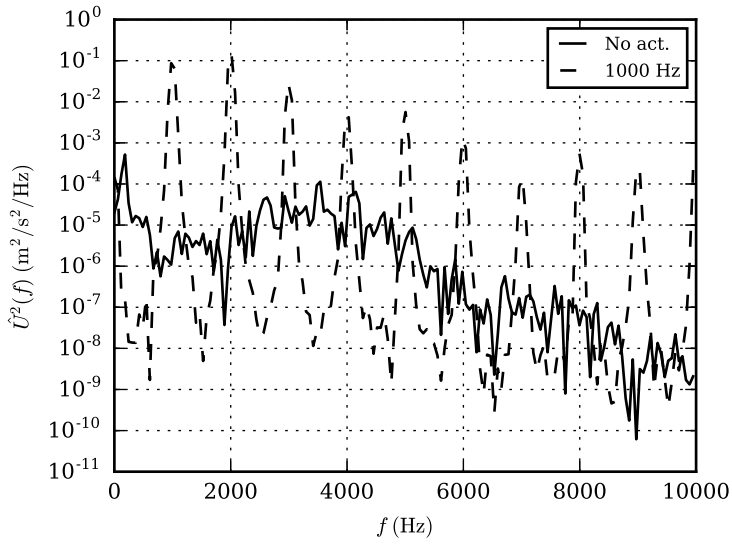


Figure 6.16: Spectra of the U component of the velocity at a point 20 mm downstream of the inlet on the midline of the shear layer.

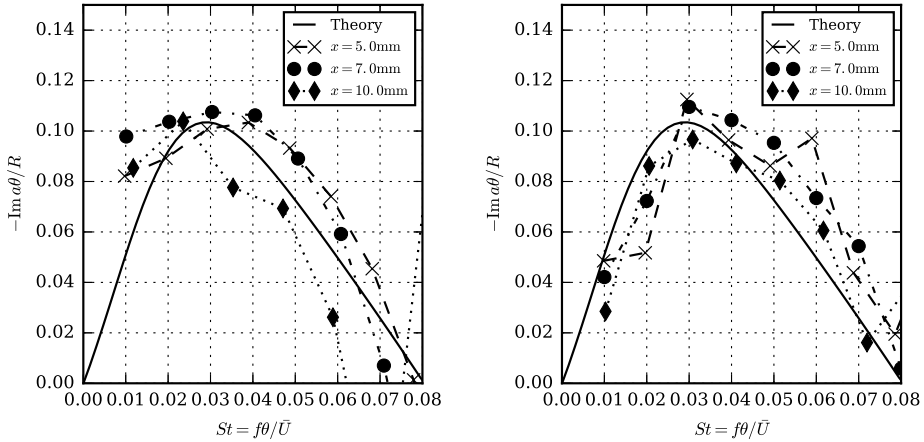


Figure 6.17: Growth rate vs. Strouhal number for several x positions. Actuation at 1000 Hz (left) and no actuation (right).

Effect of varying energy input

In addition to the frequency dependence, the dependence of the results on the energy input per pulse was studied. To do so, simulations with fixed repetition frequency of 1000 Hz and varying energy input per pulse have been carried out. The momentum thickness and Reynolds stress, may be considered most relevant characteristics of actuation effectiveness for separation control applications. These plotted along the midline of the shear layer for several different values of energy per pulse in figures 6.18 and 6.19. In all cases the fixed repetition frequency of $F = 1000$ Hz was used. The same characteristics for one fixed location at $x = 10$ mm are shown in figures 6.20 and 6.21 as functions of average discharge power $P = F \cdot E$. These are compared with results obtained with fixed energy and varying repetition frequency. It can be seen that dependence of the results on energy per pulse is monotonic and smooth, whereas dependence on frequency exhibits a maximum, after which effectiveness decreases. An interesting result is the almost exact equality of actuator effectiveness at low average power levels, regardless if they reached by means of decreasing energy per pulse or repetition frequency.

The presented results can provide guidance for choosing optimal parameters for actuation with respect to energy efficiency. This is particularly important for practical applications, where discharge energy is normally limited by the electric parameters of the equipment used, and thus can not be increased arbitrary. The current results imply that, there exists an optimal discharge frequency for which the momentum thickness and Reynolds stress is maximized for a given maximum energy per pulse. It should be noted, however, that choosing measures of control effect other than momentum thickness and Reynolds stress might result in different optimal parameters.

Mesh convergence

In order to assure that the mesh refinement is enough for the simulations, results with the different levels of mesh resolution described in section 6.3 have been compared. A typical result is presented in figure 6.22, where the momentum thickness θ is plotted versus the flow wise coordinate, x . At the levels of refinement used, there is little sensitivity of the results to mesh size.

Conclusions

A numerical investigation of the excitation of a free shear layer with NS-DBD actuators has been carried out. The qualitative results are similar to those obtained in the experimental visualizations of [13]. Coherent vortex structures similar to

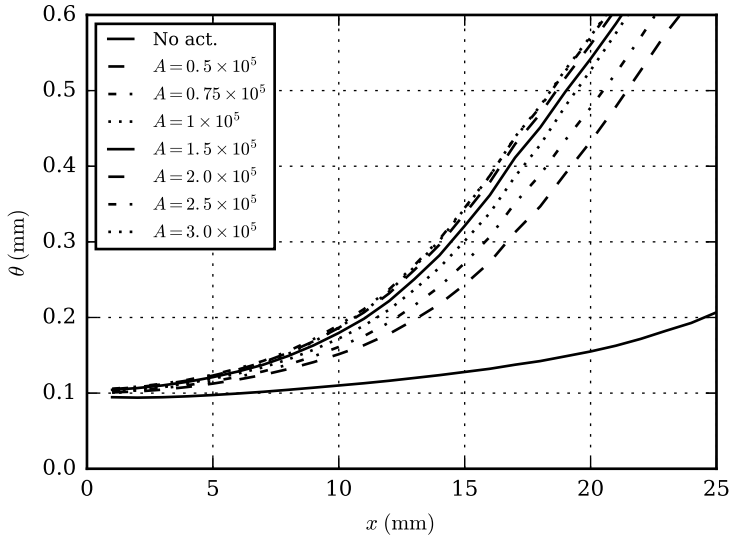


Figure 6.18: Momentum thickness growth for cases without actuation and with actuation at fixed frequency with varying energy per pulse.

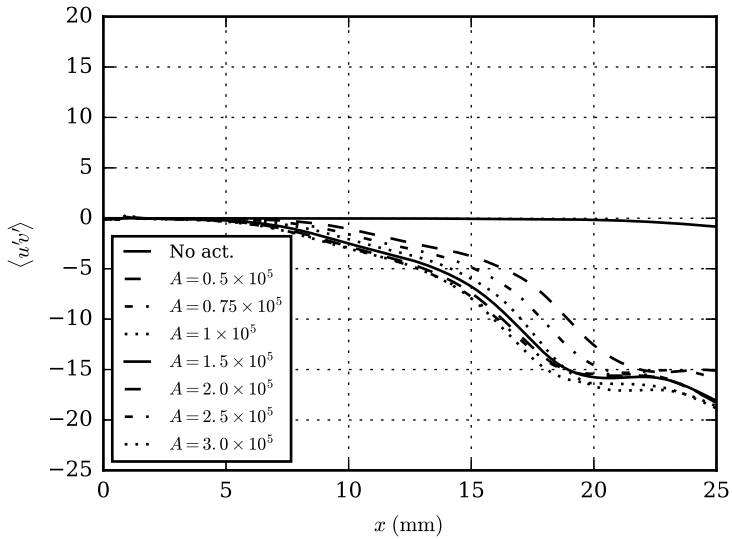


Figure 6.19: Reynolds stress growth for cases without actuation and with actuation at fixed frequency with varying energy per pulse.

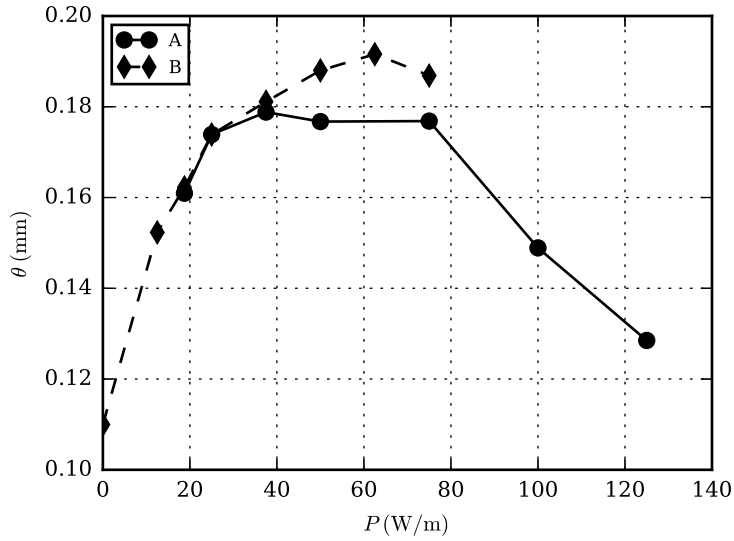


Figure 6.20: Momentum thickness θ at position $x = 10$ mm vs. discharge power P . A — at constant energy per pulse and varying frequency, B — at constant frequency 1000 Hz and varying energy per pulse.

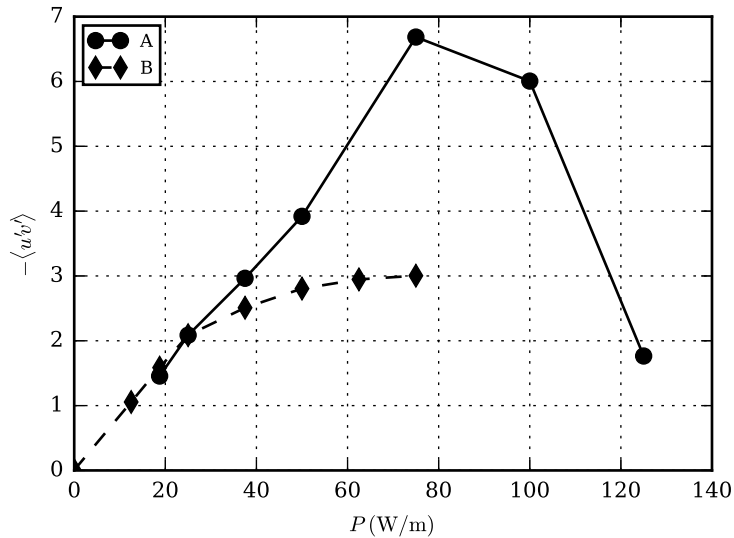


Figure 6.21: Reynolds stress $\langle u'v' \rangle$ at position $x = 10$ mm vs. discharge power P . The line (A) indicates a constant energy per pulse and varying frequency, while (B) indicates a constant frequency 1000 Hz and varying energy per pulse.

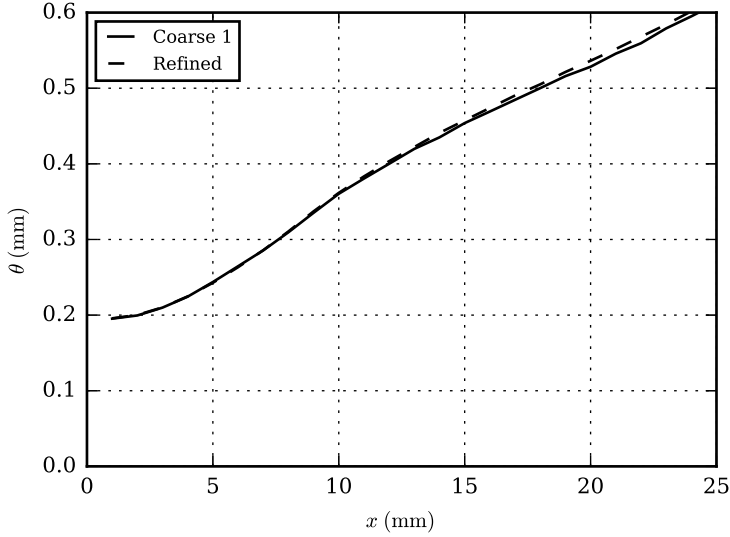


Figure 6.22: Reynold stress $\langle u'v' \rangle$ at position $x = 10$ mm vs. discharge power P . The line (A) indicates a constant energy per pulse and varying frequency, while (B) indicates a constant frequency 1000 Hz and varying energy per pulse.

those found in the experiments have been observed as well as large increases in momentum thickness and Reynolds stress of the shear layer due to actuation. The influence of actuation frequency and amplitude quantified. The growth rates of the disturbances are found to be in agreement with the predictions of the linear stability theory within the uncertainties of the numerical method.

Chapter 7

Conclusions and outlook

Conclusions

This thesis has addressed the physics, modeling and behavior of NS-DBD actuators for separation control. Firstly, it was examined how the NS-DBD actuator could be modeled efficiently for the prediction of its effects on separation control. First principles models are clearly inappropriate for this purpose, due to the vast differences in the time scales of plasma (~ 20 ns), thermodynamic (~ 1 μ s) and fluid dynamic (~ 1 ms) processes. This separation of scales, however, can be exploited by modeling only the fluid dynamical effects which have been identified in literature. Here thermodynamical effects are modeled with a spanwise-uniform volumetric source term in the energy equation of the compressible Navier-Stokes equations. As momentum deposition is known to be low, it is not modeled. For the specific actuator considered, the region of energy deposition was assumed to have a cross-section of 0.5 mm by 0.5 mm based on experimental observations, and to be uniform in time during 1 μ s after the discharge. The amount of energy released was estimated from electrical measurements. This model was embedded into a 2D compressible laminar Navier-Stokes simulation.

To find out if the model could be used to explain the experimentally-observed effects of NS-DBD actuators on separation, it was used to perform simulations in two different flows considered relevant for separation control. The first of these flows was a laminar boundary layer. This case is relevant for a situation where an actuator is used to promote early transition making the boundary layer more resistant to separation. The model was found to qualitatively reproduce the effects of actuation in a laminar boundary layer. The shapes, wavelengths and speeds

of the computed disturbances were found to be close to those in the experiment. The second flow considered was the free shear layer. This case is relevant for a situation where an actuator is used to eliminate laminar leading edge separation. Here, actuation led to an early formation of vortices in the shear layer, similar to that observed in laminar leading edge separation experiments. The actuation was found to cause an increase in the momentum thickness and Reynolds stress in the shear layer. Thus in both cases considered, the proposed model was able to qualitatively reproduce the effects of the NS-DBD actuation. The results of the simulations can be considered to be a qualitative validation of the model.

To study the processes relevant for the effects of NS-DBD actuators, the nature and dynamics of disturbances introduced into the flow were investigated. In both flows, actuation produced convective instabilities. For the laminar boundary case, the disturbance was analyzed using a POD approach. The most energetic POD mode of the disturbance was found to be similar to the most unstable Tollmien-Schlichting wave, as predicted by linear stability theory. For the free shear layer case, the growth rates of the disturbances were compared to the predictions of linear stability theory and found to agree within the bounds of the identification procedure. The role of compression waves observed in experiments has also been investigated, but found not to be essential in determining the effect. In summary, the results of the simulations have shown that the primary mechanism of NS-DBD actuation in the flows considered is an excitation of natural instabilities in the flow, which then evolve according to stability properties of the flow.

To find optimal conditions and parameters for NS-DBD actuators, a parametric study has been carried out for the two flows in question. The variation of energy input due to changing actuation frequency and energy per pulse was investigated. For the boundary layer case, the parametric study demonstrated the existence of an initially linear range followed by a saturation with increasing energy per pulse. For both flows, the existence of optimal values of the frequency and energy per pulse was shown. The optimal frequencies were in correspondence with the most unstable frequencies predicted by the linear stability theory. The two cases considered, however, do not answer other questions relevant for practical application of NS-DBD actuators, such as the optimal positioning of an actuator on a wing surface. For this, the extension of the proposed modeling method to complex geometries and turbulent flows is required. This defines a direction for further research on the topic of NS-DBD actuators.

Outlook

The results of current work open the path to simulations for different applications of NS-DBD actuation. Such simulations can help to determine flow conditions

where an actuator is most effective, and to select an optimal position, voltage and frequency of actuation. At a higher level application level, the development of a control strategy using NS-DBD actuators could also make use of the proposed model, leading to estimations of the possible benefits of NS-DBD actuators for practical applications.

Applications which involve complex geometries or turbulent flows, however, violate some of the assumptions used for the current model. The separation of scales can be violated if the turbulence scales approach the scales of the discharge, which is the case for high-Re flows. This would require a full first principles simulations of the plasma actuation together with DNS simulation of the flow dynamics. The separation of scales assumption can be restored if only the largest turbulent scales are resolved, as in LES. Existing SGS and RANS turbulence models, however, were developed without having NS-DBD actuators in mind, and have no way to respond to disturbances caused by actuation. Additionally, fidelity of existing RANS turbulence models for separated flows is generally be not high enough to produce accurate predictions of separation. A middle ground may exist for problems where it may be assumed that the interaction of the actuation with turbulence is not significant and that the dominant effect of the is the creation of vortical structures with scales much larger than the turbulent scales. An example analysis based on such assumptions is described in [Appendix A](#), in which some qualitative agreement with experiment was found.

In general, however, reliable LES or RANS simulations of NS-DBD plasma actuators would require additional research to develop turbulence models specifically adapted for usage with the NS-DBD actuator model. As an alternative, a hybrid approach could be employed, where a DNS simulation is used in the vicinity of the actuator location, and RANS is used elsewhere. Further research is required to make such simulations accurate and reliable enough for practical application.

This thesis focused on application of NS-DBD actuators for separation control. There are, however, experimental observations suggestion a number of other applications, such as load control for wind turbines, noise suppression, deicing and others. These applications also require numerical simulations, and it seems likely that the proposed actuator model can be used for such cases as well.

Appendix **A**

Preliminary simulations of NS-DBD plasma actuators on airfoils

Introduction

In the present thesis, the framework for modeling NS-DBD plasma actuators is established and applied to several model situations, such as a laminar boundary layer and a free shear layer. All these cases are two-dimensional and at low Reynolds numbers. For practical engineering purposes, however, simulations on more complex geometries are required. This poses several challenges. First, real geometries are usually three-dimensional. Moreover, even if the geometry itself is two-dimensional, the flow field is often inherently three-dimensional, such the flow in separated regions on a wing. Second, in many practical applications, the Reynolds number is relatively large, and thus the flow is turbulent. Additional considerations have to be made to simulate the effects of NS-DBD plasma actuators in such conditions.

The experiments and simulations described in this thesis show that the effect of the actuator in the case of leading edge separation is largely due to the creation of large scale vortices, which propagate through the shear layer formed on the boundary of separation zone. These vortices are coherent in the spanwise direction and propagate first in a laminar flow and then in turbulent one, but are expected to have large size compared to the typical size of turbulent fluctuations at higher Reynolds numbers.

This separation of spatial scales between coherent vortices and the turbulence allows us to make a hypothesis that the interaction of these two can be represented

to first approximation by the turbulent viscosity coefficient computed with the standard turbulence model. This assumes that the coherent vortices do not affect the turbulence model. Under this assumption we consider a preliminary RANS simulation for the actuator in the separated region on an airfoil. The simulation was performed using a compressible pressure-based Navier-Stokes solver from the open source CFD package OpenFOAM. The large scale vortices are resolved and the fine scale turbulence is modeled by a turbulence model (in this particular case we use Menter's $k - \omega$ SST model) in the standard way. The airfoil (NACA 63₃-618) and flow conditions were selected to be the same as in the experiments performed in [13].

In a separated region, the flow is essentially three-dimensional, and the vortices are expected to break down in three-dimensional way. This cannot be accounted by a RANS simulation, and thus there is a considerable model error in these conditions. Although it is not expected that this simulation is fully accurate, it does exhibit qualitative similarities to the experiment.

Setup and meshing

The numerical domain for the simulation consisted of an O-type hyperbolic mesh with an almost circular outer boundary with a radius of 20 chord lengths. The mesh and the airfoil were held fixed, and to simulate different angles of attack, the direction of the inflow was changed.

The airfoil profile used was a NACA 63₃-618 airfoil, taken from University of Illinois Urbana-Campaign Airfoil Database¹ and then interpolated using cubic splines to have 1000 points along the surface to make leading edge bump-free, which is crucial for separation simulations. The airfoil section is shown in [Figure A.1](#). General parameters of the simulation are shown in [Table A.1](#).

The mesh has 1000 cells along the surface of the airfoil and 118 cells in wall-normal direction, giving 118000 cells in total. The size of the first cell is $2 \cdot 10^{-5} \text{ m} = 20 \mu\text{m}$, corresponding to $\langle y^+ \rangle \approx 0.9$, $y_{\text{max}}^+ \approx 2.0$. The mesh is shown in [Figure A.2](#). The mesh was designed to provide high near-wall resolution and high enough tangential resolution in the actuator region (to resolve the region of fast gas heating by the actuator).

Boundary conditions

On the outer boundary, the switching boundary condition was used for the velocity field (`inletOutlet` in OpenFOAM). This enforces fixed value boundary con-

¹Available on the Internet at http://aerospace.illinois.edu/m-selig/ads/coord_database.html

Parameter	Symbol	Value	Unit
Freestream velocity	U_∞	50	m/s
Chord length	c	755	mm
Reynolds number	$Re = U_\infty c / \nu$	2.5×10^6	—
Mach number	M	0.15	—
First cell height	y_1^+	0.9	wall units

Table A.1: Simulation parameters

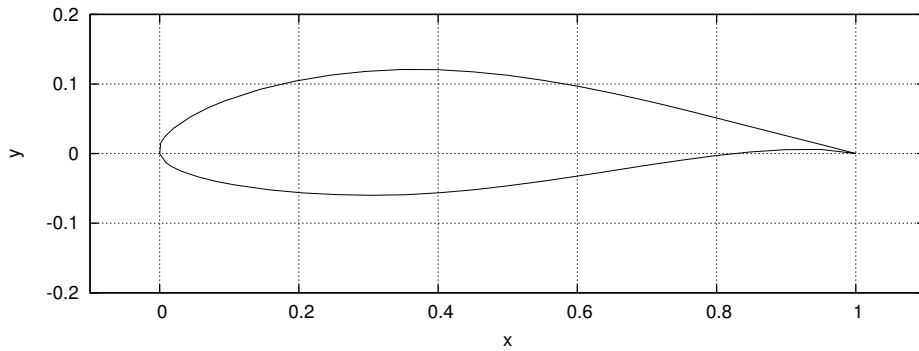
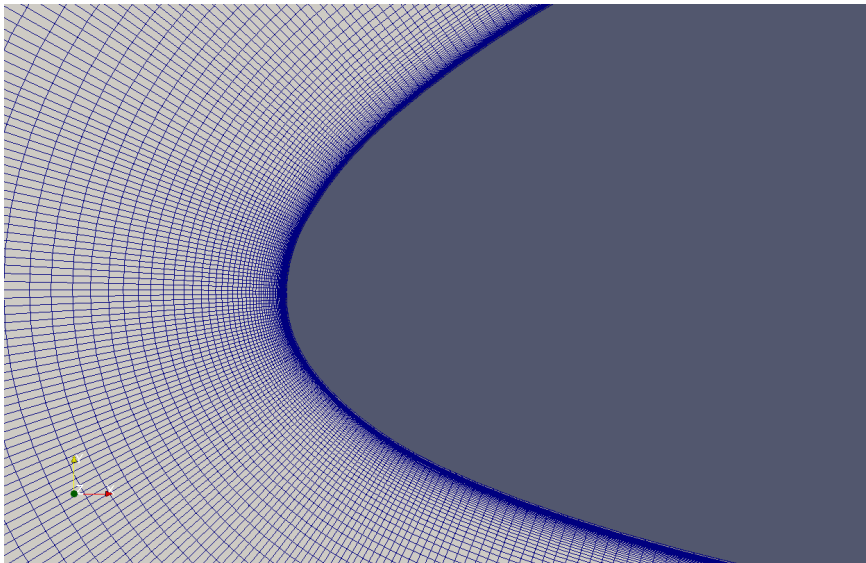
Figure A.1: NACA 63₃-618 airfoil.

Figure A.2: Mesh in the leading edge region.

dition where velocity is directed inwards, and zero gradient boundary condition where velocity is directed outwards. For the pressure field, a waveTransmissive boundary condition was used. This boundary condition implements a simplified method of characteristics for non-reflective boundary condition for compressible flows.

On the airfoil surface, standard boundary conditions for the solid wall were used: a no-slip boundary condition for the flow velocity field and a zero gradient boundary condition for the pressure field. For the temperature field, a switching inletOutlet boundary condition was used on the outer boundary, while a fixed value was used on the surface of the airfoil (an isothermal boundary condition). In both cases, reference value was set to 300 K.

Turbulence model

A *Menter $k - \omega$ SST turbulence model* was used. This model was chosen because it has been thoroughly validated and is known to predict separation relatively well compared to other turbulence models. The model requires two additional fields: turbulent kinetic energy k and relative rate of dissipation ω . It also solves two additional evolution equations for these fields. Based on these, the turbulent viscosity coefficient μ_t is computed, and used in Reynolds-averaged Navier-Stokes equations. On the outer boundary of the domain, the inletOutlet boundary condition was used, with inlet values set to be low, corresponding to a non-turbulent free-flight conditions. On the surface of the airfoil special wall functions provided with OpenFOAM are used, claimed to be suitable for low-Re conditions. (From turbulence modeling perspective, conditions are considered low-Re where the the first cell next to the wall has $y^+ \leq 1$, and conditions considered high-Re where the first cell has $y^+ > 30$). In the present simulation, the first-cell non-dimensional wall distance was $y^+ \approx 1$.

Results

First, simulations without an actuator were performed. Because the simulations can be non-converging in some conditions (due to vortex shedding at very high angles of attack, for example), an unsteady time scheme was chosen. The simulations were run for long times, enough to pass the transient period before taking statistics. Then the averaging of data was performed on the time series of aerodynamic coefficients. The results are presented for the critical angle of attack of the unactuated case (16 degrees), which is the lowest angle of attack where the effect of actuation is detected.

Simulations with the actuation were performed with the same setup as the

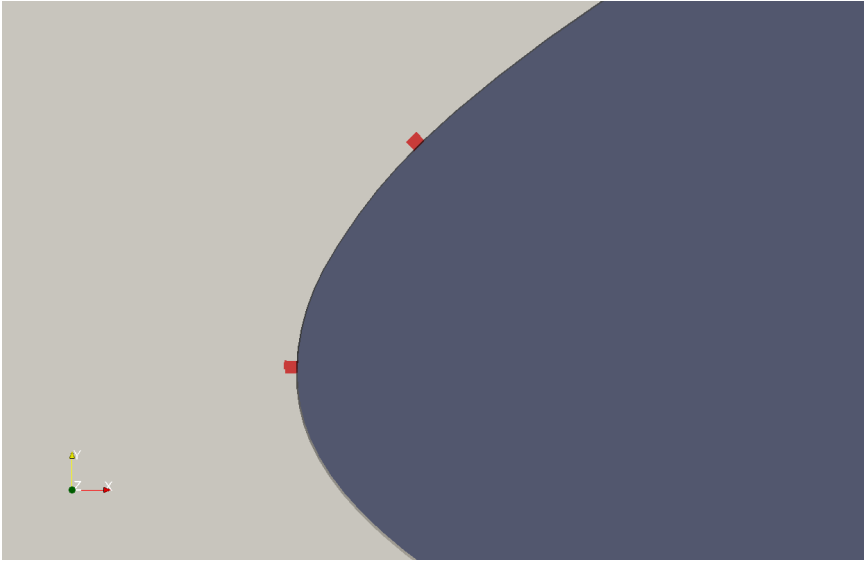


Figure A.3: Positioning of the actuators on the surface of the airfoil.

simulations without the actuation, except the addition of the actuator model. Two actuator models were placed in the simulation domain on the surface of the airfoil. One is placed close to the leading edge of the airfoil ($y = +4.0$ mm), and the second one is placed about 30 mm downstream on the suction side of the airfoil ($x = +9.5$ mm, $y = +22.8$ mm). The position of the actuator models is shown in [Figure A.3](#). Actuators were operated at the frequency 200 Hz (corresponding to the burst repetition frequency used in the experiments), with an energy of actuation 10 times larger than an estimated energy of a single pulse, simulating a 10-pulse burst mode. The comparison of the lift curve with and without the actuation is shown in [Figure A.4](#). Looking at the flow field examples (shown in [Figure A.5](#) for the angle of attack of 16 degrees), we can see the series of coherent large scale vortices produced by the actuation, propagating along the surface of the airfoil, which qualitatively corresponds to the experimental observations.

Analysis and conclusions

In this section the initial attempt on the simulation of the actuator in the separated flow on the airfoil is demonstrated, which is a proof of concept for further research in this direction. The simulation, although based on loose assumption, exhibit the behavior similar to that observed in the experiments. The actuation produces a train of large scale vortices, which transfer momentum from the free flow into

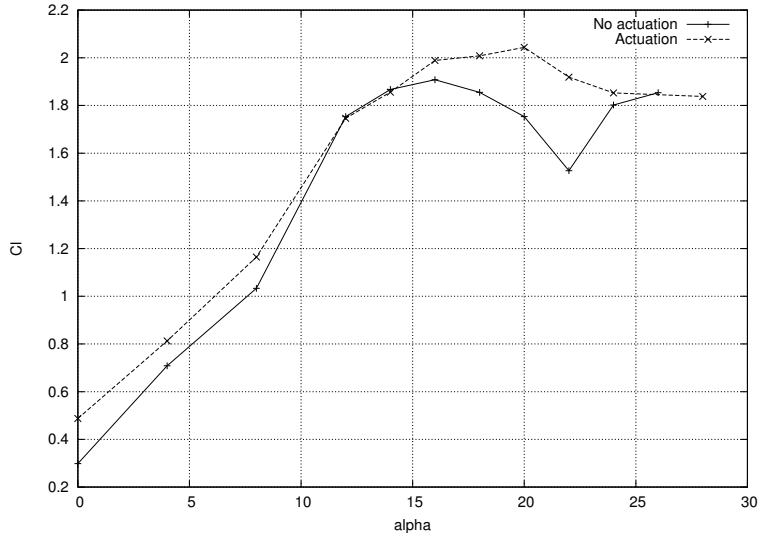


Figure A.4: Comparison of the lift coefficient with and without actuation. (Note: the results at the angles of attack greater than 16 degrees, where the separation takes place, are unreliable as the three-dimensional nature of separation not taken into account in a 2D RANS simulation.)

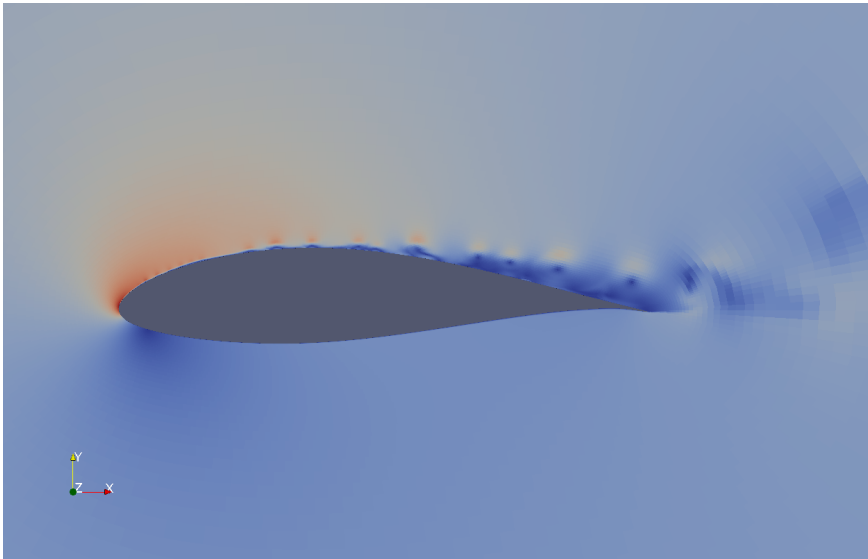


Figure A.5: Example of the velocity field for the angle of attack of 16 degrees, showing the series of vortices generated by the actuation.

the separated region. This leads to massive reduction in the size of separation region and increase in lift coefficient in stall conditions. This simulation proves that there is a possibility of the computationally cheap simulations of separated flows with actuation, but requiring additional research.

Three directions to improve quality of the simulations of the NS-DBD actuators compared to the present naive one are foreseen:

- Resolve more. This would employ a three-dimensional compressible LES simulation, capable of resolving interaction between the instabilities introduced by the actuator and the turbulence present in the flow. A hybrid approach where the relatively small region in the vicinity of the actuator and in the separation region is simulated using 3D compressible LES and the rest of the domain is simulated using uRANS shall be considered.
- Resolve less. For that, the construction of the completely new turbulent model is required, which would incorporate the whole effects of the actuator, including compressibility effects, flow instabilities and vortex structures introduced. The simulation is therefore no more required to resolve these structures.
- Follow the present approach. We resolve the actuator and large scale vortices, leaving the turbulence for the turbulence model, but we modify the turbulent model to make sure it interacts correctly with the large-scale structures.

The choice of the of the option is determined by the trade-off of computational cost and accuracy of the model. The first option is the most straightforward, requiring the least additional assumptions and research work, at the cost of highest numerical complexity. The second option promises to greatly reduce the computational time required for the simulation, although requiring the most research efforts to propose and validate such a turbulent model. The third one represents middle ground in terms of computational cost and accuracy.

Appendix **B**

Proper orthogonal decomposition

Proper orthogonal decomposition (POD) is a powerful tool for analysis of flow fields. POD has been widely used in this thesis. For this purpose special software tools have been developed. This chapter gives an introduction to POD, describes the algorithm and its software implementation within the OpenFOAM framework. Some brief introduction to reduced order modeling using POD is given as well. Finally, several example cases are presented to demonstrate the method and implementation.

Algorithm description

Introduction

Proper Orthogonal decomposition (POD) is a powerful technique for analyzing flow fields. It allows to identify and separate the most energetic modes, which are of great interest for many fluid dynamical problems.

The variation of the method described here is based on snapshots of the velocity field, obtained either from LES or DNS simulation or from experiments, for example by the means of particle imaging velocimetry (PIV). We then try to construct a basis and represent the velocity field snapshots as a linear combination of the basis functions. The basis functions are ordered by their energy contribution to the flow field. Thus, first basis functions represent the most energetic modes of fluid motion.

In mathematical sense, POD is construction of a basis ϕ_i , $i = 1 \dots N$ that minimizes error in kinetic energy (or, equivalent, L_2 error in velocity vector) for the reconstruction of snapshots:

$$\Phi = \{\phi_i\}, \quad i = 1 \dots N, \quad (\phi_i, \phi_j) = \delta_{ij} \quad (\text{B.1})$$

$$\Phi = \operatorname{argmin} \int_{\Omega} (u - \hat{u})^2 \, d\Omega \quad (\text{B.2})$$

$$\hat{u} = \mathbf{P}_{\Phi} u = \sum_i a_i \phi_i = \sum_i \frac{(u, \phi_i)}{(\phi_i, \phi_i)} \phi_i \quad (\text{B.3})$$

where δ_{ij} is a Kronecker delta symbol, Ω is a domain, and \mathbf{P}_{Φ} is a projection operator onto the basis Φ .

Construction of POD basis

Consider we have snapshots of flow fields: $U^i, p^i, i = 1..N_s$, representing the flow field at different time instants (time based decomposition) or different realizations of the process (ensemble based decomposition), where N_s is the number of snapshots used, and N is the number of cells in the mesh.

First we calculate mean flow and subtract it from snapshots:

$$\bar{U} = \frac{1}{N_s} \sum_i U^i$$

$$\bar{p} = \frac{1}{N_s} \sum_i p^i$$

then we construct correlation matrix for velocity field:

$$C_{ij} = (U^i, U^j) \quad (\text{B.4})$$

using inner product of the form:

$$(f, g) = \int_{\Omega} f g \, d\Omega \quad (\text{B.5})$$

Then, we solve *eigenvalue problem* for correlation matrix C to find eigenvalues λ_i and eigenvectors v_i .

$$C v_i = \lambda_i v_i \quad (\text{B.6})$$

Since matrix C is symmetric, all eigenvalues are real, and eigenvectors form an orthogonal set.

Instead of solving an eigenvalue problem on correlation matrix, a *singular value decomposition* (SVD) can be used for initial dataset (without construction of correlation matrix):

$$U = V \Sigma W^* \quad (\text{B.7})$$

where singular values σ_i of snapshot matrix U are related to eigenvalues λ_i of correlation matrix C :

$$\sigma_i = \sqrt{\lambda_i} \quad (\text{B.8})$$

According to matrix analysis theory, this can offer better performance and better numerical stability, but unfortunately, SVD is not implemented within OpenFOAM, thus requiring usage of an external library for SVD.

As a quality criterion for the basis, we use total fraction of the flow energy represented by the first m modes, which can be computed using the obtained eigenvalues:

$$\alpha_m = \frac{\sum_0^m \lambda_i}{\sum_0^{N_s} \lambda_i} \quad (\text{B.9})$$

Then we select N_m (which is determined either by desired accuracy or specified explicitly) largest eigenvalues and construct velocity basis functions:

$$\phi_i = \sum_{j \leq N_s} v_{ij} U^j \quad (\text{B.10})$$

and normalize them such that:

$$(\phi_i, \phi_j) = \delta_{ij} \quad (\text{B.11})$$

Given this basis, we can consider velocity field approximated following way:

$$u(x, t) \approx \bar{U}(x) + \sum_{i \leq N_m} a_i(t) \phi_i(x) \quad (\text{B.12})$$

Also we calculate basis functions for pressure using the same eigenvectors:

$$\psi_i = \sum_{j \leq N_s} v_{ij} p^j \quad (\text{B.13})$$

and thus pressure is approximated as

$$p(x, t) \approx \bar{p}(x) + \sum_{i \leq N_m} a_i(t) \psi_i(x) \quad (\text{B.14})$$

Numerical complexity of this procedure is follows: to calculate correlation matrix we need $O(N_s^2 N)$ operations, and we need to keep all the snapshots in memory, $O(N_s N)$ memory words. Then, to calculate eigenvalues and eigenvectors, $O(N_s^3)$ operations are needed. Additionally, $O(N_m N_s N)$ operations are needed to calculate basis functions.

Galerkin projection of the Navier-Stokes equations

Having constructed a POD basis, we can use it to construct a reduced order model of the flow. For this purpose, we can project Navier-Stokes equation onto the POD basis to obtain a system of ordinary differential equations representing evolution of the mode coefficients in time. This can be done using Galerkin projection method. This model can then be used as a computationally cheap replacement of the full Navier-Stokes equations.

Continuity equation is automatically satisfied since every snapshot satisfies it, and our solution is a linear combination of snapshots. If basis functions do not satisfy the continuity equation by themselves, some modification to the model should be made.

As of momentum equation:

$$\frac{\partial u}{\partial t} + (u \cdot \nabla)u = -\nabla p + \frac{1}{Re} \Delta u \quad (\text{B.15})$$

we multiply it by each of our basis functions ϕ_i :

$$(\phi_i, \frac{\partial u}{\partial t} + (u \cdot \nabla)u) = (\phi_i, -\nabla p + \frac{1}{Re} \Delta u) \quad (\text{B.16})$$

then substituting decomposition of velocity field:

$$\sum_j L_{ij} \frac{da_j}{dt} = b_i + \sum_j B_{ij} a_j + \sum_{j,k} C_{ijk} a_j a_k \quad (\text{B.17})$$

where

$$L_{ij} = (\phi_i, \phi_j) = \delta_{ij}$$

$$b_i = (\phi_i, -(\bar{U} \cdot \nabla)\bar{U} + \frac{1}{Re} \Delta \bar{U})$$

$$B_{ij} = (\phi_i, \frac{1}{Re} \Delta \phi_j - \nabla \psi_j - (\bar{U} \cdot \nabla)\phi_j - (\phi_j \cdot \nabla)\bar{U})$$

$$C_{ijk} = -(\phi_i, (\phi_j \cdot \nabla)\phi_k)$$

To calculate these coefficients, $O(N_m^3 N)$ operations are needed.

This system of ordinary differential equations can be integrated by any numerical integration method, for example by Runge-Kutta method. For each RHS calculation, $O(N_m^3)$, operations are needed (plus the same order for inversion of matrix L by direct method if needed).

Flow rate conservation

Since we excluded mean flow from our ODE system, and flow rate is contained in mean flow, no special treatment of flow rate conservation is required.

SGS model

The inclusion of SGS model can be desirable. The model shall account for sub-grid scale vortices and their influence on the flow dynamics.

In current study a Smagorinsky model is used, acting on all the modes. The model defines an eddy viscosity coefficient, ν^{SGS} , which is added to normal viscosity term in Navier-Stokes equation. The implementation of SGS model consists of two parts: the update of eddy viscosity field and application of SGS model in calculation of RHS of ROM.

The update of eddy viscosity is performed not every time step to save computational time, since the operation is expensive. The interval of the update can be adjusted in configuration time. First, the velocity field is reconstructed:

$$u^r(x, t) = \bar{U}(x) + \sum_i a_i(t) \phi_i(x) \quad (\text{B.18})$$

Then, the eddy viscosity is recalculated

$$\nu_{\text{SGS}}(x) = 2(Cs\delta)^2 \|D(u^r)\| \quad (\text{B.19})$$

where δ is a characteristic length of unresolved scales. In this particular implementation, instead of unresolved scales, the last resolved POD mode is used to estimate δ :

$$\delta = \frac{\|\phi_{N_m}\|}{\|\nabla\phi_{N_m}\|}, \quad (\text{B.20})$$

and $D(U)$ is a deformation tensor

$$D(u) = \frac{1}{2} (\nabla u + \nabla u^T) \quad (\text{B.21})$$

And using this viscosity, coefficients associated with unresolved scales are recalculated:

$$\begin{aligned} b_i^{\text{SGS}} &= (\phi_i, \nu_{\text{SGS}} \Delta \bar{U}) \\ B_{ij}^{\text{SGS}} &= (\phi_i, \nu_{\text{SGS}} \Delta \phi_j) \end{aligned}$$

The complexity of this procedure is $O(N_m^2 N)$ and is determined by calculation of coefficients B_{ij}^{SGS} .

In the ODE which describes the evolution of ROM, new terms associated with SGS are added. Thus the ODE reads:

$$\frac{da_i}{dt} = (b_i + b_i^{\text{SGS}}) + \sum_j (B_{ij} + B_{ij}^{\text{SGS}}) a_j + \sum_{j,k} C_{ijk} a_j a_k \quad (\text{B.22})$$

Weighting

As an additional option, a weighting has been implemented. Weighting allows to focus POD decomposition on the specified region of interest. Given the weighting function w , the dot product becomes instead of B.5:

$$(f, g) = \int_{\Omega} w \cdot (fg) \, d\Omega \quad (\text{B.23})$$

Validation

Laminar vortex shedding

This case resembles the case of Bergmann paper [6].

There is a 2D channel of width 8 units and length 32 units. On the midline there is a square obstacle of size 1×1 . On the wall and an obstacle there is no-slip boundary condition. At the inlet there is a fixed velocity boundary condition, $U = 1$. Reynolds number of the case is about 150.

Snapshots are taken from DNS simulation, and are uniformly spanning 2 periods of vortex shedding. There are 213 snapshots. It appears that the best way to select snapshots is the set spanning small integral number of periods (like 1 or 2). Using more periods does not add any new information. Using not integral number of periods changes the eigenspectrum and adds asymmetry to the modes. But this observation applies only to cases with exact periodical behavior.

The eigenvalues spectrum for this case is presented in figure B.1, and the first 20 of eigenvalues in bigger scale in figure B.2. These plots show clearly the pairing of eigenvalues, meaning periodicity of the process.

ROM simulation based on these POD modes good, giving the realistic results using as less as 6 modes. No SGS model was used since the case is laminar in nature. The results correspond well with results of Bergmann paper [6].

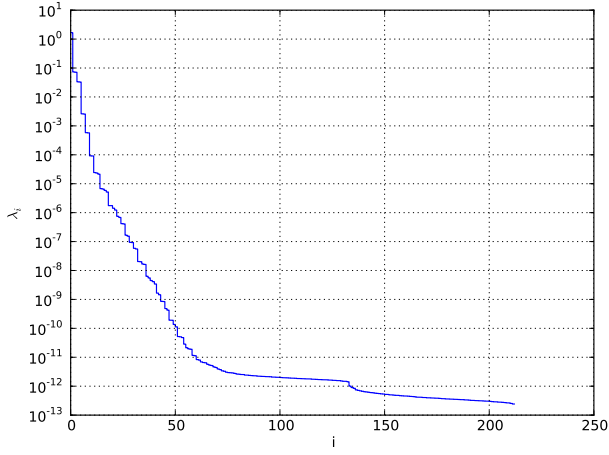


Figure B.1: Eigenvalues for laminar vortex shedding case.

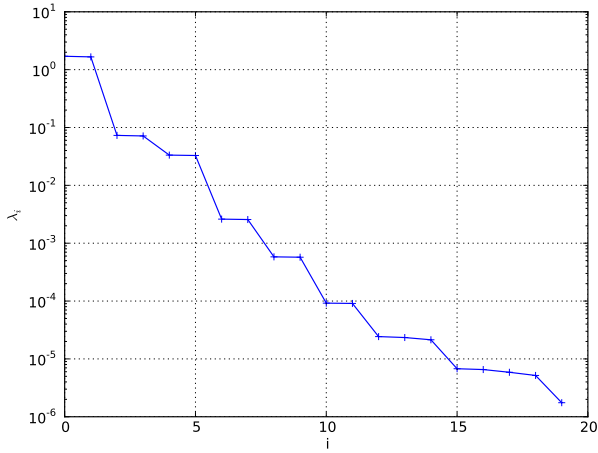


Figure B.2: First 20 eigenvalues for laminar vortex shedding case.

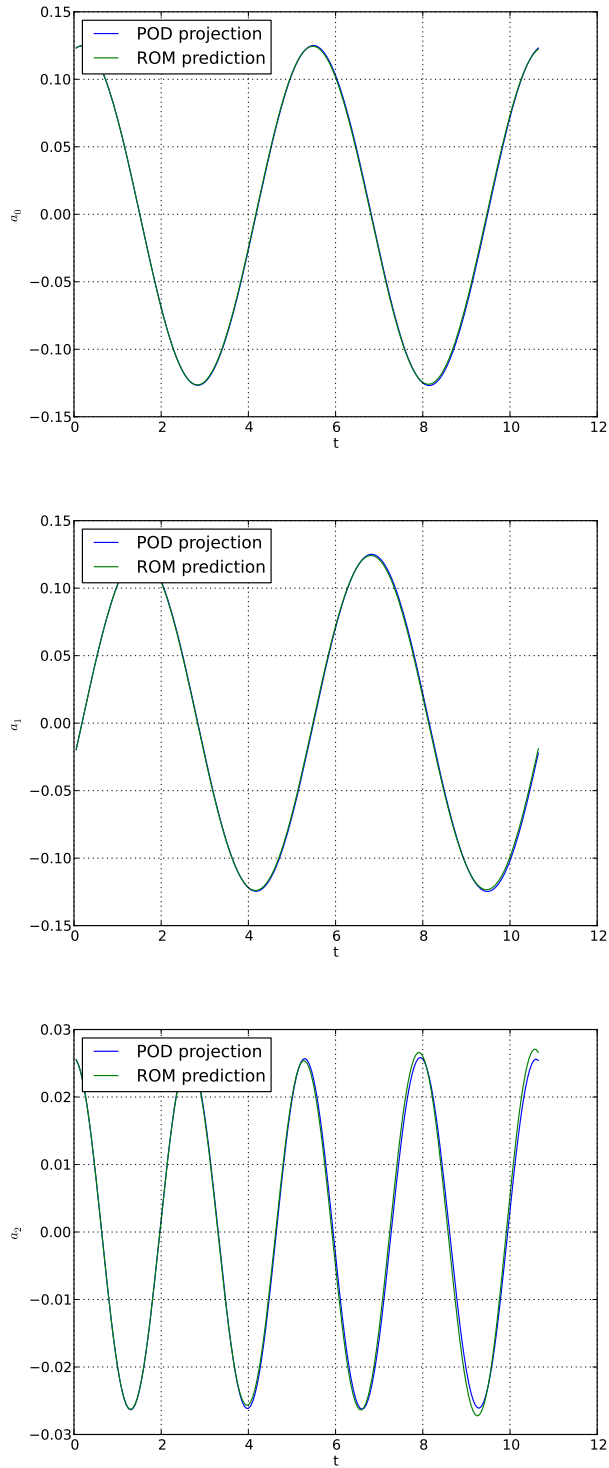


Figure B.3: Amplitude of the 1st mode for DNS and ROM using 6 modes. Laminar vortex shedding case.

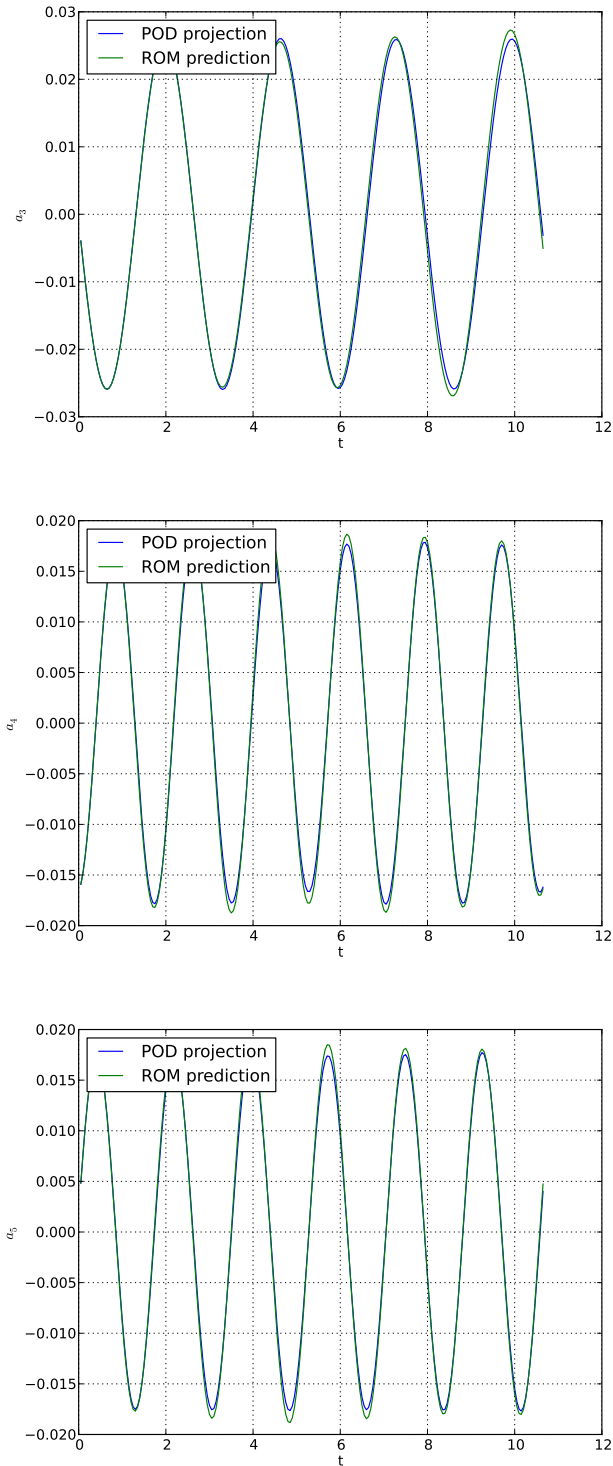


Figure B.4: Amplitude of the 1st mode for DNS and ROM using 6 modes. Laminar vortex shedding case.

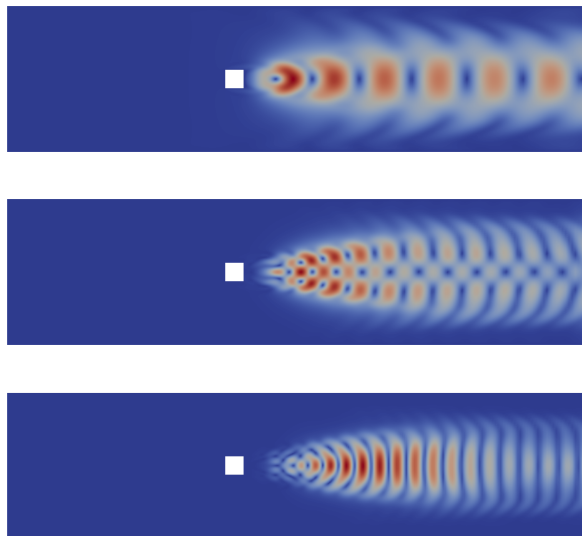


Figure B.5: Velocity magnitude of the 1st, 3rd and 5th modes. Laminar vortex shedding case.

Free shear layer

Free shear layer case is a 2D case with developing instability in the shear layer. It starts from the laminar condition at the inlet, than experiences instabilities, formation and pairing of vortices.

200 snapshots spanning about 1 period of large scale vortex formation were used. The problem in selecting the set of snapshots is that the DNS solution is not exactly periodical and it is not clear if this a problem of quality of DNS or it is true physical property of the problem.

Results presented were obtained using 20 modes without SGS model. There are clear discrepancies between ROM prediction results and POD projection of DNS results, but the source of them is not clearly understood.

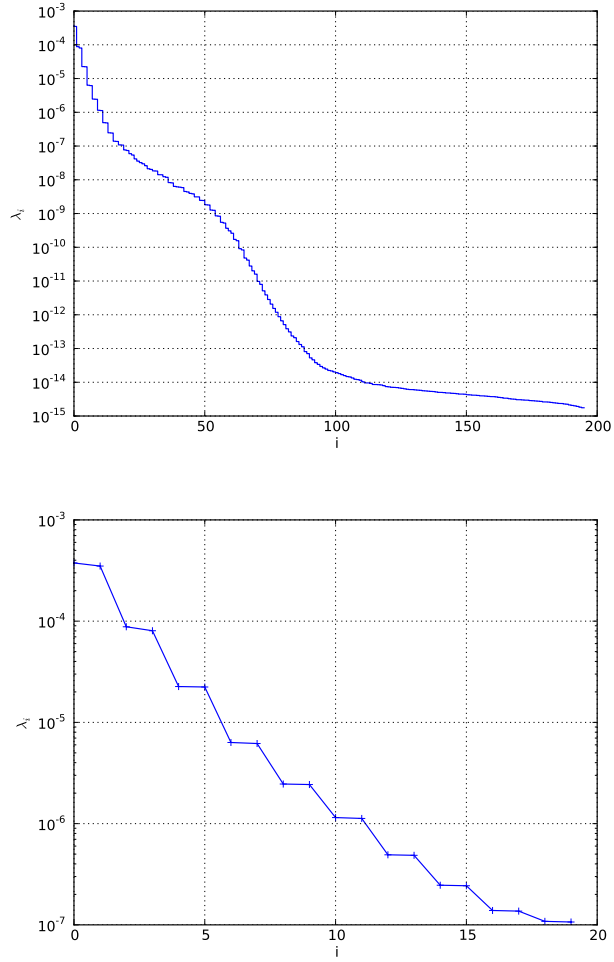


Figure B.6: Eigenvalues for free shear layer case.

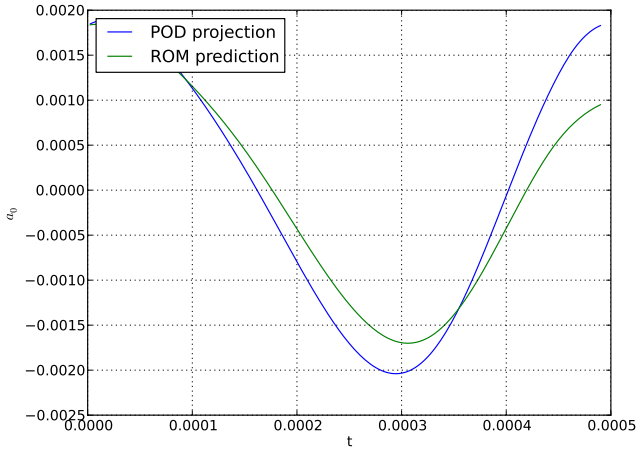


Figure B.7: Amplitude of the 1st mode for DNS and ROM using 30 modes.

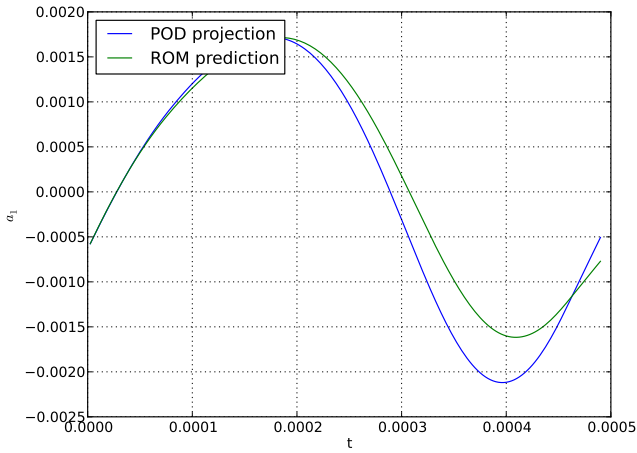


Figure B.8: Amplitude of the 2nd mode for DNS and ROM using 20 modes. Free shear layer case.

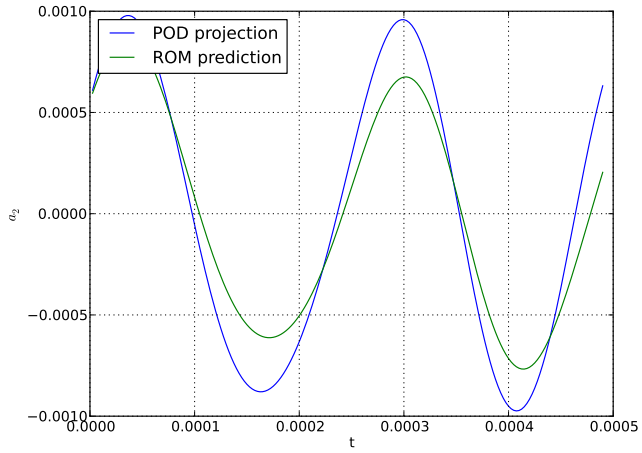


Figure B.9: Amplitude of the 3rd mode for DNS and ROM using 20 modes. Free shear layer case.

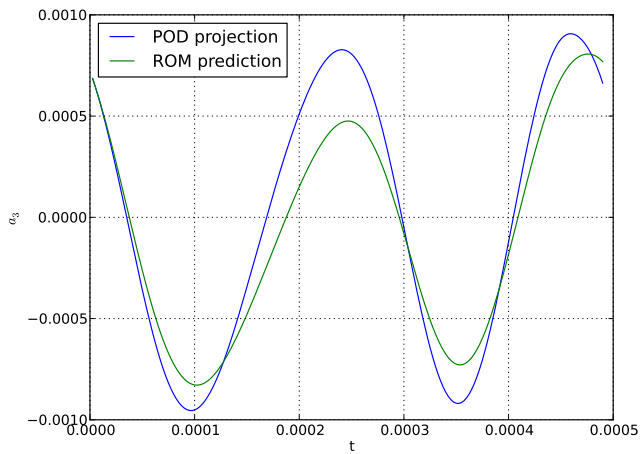


Figure B.10: Amplitude of the 4th mode for DNS and ROM using 20 modes. Free shear layer case.

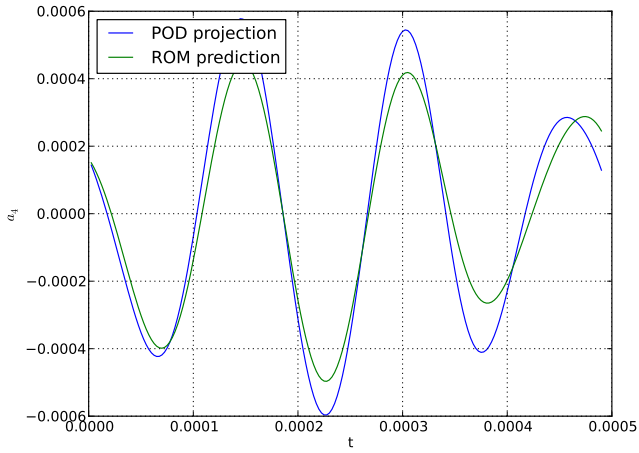


Figure B.11: Amplitude of the 5th mode for DNS and ROM using 20 modes. Free shear layer case.

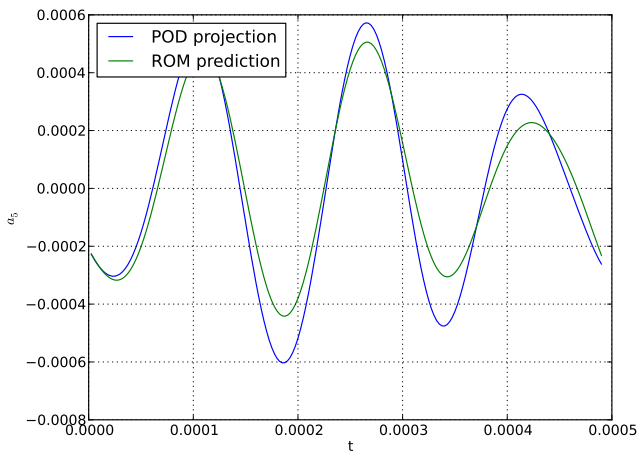


Figure B.12: Amplitude of the 6th mode for DNS and ROM using 20 modes. Free shear layer case.

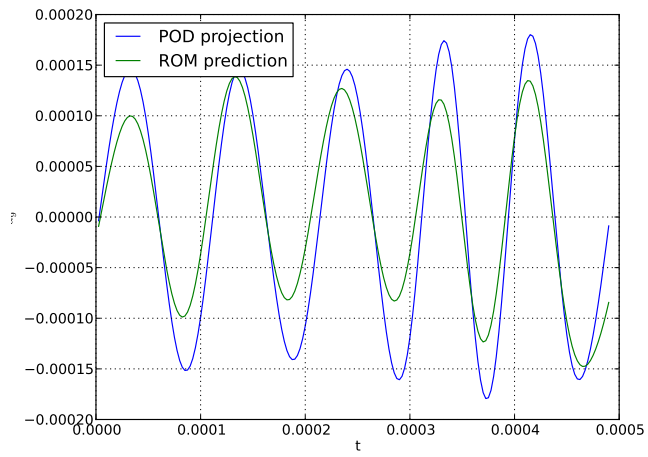


Figure B.13: Amplitude of the 10th mode for DNS and ROM using 20 modes. Free shear layer case.

Appendix C

Linear stability theory

Introduction

Orr-Sommerfeld equation is an main mean of studying linear stability of parallel two-dimensional flows.

Consider two-dimensional parallel incompressible base flow $(U, V) = (U(y), 0)$.

$$u(x, y, t) = U(y) + u'(x, y, t) \quad (\text{C.1})$$

Substituting it into Navier-Stokes equations, linearizing about mean base flow, and assuming the stream function of the fluctuation to be in form:

$$\psi(x, y, t) = \phi(y)e^{-i\alpha(x-ct)} = \phi(y)e^{i(\omega t - \alpha x)} \quad (\text{C.2})$$

where α — wave number, c — wave speed, ω — angular frequency, and

$$\begin{aligned} u &= \frac{\partial \psi}{\partial y} = \phi' e^{i(\omega t - \alpha x)} \\ v &= -\frac{\partial \psi}{\partial x} = -\alpha \phi e^{i(\omega t - \alpha x)} \end{aligned} \quad (\text{C.3})$$

we end up with Orr-Sommerfeld equation (in non-dimensionalized form):

$$\frac{1}{iRe\alpha} \left(\frac{d^2}{dy^2} - \alpha^2 \right)^2 \phi = (U - c) \left(\frac{d^2}{dy^2} - \alpha^2 \right) \phi - U'' \phi \quad (\text{C.4})$$

where Re is a Reynolds number. Set of pairs (α, c) where this equation has non-trivial (non-zero) solutions, define all possible wave-like fluctuations to the flow.

Boundary conditions are

$$\begin{aligned} \phi|_{boundary} &= 0 \\ \frac{d\phi}{dy}|_{boundary} &= 0 \end{aligned} \quad (C.5)$$

where boundary can be either solid wall or freestream at infinity. We can solve it two ways: either select real value for α and solve eigenvalue problem to find (complex) wave speeds c (*temporal stability problem*), or select real wave speed c and solve eigenvalue problem for (complex) α (*spatial stability problem*). In following sections will approach both of these problems.

Temporal stability

In temporal stability problem we would like to answer how the wave with given wavenumber grows in time. To get this, we look for complex wave speed c as a function of real wave number α .

As a result of solving the eigenvalue problem, we will have complex wave speed

$$c = c_r + ic_i \quad (C.6)$$

where real part c_r is a propagation speed along x axis, and c_i is a temporal growth rate. Substituting into stream function expression:

$$\psi(x, y, t) = \phi(y) \cdot e^{\alpha c_i t} \cdot e^{-i\alpha(x - c_r t)} \quad (C.7)$$

where the term $e^{\alpha c_i t}$ is responsible for temporal growth of the wave.

There are several possible approaches to solve Orr-Sommerfeld problem. There are variational approach, Galerkin approach, finite differences approach, and ODE approach. First two require careful selection of basis functions, which requires special research, and the same set of basis functions might not suit all the cases. In the current work, the finite differences approach is used, as the simple and straightforward. On the other hand, variational or Galerkin approaches with carefully selected base functions might require smaller size of matrix and thus less computational time, and possibly give better accuracy.

First the mesh y_i , $i = 1 \dots n$ is constructed, which depends on particular case. In general higher mesh resolution is used near the wall for boundary layer case and in the area of higher velocity gradients in the case of a jet or shear layer. Then, a matrix of Laplacian operator \mathbf{L} is constructed, which calculates second spatial derivative:

$$(\mathbf{L}f)_i = \frac{2}{y_{i+1} - y_{i-1}} \left(\frac{f_{i+1} - f_i}{y_{i+1} - y_i} - \frac{f_i - f_{i-1}}{y_i - y_{i-1}} \right) \quad (C.8)$$

After that, following matrices are constructed:

$$\mathbf{F} = \mathbf{L} - \alpha^2 \mathbf{I} \quad (\text{C.9})$$

$$\mathbf{A} = \frac{1}{iRe\alpha} \mathbf{F}\mathbf{F} - \text{diag}(U)\mathbf{F} + \text{diag}(\mathbf{L}U) \quad (\text{C.10})$$

$$\mathbf{B} = -\mathbf{F} \quad (\text{C.11})$$

Using this matrices, we rewrite discretized Orr-Sommerfeld equation in a form

$$(\mathbf{A} - c\mathbf{B})\phi = 0 \quad (\text{C.12})$$

This form is called “generalized eigenvalue problem”, differing from simple eigenvalue problem in that we have a matrix \mathbf{B} instead of identity matrix.

The important thing is boundary conditions: since boundary conditions are independent on c , they are only applied to \mathbf{A} , and in matrix \mathbf{B} there are zero rows in place of boundary conditions, but this would make matrix \mathbf{B} singular, not allowing to solve eigenvalue problem. We have four boundary conditions, in particularly zero values and zero gradient on each of the the boundaries. Therefore four nodes at the boundaries are excluded from eigenvalue problem, and the eigenfunction ϕ is forced to be zero at this points.

The eigenvalue problem of size $n - 4$ can be then solved by any of the available numerical methods.

Solution of eigenvalue problem gives a set of eigenvalues, c_j , and eigenvectors, ϕ_j , which are the shapes of the waves propagating with velocities c_j . The most interesting for us is the most unstable mode, which corresponds to the eigenvalue with largest imaginary part. Thus the eigenvalues are sorted in descending order by their imaginary part. Eigenvectors are the mode shapes corresponding to that eigenvalues.

Spatial stability

In spatial stability problem, we look for complex wave number α as a function of real wave speed c or angular frequency ω . For the later, Orr-Sommerfeld equation can be rewritten using the fact that $\omega = \alpha c$:

$$\left[\left(\frac{d^2}{dy^2} - \alpha^2 \right)^2 - iRe(\alpha U - \omega) \left(\frac{d^2}{dy^2} - \alpha^2 \right) \phi + iRe\alpha U'' \right] \phi = 0 \quad (\text{C.13})$$

Discretizing this equation using the same finite differences approach as in case of temporal stability, we get:

$$(\alpha^4 \mathbf{I} + \alpha^3 \mathbf{C}_3 + \alpha^2 \mathbf{C}_2 + \alpha \mathbf{C}_1 + \mathbf{C}_0) \phi = 0 \quad (\text{C.14})$$

where

$$\begin{aligned}
 \mathbf{C}_3 &= iRe \operatorname{diag}(U) \\
 \mathbf{C}_2 &= -(iRe\omega\mathbf{I} + 2\mathbf{L}) \\
 \mathbf{C}_1 &= iRe(\operatorname{diag}(\mathbf{L}U) - \operatorname{diag}(U)\mathbf{L}) \\
 \mathbf{C}_0 &= \mathbf{L}^2 + iRe\omega\mathbf{L}
 \end{aligned} \tag{C.15}$$

This is a non-linear eigenvalue problem, which can be solved using companion matrix method as described in [7]. Following this method, the above eigenvalue problem can be rewritten in the form

$$\left[\begin{pmatrix} -\mathbf{C}_3 & -\mathbf{C}_2 & -\mathbf{C}_1 & -\mathbf{C}_0 \\ \mathbf{I} & \mathbf{0} & \mathbf{0} & \mathbf{0} \\ \mathbf{0} & \mathbf{I} & \mathbf{0} & \mathbf{0} \\ \mathbf{0} & \mathbf{0} & \mathbf{I} & \mathbf{0} \end{pmatrix} - \alpha\mathbf{I} \right] \begin{pmatrix} \alpha^3\phi \\ \alpha^2\phi \\ \alpha\phi \\ \phi \end{pmatrix} = 0 \tag{C.16}$$

In this formulation, we have linear eigenvalue problem of size $4 \cdot (n - 4)$. This problem can be solved using conventional methods for eigenvalue problems. Mode of interest, the most unstable one, corresponds to the eigenvalue which has the lowest imaginary part. But it should be noted here that the spectrum contains several branches of continuous spectrum and unphysical eigenvalues, which should be excluded. First, all eigenvalues with negative real part are excluded as unphysical (propagating upstream). Then, an empiric rule is used to keep only eigenvalues satisfying a condition

$$|\alpha_i| < \alpha_r \tag{C.17}$$

It should be noted that this rule might not be suitable for all the cases, and thus should be verified for the particular problem. A set of validation cases used in this work is presented in [Table C.1](#).

Validation

List of validation cases is presented in [table C.1](#). The cases, for which ω and α are specified, are spatial stability cases, and for which α and c are specified, are temporal stability cases.

Table C.1: Validation cases

No.	Re	ω	α	c	Reference
Poiseuille flow $U(y) = 1 - y^2$, $y \in [-1, 1]$					
1	6000	0.26	$1.00047 - 0.00086i$		[7], Table IV
2	5772	0.26943	$1.020556 + 9.74 \cdot 10^{-7}i$		[7], Table III
3	100		1.0	$0.478494 - 0.162944i$	[35], Table 2
4	10000		1.0	$0.23763 + 0.00364i$	[35], Table 2
Couette flow $U(y) = y$, $y \in [-1, 1]$					
5	20		0.5	$-0.96066i$	[35], Table 4
Jet flow $U(y) = (\cosh y)^{-2}$					
6	12.58		1.0	0.3933	[35], Table 5
Blasius boundary layer					
7	336	0.1297	$0.30864 + 0.00799i$		[14], Table II
8	598	0.1201	$0.30801 - 0.00184i$		[14], Table II
9	998	0.1122	$0.30870 - 0.00564i$		[14], Table II
10	580		0.179	$0.3641 + 0.0080i$	[41], Table 1
11	1000		0.179	$0.3383 + 0.0048i$	[41], Table 1
12	2000		0.179	$0.3089 - 0.0166i$	[41], Table 1
13	5000		0.179	$0.3283 - 0.0294i$	[41], Table 1
14	10000		0.179	$0.3250 - 0.0325i$	[41], Table 1

Implementation details

The code is implemented using Python programming language and `numpy` and `scipy` libraries. `matplotlib` library is used for plotting. It has been developed and tested using Python versions 2.6.8 and 2.7.3, `numpy` version 1.6.2, and `scipy` version 0.10.0 and `matplotlib` version 1.1.0 More recent versions are expected to work as well, but not tested yet.

The solution of Orr-Sommerfeld equation itself is implemented in source file `orrsommerfeld.py`. All the automatic tests could be run with command

```
> python orrsommerfeld.py
```

Index

- actuation mode
 - burst, 34
 - continuous, 34
- actuator, 9
 - AC-DBD plasma actuator, 15
 - NS-DBD plasma actuator, 16
- actuators
 - plasma actuators, 14
- anode, 27
- arc phase, 28

- blowing and suction, 10
- breakdown voltage, 31

- cathode, 27
- coherent vortex structures, 57

- Dielectric Barrier Discharge, 14

- eigenvalue decomposition, 112
- electric breakdown, 15
- electrodes, 29
- equation
 - Arrhenius equation, 27
 - Boltzmann equation, 27
 - telegrapher's equations, 35
 - wave equation, 35

- filaments, 56
- flow control, 7
 - active, 8
 - passive, 8
 - reactive, 8

- frequency
 - actuation frequency, 34
 - burst frequency, 34
 - pulse frequency, 34
 - reduced frequency, 13

- impedance, 36
- ionic wind, 32, 55

- large-eddy simulation, 61
- LES, 61

- number
 - Mach number, 14
 - Strouhal number, 13

- offset, 31

- Particle Imaging Velocimetry, 65
- plasma, 24
- plasma channel, 23, 27
- pulse generator, 33
- pulse width, 32

- RANS, 61
- reaction constant, 27
- reaction cross-section, 27

- separation, 1
- singular value decomposition, 112
- stall, 1
- STOL (short takeoff and landing), 10
- streamer phase, 27
- sub-grid scale model, 61

synthetic jet, [12](#)

transmission line, [35](#)

vane, [9](#)

vortex generator, [9](#)

zero mass flow device, [12](#)

Bibliography

- [1] I V Adamovich, I Choi, N Jiang, J-H Kim, S Keshav, W R Lempert, E Mintusov, M Nishihara, M Samimy, and M Uddi. “Plasma assisted ignition and high-speed flow control: non-thermal and thermal effects”. In: *Plasma Sources Science and Technology* 18.3 (Aug. 2009), p. 034018. ISSN: 0963-0252. DOI: [10.1088/0963-0252/18/3/034018](https://doi.org/10.1088/0963-0252/18/3/034018) (cit. on pp. 28, 54, 80).
- [2] R Adrian. “Particle imaging techniques for experimental fluid mechanics”. In: *Annal Rev Fluid Mech* 23 (1991), pp. 261–304 (cit. on p. 66).
- [3] Ronald J Adrian. “Twenty years of particle image velocimetry”. In: *Experiments in Fluids* 39.2 (Aug. 2005), pp. 159–169. ISSN: 0723-4864. DOI: [10.1007/s00348-005-0991-7](https://doi.org/10.1007/s00348-005-0991-7) (cit. on p. 66).
- [4] Yu Akishev, G Aponin, A Balakirev, M Grushin, A Petryakov, V Karal’nik, and N Trushkin. “Stepwise expansion of a surface dielectric barrier discharge as a result of alternation in formation of streamers and leaders”. In: *Journal of Physics D: Applied Physics* 46.13 (Apr. 2013), p. 135204. ISSN: 0022-3727. DOI: [10.1088/0022-3727/46/13/135204](https://doi.org/10.1088/0022-3727/46/13/135204) (cit. on p. 14).
- [5] N L Aleksandrov, S V Kindysheva, M M Nudnova, and A Yu Starikovskiy. “Mechanism of ultra-fast heating in a non-equilibrium weakly ionized air discharge plasma in high electric fields”. In: *Journal of Physics D: Applied Physics* 43.25 (June 2010), p. 255201. ISSN: 0022-3727. DOI: [10.1088/0022-3727/43/25/255201](https://doi.org/10.1088/0022-3727/43/25/255201) (cit. on pp. 24, 26, 29, 54).
- [6] M Bergmann, C.-H. Bruneau, and A Iollo. “Enablers for robust POD models”. In: *Journal of Computational Physics* 228.2 (Feb. 2009), pp. 516–538. ISSN: 00219991. DOI: [10.1016/j.jcp.2008.09.024](https://doi.org/10.1016/j.jcp.2008.09.024) (cit. on pp. 68, 116).
- [7] T.J Bridges and P.J Morris. “Differential eigenvalue problems in which the parameter appears nonlinearly”. In: *Journal of Computational Physics* 55.3 (Sept. 1984), pp. 437–460. ISSN: 00219991. DOI: [10.1016/0021-9991\(84\)90032-9](https://doi.org/10.1016/0021-9991(84)90032-9) (cit. on pp. 91, 130, 131).

- [8] D M Bushnell. "TURBULENCE MODELING IN AERODYNAMIC - STATUS AND PROBLEMS". In: *29th Aerospace Sciences Meeting*. 1991 (cit. on p. 61).
- [9] Daniel Caruana, C Hollenstein, JP Boeuf, C Gleyzes, C Tropea, Eric Moreau, P Leyland, and F Rogier. "Flow Control by Plasma in PLASMAERO project". In: *Aerodays 2011*. April. Madrid, 2011, pp. 1–30 (cit. on p. 3).
- [10] Thomas C. Corke, C. Lon Enloe, and Stephen P. Wilkinson. "Dielectric Barrier Discharge Plasma Actuators for Flow Control". In: *Annu. Rev. Fluid Mech* (2010). DOI: [10.1146/annurev-fluid-121108-145550](https://doi.org/10.1146/annurev-fluid-121108-145550) (cit. on pp. 3, 15).
- [11] G. Correale, T. Michelis, D. Ragni, M. Kotsonis, and F. Scarano. "Nanosecond-pulsed plasma actuation in quiescent air and laminar boundary layer". In: *Journal of Physics D: Applied Physics* 47.10 (Mar. 2014), p. 105201. ISSN: 0022-3727. DOI: [10.1088/0022-3727/47/10/105201](https://doi.org/10.1088/0022-3727/47/10/105201) (cit. on pp. 52, 64–67).
- [12] Giuseppe Correale and Marios Kotsonis. "Effect of dielectric material on thermal effect produced by ns-DBD plasma actuator". In: *45th AIAA Plasmadynamics and Lasers Conference*. AIAA. Reston, Virginia: American Institute of Aeronautics and Astronautics, June 2014. ISBN: 978-1-62410-290-5. DOI: [10.2514/6.2014-2119](https://doi.org/10.2514/6.2014-2119) (cit. on pp. 29, 30, 32).
- [13] Giuseppe Correale, Ilia Popov, Aleksandr Rakitin, Andrei Starikovskii, Steven Hulshoff, and Leo Veldhuis. "Flow Separation Control on Airfoil With Pulsed Nanosecond Discharge Actuator". In: *49th AIAA Aerospace Sciences Meeting including the New Horizons Forum and Aerospace Exposition*. January. Reston, Virginia: American Institute of Aeronautics and Astronautics, Jan. 2011, pp. 2011–1079. ISBN: 978-1-60086-950-1. DOI: [10.2514/6.2011-1079](https://doi.org/10.2514/6.2011-1079) (cit. on pp. 20, 21, 52–54, 80, 82, 94, 104).
- [14] Gökhan Danabasoglu and Sedat Biringen. "A Chebyshev matrix method for the spatial modes of the Orr-Sommerfeld equation". In: *International Journal for Numerical Methods in Fluids* 11.7 (Nov. 1990), pp. 1033–1037. ISSN: 0271-2091. DOI: [10.1002/flid.1650110709](https://doi.org/10.1002/flid.1650110709) (cit. on p. 131).
- [15] Robyn A. Dawson and Jesse Little. "Effects of pulse polarity on nanosecond pulse driven dielectric barrier discharge plasma actuators". In: *Journal of Applied Physics* 115.4 (Jan. 2014), p. 043306. ISSN: 0021-8979. DOI: [10.1063/1.4863175](https://doi.org/10.1063/1.4863175) (cit. on p. 17).
- [16] Paul A Durbin. "Turbulence Closure Models for Computational Fluid Dynamics". In: *Fluids*. Ed. by Rene de Borst Erwin Stein and Thomas J R Hughes. Volume 3 F. Vol. 3. Encyclopedia of Computational Mechanics.

- John Wiley & Sons, Ltd, 2004. Chap. 10, pp. 301–324. ISBN: 0470846992 (cit. on p. 61).
- [17] A Flitti and S Pancheshnyi. “Gas heating in fast pulsed discharges in N₂–O₂ mixtures”. In: *The European Physical Journal Applied Physics* 45.2 (Feb. 2009), p. 21001. ISSN: 1286-0042. DOI: [10.1051/epjap/2009011](https://doi.org/10.1051/epjap/2009011) (cit. on p. 24).
- [18] Mohamed Gad-el-Hak. *Flow control: passive, active and reactive flow management*. Cambridge: Cambridge University Press, 2000. ISBN: 9780521770064. URL: <http://www.cambridge.org/9780521770064> (cit. on p. 68).
- [19] Y C Ganiev, V P Gordeev, a V Krasilnikov, V I Lagutin, V N Otmennikov, and a V Panasenko. “Aerodynamic Drag Reduction by Plasma and Hot-Gas Injection”. In: *Journal of Thermophysics and Heat Transfer* 14.1 (Jan. 2000), pp. 10–17. ISSN: 0887-8722. DOI: [10.2514/2.6504](https://doi.org/10.2514/2.6504) (cit. on p. 14).
- [20] R H M Giepmans and M Kotsonis. “On the mechanical efficiency of dielectric barrier discharge plasma actuators”. In: *Applied Physics Letters* 98 (2011), pp. 130–132. DOI: [10.1063/1.3597652](https://doi.org/10.1063/1.3597652) (cit. on pp. 15, 16, 55).
- [21] Rogier Giepmans. “On Transition Delay with Plasma Actuators PIV”. Master of Science Thesis. 2011 (cit. on p. 16).
- [22] V. P. Gordeev, a. V. Krasil’nikov, V. I. Lagutin, and V. N. Otmennikov. “Experimental study of the possibility of reducing supersonic drag by employing plasma technology”. In: *Fluid Dynamics* 31.2 (Mar. 1996), pp. 313–317. ISSN: 0015-4628. DOI: [10.1007/BF02029693](https://doi.org/10.1007/BF02029693) (cit. on p. 14).
- [23] David Greenblatt and Israel J Wygnanski. “The control of flow separation by periodic excitation”. In: *Progress in Aerospace Sciences* 36.7 (Oct. 2000), pp. 487–545. ISSN: 03760421. DOI: [10.1016/S0376-0421\(00\)00008-7](https://doi.org/10.1016/S0376-0421(00)00008-7) (cit. on pp. 9–11, 13).
- [24] Martin O. L. Hansen. *Aerodynamics of Wind Turbines*. 2nd ed. London: Earthscan, 2008. ISBN: 978-1-84407-438-9 (cit. on p. 7).
- [25] CM Ho and Patrick Huerre. “Perturbed Free Shear Layers”. In: *Annual Review of Fluid Mechanics* 16.1 (Jan. 1984), pp. 365–422. ISSN: 0066-4189. DOI: [10.1146/annurev.fl.16.010184.002053](https://doi.org/10.1146/annurev.fl.16.010184.002053) (cit. on p. 91).
- [26] Alec Houpt and Sergey B Leonov. “Dynamics of Charge Transfer by Surface Electric Discharges in Atmospheric Air”. In: *Journal of Applied Mathematics and Physics* 03.08 (2015), pp. 1062–1071. ISSN: 2327-4352. DOI: [10.4236/jamp.2015.38132](https://doi.org/10.4236/jamp.2015.38132) (cit. on p. 17).

- [27] P. Huerre and P. A. Monkewitz. “Absolute and convective instabilities in free shear layers”. In: *Journal of Fluid Mechanics* 159.-1 (Oct. 1985), p. 151. ISSN: 0022-1120. DOI: [10.1017/S0022112085003147](https://doi.org/10.1017/S0022112085003147) (cit. on p. 9).
- [28] Balaji Jayaraman and Wei Shyy. “Modeling of dielectric barrier discharge-induced fluid dynamics and heat transfer”. In: *Progress in Aerospace Sciences* 44.3 (Apr. 2008), pp. 139–191. ISSN: 03760421. DOI: [10.1016/j.paerosci.2007.10.004](https://doi.org/10.1016/j.paerosci.2007.10.004) (cit. on pp. 24, 51).
- [29] I N Kosarev, V I Khorunzhenko, E I Mintoussov, P N Sagulenko, N A Popov, and S M Starikovskaia. “A nanosecond surface dielectric barrier discharge at elevated pressures: time-resolved electric field and efficiency of initiation of combustion”. In: *Plasma Sources Science and Technology* 21.4 (Aug. 2012), p. 045012. ISSN: 0963-0252. DOI: [10.1088/0963-0252/21/4/045012](https://doi.org/10.1088/0963-0252/21/4/045012) (cit. on pp. 24, 54).
- [30] M Kotsonis, S Ghaemi, L Veldhuis, and F Scarano. “Measurement of the body force field of plasma actuators”. In: *Journal of Physics D: Applied Physics* 44.4 (Feb. 2011), p. 045204. ISSN: 0022-3727. DOI: [10.1088/0022-3727/44/4/045204](https://doi.org/10.1088/0022-3727/44/4/045204) (cit. on pp. 3, 16, 55).
- [31] M Kotsonis and L Veldhuis. “Experimental study on dielectric barrier discharge actuators operating in pulse mode”. In: *Journal of Applied Physics* 108 (2010), pp. 1–9. DOI: [10.1063/1.3517453](https://doi.org/10.1063/1.3517453) (cit. on pp. 3, 15, 16, 55).
- [32] Marios Kotsonis. “Dielectric Barrier Discharge Actuators for Flow Control: Diagnostics, Modeling, Application”. PhD thesis. 2011 (cit. on pp. 15, 16).
- [33] L.D. Kral. “Recent experience with different turbulence models applied to the calculation of flow over aircraft components”. In: *Progress in Aerospace Sciences* 34.7-8 (Nov. 1998), pp. 481–541. ISSN: 03760421. DOI: [10.1016/S0376-0421\(98\)00009-8](https://doi.org/10.1016/S0376-0421(98)00009-8) (cit. on p. 61).
- [34] J Kriegseis, S Grundmann, and C Tropea. “Power consumption, discharge capacitance and light emission as measures for thrust production of dielectric barrier discharge plasma actuators”. In: *Journal of Applied Physics* 110.1 (2011), p. 013305. ISSN: 00218979. DOI: [10.1063/1.3603030](https://doi.org/10.1063/1.3603030) (cit. on pp. 3, 15).
- [35] L. H. LEE and W. C. REYNOLDS. “ON THE APPROXIMATE AND NUMERICAL SOLUTION OF ORR-SOMMERFELD PROBLEMS”. In: *The Quarterly Journal of Mechanics and Applied Mathematics* 20.1 (1967), pp. 1–22. ISSN: 0033-5614. DOI: [10.1093/qjmam/20.1.1](https://doi.org/10.1093/qjmam/20.1.1) (cit. on p. 131).

- [36] Alexandre V Likhanskii, Mikhail N Shneider, Sergey O Macheret, and Richard B Miles. “Modeling of dielectric barrier discharge plasma actuators driven by repetitive nanosecond pulses”. In: *Physics of Plasmas* 14.7 (2007), p. 073501. ISSN: 1070664X. DOI: [10.1063/1.2744227](https://doi.org/10.1063/1.2744227) (cit. on p. 24).
- [37] Jesse Little and Mo Samimy. “High-Lift Airfoil Separation with Dielectric Barrier Discharge Plasma Actuation”. In: *AIAA Journal* 48.12 (Dec. 2010), pp. 2884–2898. ISSN: 0001-1452. DOI: [10.2514/1.J050452](https://doi.org/10.2514/1.J050452) (cit. on p. 16).
- [38] Jesse Little, Keisuke Takashima, Munetake Nishihara, Igor Adamovich, and Mo Samimy. “High Lift Airfoil Leading Edge Separation Control with Nanosecond Pulse DBD Plasma Actuators”. In: *5th Flow Control Conference*. July. Reston, Virginia: American Institute of Aeronautics and Astronautics, June 2010. ISBN: 978-1-62410-140-3. DOI: [10.2514/6.2010-4256](https://doi.org/10.2514/6.2010-4256) (cit. on pp. 56, 80).
- [39] Javier Lopera, T Terry Ng, Mehul P. Patel, Srikanth Vasudevan, Ed Santavicca, and Thomas C. Corke. “Aerodynamic Control of Using Windward-Surface Plasma Actuators on a Separation Ramp”. In: *Journal of Aircraft* 44.6 (Nov. 2007), pp. 1889–1895. ISSN: 0021-8669. DOI: [10.2514/1.30741](https://doi.org/10.2514/1.30741) (cit. on p. 3).
- [40] S K Lyubutin, S N Rukin, B G Slovikovskii, and S N Tsyranov. “High-frequency pulse generators based on SOS diodes with subnanosecond current cutoff time”. In: *Instruments and Experimental Techniques* 43.3 (May 2000), pp. 331–338. ISSN: 0020-4412. DOI: [10.1007/BF02759030](https://doi.org/10.1007/BF02759030) (cit. on pp. 18, 33).
- [41] Leslie M. Mack. “A numerical study of the temporal eigenvalue spectrum of the Blasius boundary layer”. In: *Journal of Fluid Mechanics* 73.03 (Feb. 1976), p. 497. ISSN: 0022-1120. DOI: [10.1017/S002211207600147X](https://doi.org/10.1017/S002211207600147X) (cit. on p. 131).
- [42] Antonello Marino, Pietro Catalano, Claudio Marongiu, Philip Peschke, Christoph Hollenstein, and R Donelli. “Effects of High Voltage Pulsed DBD on the Aerodynamic Performances in Subsonic and Transonic Conditions”. In: *43rd Fluid Dynamics Conference*. Reston, Virginia: American Institute of Aeronautics and Astronautics, June 2013, pp. 1–15. ISBN: 978-1-62410-214-1. DOI: [10.2514/6.2013-2752](https://doi.org/10.2514/6.2013-2752) (cit. on p. 21).
- [43] E I Mintousov, S J Pendleton, F G Gerbault, N A Popov, and S M Starikovskaia. “Fast gas heating in nitrogen–oxygen discharge plasma: II. Energy exchange in the afterglow of a volume nanosecond discharge at moderate pressures”. In: *Journal of Physics D: Applied Physics* 44.28 (July 2011),

- p. 285202. ISSN: 0022-3727. DOI: [10.1088/0022-3727/44/28/285202](https://doi.org/10.1088/0022-3727/44/28/285202) (cit. on pp. 24, 54).
- [44] Eric Moreau. “Airflow control by non-thermal plasma actuators”. In: *Journal of Physics D: Applied Physics* 40.3 (Feb. 2007), pp. 605–636. ISSN: 0022-3727. DOI: [10.1088/0022-3727/40/3/S01](https://doi.org/10.1088/0022-3727/40/3/S01) (cit. on p. 3).
- [45] G V Naidis. “Simulation of spark discharges in high-pressure air sustained by repetitive high-voltage nanosecond pulses”. In: *Journal of Physics D: Applied Physics* 41.23 (Dec. 2008), p. 234017. ISSN: 0022-3727. DOI: [10.1088/0022-3727/41/23/234017](https://doi.org/10.1088/0022-3727/41/23/234017) (cit. on p. 29).
- [46] R Narasimha and S N Prasad. “Leading edge shape for flat plate boundary layer studies”. In: *Experiments in Fluids* 17.5 (Sept. 1994), pp. 358–360. ISSN: 0723-4864. DOI: [10.1007/BF01874418](https://doi.org/10.1007/BF01874418) (cit. on p. 64).
- [47] A.C. Aba’a Ndong, N Zouzou, N Benard, and E Moreau. “Geometrical optimization of a surface DBD powered by a nanosecond pulsed high voltage”. In: *Journal of Electrostatics* 71.3 (June 2013), pp. 246–253. ISSN: 03043886. DOI: [10.1016/j.elstat.2012.11.030](https://doi.org/10.1016/j.elstat.2012.11.030) (cit. on p. 31).
- [48] D F Opaits, M N Shneider, and R B Miles. “Electrodynamic effects in nanosecond-pulse-sustained long dielectric-barrier-discharge plasma actuators”. In: *Applied Physics Letters* 94.6 (2009), p. 061503. ISSN: 00036951. DOI: [10.1063/1.3081027](https://doi.org/10.1063/1.3081027) (cit. on p. 34).
- [49] Dmitry F Opaits, Alexandre V Likhanskii, Gabriele Neretti, Sohail Zaidi, Mikhail N Shneider, Richard B Miles, and Sergey O Macheret. “Experimental investigation of dielectric barrier discharge plasma actuators driven by repetitive high-voltage nanosecond pulses with dc or low frequency sinusoidal bias”. In: *Journal of Applied Physics* 104.4 (2008), p. 043304. ISSN: 00218979. DOI: [10.1063/1.2968251](https://doi.org/10.1063/1.2968251) (cit. on pp. 3, 34).
- [50] S Pancheshnyi, M Nudnova, and A Starikovskii. “Development of a cathode-directed streamer discharge in air at different pressures: Experiment and comparison with direct numerical simulation”. In: *Physical Review E* 71.1 (Jan. 2005), p. 016407. ISSN: 1539-3755. DOI: [10.1103/PhysRevE.71.016407](https://doi.org/10.1103/PhysRevE.71.016407) (cit. on pp. 17, 27, 51).
- [51] S Pancheshnyi, P Ségur, J. Capeillère, and A. Bourdon. “Numerical simulation of filamentary discharges with parallel adaptive mesh refinement”. In: *Journal of Computational Physics* 227.13 (June 2008), pp. 6574–6590. ISSN: 00219991. DOI: [10.1016/j.jcp.2008.03.020](https://doi.org/10.1016/j.jcp.2008.03.020) (cit. on p. 51).

- [52] Sergey Pancheshnyi, Ilya Popov, and Andrey Starikovskiy. “Using a non-diffusive hybrid scheme for simulation of filamentary discharges”. In: *Bulletin of the American Physical Society*. Vol. 55. American Physical Society, 2010, p. 2008. URL: <http://meetings.aps.org/link/BAPS.2010.GEC.DTP.158> (cit. on pp. 27, 51).
- [53] U Piomelli. “Large-eddy simulation: achievements and challenges”. In: *Progress in Aerospace Sciences* 35.4 (May 1999), pp. 335–362. ISSN: 03760421. DOI: [10.1016/S0376-0421\(98\)00014-1](https://doi.org/10.1016/S0376-0421(98)00014-1) (cit. on p. 61).
- [54] Ugo Piomelli. “Wall-layer models for large-eddy simulations”. In: *Progress in Aerospace Sciences* 44.6 (Aug. 2008), pp. 437–446. ISSN: 03760421. DOI: [10.1016/j.paerosci.2008.06.001](https://doi.org/10.1016/j.paerosci.2008.06.001) (cit. on p. 61).
- [55] Ugo Piomelli. “Large-eddy and direct simulation of turbulent flows”. In: *9e conference annule de la Societe canadienne de CFD* (cit. on p. 61).
- [56] Ilya Popov, Giuseppe Correale, and Steven Hulshoff. “Numerical Simulations of Disturbances in Shear Flows Introduced by NS-DBD Plasma Actuators”. In: *46th AIAA Plasmadynamics and Lasers Conference*. June. Reston, Virginia: American Institute of Aeronautics and Astronautics, June 2015, pp. 1–14. ISBN: 978-1-62410-360-5. DOI: [10.2514/6.2015-2340](https://doi.org/10.2514/6.2015-2340) (cit. on p. 63).
- [57] Ilya Popov and Steven Hulshoff. “Numerical Investigation of Instabilities in Free Shear Layer Produced by NS-DBD Actuator”. In: *ICCFD 2012* 6.8 (2012), pp. 1345–1353. URL: <http://www.waset.org/publications/8047> (cit. on p. 79).
- [58] Ilya Popov, Andrey Nikipelov, Sergey Pancheshnyi, Giuseppe Correale, Steven Hulshoff, Leo Veldhuis, Sohail Zaidi, and Andrey Starikovskiy. “Experimental Study and Numerical Simulation of Flow Separation Control with Pulsed Nanosecond Discharge Actuator”. In: *51st AIAA Aerospace Sciences Meeting including the New Horizons Forum and Aerospace Exposition*. Vol. 56. January. Reston, Virginia: American Institute of Aeronautics and Astronautics, Jan. 2013. ISBN: 978-1-62410-181-6. DOI: [10.2514/6.2013-572](https://doi.org/10.2514/6.2013-572) (cit. on pp. 3, 52).
- [59] N A Popov. “Investigation of the mechanism for rapid heating of nitrogen and air in gas discharges”. In: *Plasma Physics Reports* 27.10 (Oct. 2001), pp. 886–896. ISSN: 1063-780X. DOI: [10.1134/1.1409722](https://doi.org/10.1134/1.1409722) (cit. on p. 54).
- [60] Yuri P. Raizer. *Gas Discharge Physics*. Ed. by John E Allen. Berlin Heidelberg: Springer-Verlag, 1991. ISBN: 978-3-642-64760-4 (cit. on pp. 23, 24, 27).

- [61] Chris Rethmel, Jesse Little, Keisuke Takashima, Aniruddha Sinha, Igor Adamovich, and Mo Samimy. “Flow Separation Control Using Nanosecond Pulse Driven DBD Plasma Actuators”. In: *International Journal of Flow Control* 3.4 (Dec. 2011), pp. 213–232. ISSN: 1756-8250. DOI: [10.1260/1756-8250.3.4.213](https://doi.org/10.1260/1756-8250.3.4.213) (cit. on p. 3).
- [62] David Riggins, H F Nelson, and Eric Johnson. “Blunt-Body Wave Drag Reduction Using Focused Energy Deposition”. In: *AIAA Journal* 37.4 (Apr. 1999), pp. 460–467. ISSN: 0001-1452. DOI: [10.2514/2.756](https://doi.org/10.2514/2.756) (cit. on p. 14).
- [63] D. V. Roupasov, A. A. Nikipelov, M. M. Nudnova, and A. Yu. Starikovskii. “Flow Separation Control by Plasma Actuator with Nanosecond Pulsed-Periodic Discharge”. In: *AIAA Journal* 47.1 (Jan. 2009), pp. 168–185. ISSN: 0001-1452. DOI: [10.2514/1.38113](https://doi.org/10.2514/1.38113) (cit. on pp. 3, 18, 21, 58, 60, 79, 80).
- [64] F Scarano. “Tomographic PIV: principles and practice”. In: *Measurement Science and Technology* 24.1 (Jan. 2013), p. 012001. ISSN: 0957-0233. DOI: [10.1088/0957-0233/24/1/012001](https://doi.org/10.1088/0957-0233/24/1/012001) (cit. on p. 66).
- [65] Moon Soo Bak and Mark A Cappelli. “Simulations of nanosecond-pulsed dielectric barrier discharges in atmospheric pressure air”. In: *Journal of Applied Physics* 113.11 (2013), p. 113301. ISSN: 00218979. DOI: [10.1063/1.4795269](https://doi.org/10.1063/1.4795269) (cit. on pp. 27, 51).
- [66] P.R Spalart. “Strategies for turbulence modelling and simulations”. In: *International Journal of Heat and Fluid Flow* 21.3 (June 2000), pp. 252–263. ISSN: 0142727X. DOI: [10.1016/S0142-727X\(00\)00007-2](https://doi.org/10.1016/S0142-727X(00)00007-2) (cit. on p. 61).
- [67] Andrei Yu. Starikovskii, Nikolai B Anikin, Ilya N Kosarev, Eugeny I Mintoussov, Maria M Nudnova, Aleksandr E Rakitin, Dmitry V Roupasov, Svetlana M Starikovskaia, and Victor P Zhukov. “Nanosecond-Pulsed Discharges for Plasma-Assisted Combustion and Aerodynamics”. In: *Journal of Propulsion and Power* 24.6 (Nov. 2008), pp. 1182–1197. ISSN: 0748-4658. DOI: [10.2514/1.24576](https://doi.org/10.2514/1.24576) (cit. on pp. 3, 52).
- [68] Andrey Starikovskii, Maryia Nudnova, Svetlana Kindusheva, and Nikolay Aleksahdrov. “Rate of Plasma Thermalization of Pulsed Nanosecond Surface Dielectric Barrier Discharge”. In: *48th AIAA Aerospace Sciences Meeting Including the New Horizons Forum and Aerospace Exposition*. 0465. Reston, Virginia: American Institute of Aeronautics and Astronautics, Jan. 2010. ISBN: 978-1-60086-959-4. DOI: [10.2514/6.2010-465](https://doi.org/10.2514/6.2010-465) (cit. on pp. 29, 58, 80).

- [69] Andrey Starikovskiy, Yong Yang, Young I Cho, and Alexander Fridman. “Non-equilibrium plasma in liquid water: dynamics of generation and quenching”. In: *Plasma Sources Science and Technology* 20.2 (Apr. 2011), p. 024003. ISSN: 0963-0252. DOI: [10.1088/0963-0252/20/2/024003](https://doi.org/10.1088/0963-0252/20/2/024003) (cit. on p. 24).
- [70] Keisuke Takashima (Udagawa), Yvette Zuzeek, Walter R Lempert, and Igor V Adamovich. “Characterization of a surface dielectric barrier discharge plasma sustained by repetitive nanosecond pulses”. In: *Plasma Sources Science and Technology* 20.5 (Oct. 2011), p. 055009. ISSN: 0963-0252. DOI: [10.1088/0963-0252/20/5/055009](https://doi.org/10.1088/0963-0252/20/5/055009) (cit. on pp. 52, 54).
- [71] T Unfer and J P Boeuf. “Modelling of a nanosecond surface discharge actuator”. In: *Journal of Physics D: Applied Physics* 42.19 (Oct. 2009), p. 194017. ISSN: 0022-3727. DOI: [10.1088/0022-3727/42/19/194017](https://doi.org/10.1088/0022-3727/42/19/194017) (cit. on pp. 27, 51, 58).
- [72] Da A Xu, Deanna A Lacoste, Diane L Rusterholtz, Paul-quentin Elias, Gabi D Stancu, and Christophe O. Laux. “Experimental study of the hydrodynamic expansion following a nanosecond repetitively pulsed discharge in air”. In: *Applied Physics Letters* 99.12 (2011), p. 121502. ISSN: 00036951. DOI: [10.1063/1.3641413](https://doi.org/10.1063/1.3641413) (cit. on p. 3).
- [73] Yifei Zhu, Yun Wu, Wei Cui, Yinghong Li, and Min Jia. “Modelling of plasma aerodynamic actuation driven by nanosecond SDBD discharge”. In: *Journal of Physics D: Applied Physics* 46.35 (Sept. 2013), p. 355205. ISSN: 0022-3727. DOI: [10.1088/0022-3727/46/35/355205](https://doi.org/10.1088/0022-3727/46/35/355205) (cit. on p. 24).

List of publications

Journal articles

- [A1] I. B. Popov and S. J. Hulshoff. “Computational Study of Dynamics of Disturbances Introduced into a Free Shear Layer by NS-DBD Actuator”. In: (2016). In preparation.
- [A2] I. B. Popov and S. J. Hulshoff. “Modeling of a NS-DBD Plasma Actuator in a Laminar Boundary Layer”. In: (2016). In preparation.

Conference papers

- [B1] Ilya Popov, Giuseppe Correale, and Steven Hulshoff. “Numerical Simulations of Disturbances in Shear Flows Introduced by NS-DBD Plasma Actuators”. In: *46th AIAA Plasmadynamics and Lasers Conference*. Dallas, Texas: American Institute of Aeronautics and Astronautics, June 2015, pp. 1–14. ISBN: 978-1-62410-360-5. DOI: [10.2514/6.2015-2340](https://doi.org/10.2514/6.2015-2340).
- [B2] T. Michelis, G. Correale, I. B. Popov, M. Kotsonis, D. Ragni, S. J. Hulshoff, and L. L. M. Veldhuis. “Disturbance introduced into a laminar Boundary Layer by a NS-DBD plasma actuator”. In: *51st AIAA Aerospace Sciences Meeting, Grapevine, Texas, USA*. 2013. DOI: [10.2514/6.2013-752](https://doi.org/10.2514/6.2013-752).
- [B3] I. B. Popov, A. Nikipelov, S. Pancheshnyi, G. Correale, S. J. Hulshoff, L. L. M. Veldhuis, S. Zaidi, and A. Starikovskiy. “Experimental Study and Numerical Simulation of Flow Separation Control with Pulsed Nanosecond Discharge Actuator”. In: *51st AIAA Aerospace Sciences Meeting including the New Horizons Forum and Aerospace Exposition*. American Institute of Aeronautics and Astronautics. Grapevine, Texas, USA, 2013. DOI: [10.2514/6.2013-572](https://doi.org/10.2514/6.2013-572).
- [B4] Ilya Popov and Steven Hulshoff. “Numerical Investigation of Instabilities in Free Shear Layer Produced by NS-DBD Actuator”. In: *ICCFD 2012, Paris*. Vol. 6. 8. WASET. 2012. URL: <http://waset.org/publications/8047>.

- [B5] G. Correale, I. B. Popov, A. Nikipelov, S. Pancheshnyi, A. Yu. Starikovkii, S. J. Hulshoff, and L. L. M. Veldhuis. “Experimental study and numerical simulation of flow separation control with pulsed nanosecond discharge actuator”. In: *30th International Conference on Phenomena in Ionized Gases (ICPIG) (Belfast, Northern Ireland, August 28 – September 2, 2011)*. Aug. 28–Sept. 2, 2011. URL: http://mpserver.pst.qub.ac.uk/sites/icpig2011/218_D16_Pancheshnyi.pdf.
- [B6] G. Correale, I. B. Popov, A. E. Rakitin, A. Yu. Starikovskii, S. J. Hulshoff, and L. L. M. Veldhuis. “Flow Separation Control on Airfoil With Pulsed Nanosecond Discharge Actuator”. In: *49th AIAA Aerospace Sciences Meeting including the New Horizons Forum and Aerospace Exposition, Orlando, Florida*. 2011. DOI: [10.2514/6.2011-1079](https://doi.org/10.2514/6.2011-1079).
- [B7] G. Correale, I. Popov, A. Nikipelov, S. Pancheshnyi, S. Hulshoff, L. Veldhuis, and A. Starikovskiy. “Experimental study and numerical simulation of flow separation control with pulsed nanosecond discharge actuator”. In: *64th Annual Gaseous Electronics Conference (GEC, November 14–18, 2011; Salt Lake City, Utah)*. Vol. 56. 15. 2011. URL: <http://meetings.aps.org/link/BAPS.2011.GEC.TF1.8>.
- [B8] S. Pancheshnyi, I. Popov, and A. Starikovskiy. “Using a non-diffusive hybrid scheme for simulation of filamentary discharges”. In: *63rd Annual Gaseous Electronics Conference and 7th International Conference on Reactive Plasmas (October 4 – 8, 2010; Paris, France)*. Vol. 55. 7. 2010. URL: <http://meetings.aps.org/link/BAPS.2010.GEC.DTP.158>.
- [B9] I. Popov, G. Correale, A. Rakitin, A. Starikovskii, L. Veldhuis, and S. Hulshoff. “Flow Separation Control on Airfoil With Pulsed Nanosecond Discharge Actuator”. In: *63rd Annual Gaseous Electronics Conference and 7th International Conference on Reactive Plasmas*. Vol. 55. 7. 2010. URL: <http://meetings.aps.org/link/BAPS.2010.GEC.DTP.196>.

Reports

- [C1] Ilya Popov. *Implementation of POD and ROM for OpenFOAM*. Report. TU Delft, Aerospace Faculty, Aerodynamics Group, 2012.
- [C2] Ilya Popov. *Numerical Solution of an Orr-Sommerfeld Equation*. Report. TU Delft, Aerospace Faculty, Aerodynamics Group, 2012.
- [C3] Ilya Popov. *Simulation of a Sequence of Discharges*. Internal report. Version 3. NEQLab Research B.V., Aug. 19, 2011.

- [C4] Ilya Popov. *Simulation of Flow Separation Control Using Nanosecond Plasma Actuators: Recent Results*. Report. NEQLab Research B.V., Apr. 2011.
- [C5] Ilya Popov. *Validation of LES in OpenFOAM*. Report. TU Delft, Aerospace Faculty, Aerodynamics Group, 2011.
- [C6] Ilya Popov and Giuseppe Correale. *Experimental Investigation of Electrodynamic Properties of Long Nanosecond Actuator*. Report. NEQLab Research B.V., Feb. 5, 2011.
- [C7] Ilya Popov, Andrey Nikipelov, Cedric Boisdon, and Giuseppe Correale. *Experimental Investigation of Nanosecond Plasma Actuator Performance on Ampyx's Glider Wing in OJF Wind Tunnel of TU Delft (May 4–10, 2011)*. Internal report. NEQLab Research B.V., Oct. 28, 2011.

Patents

- [D1] Ilya Popov and Giuseppe Correale. "Boundary Layer Control via Nanosecond Dielectric/Resistive Barrier Discharge Plasma Actuator". PCT/EP2013/067532. Plasma and Innovation B.V. Aug. 23, 2013. Pending.

Publications in other fields

- [E1] G. Correale, A. Rakitin, A. Nikipelov, S. Pancheshnyi, I. Popov, A. Starikovskiy, T. Shiraishi, T. Urushihara, and M. Boot. "Non-equilibrium plasma ignition for internal combustion engines". In: *10th International Conference on Engines and Vehicles (ICE2011, Capri, Italy, September 11–15, 2011)*. SAE Technical Paper 2011-24-0090. 2011. DOI: [10.4271/2011-24-0090](https://doi.org/10.4271/2011-24-0090).
- [E2] A. Nikipelov, G. Correale, A. Rakitin, S. Pancheshnyi, I. Popov, A. Starikovskii, and M. Boot. "On-Board Plasma Assisted Fuel Reforming". In: *10th International Conference on Engines and Vehicles (ICE2011, Capri, Italy, September 11–15, 2011)*. SAE paper 2011-24-0088. Sept. 11, 2011. DOI: [10.4271/2011-24-0088](https://doi.org/10.4271/2011-24-0088).
- [E3] A. Nikipelov, I. Popov, S. Pancheshnyi, and A. Starikovskii. "Localized and distributed behavior of nanosecond pulse-periodic discharge in air". In: *30th International Conference on Phenomena in Ionized Gases (ICPIG) (Belfast, Northern Ireland, August 28 – September 2, 2011)*. 2011. URL: http://mpserver.pst.qub.ac.uk/sites/icpig2011/346_C10_Pancheshnyi.pdf.

- [E4] A. Nikipelov, I. Popov, S. Pancheshnyi, and A. Starikovskiy. “Localized and distributed behavior of nanosecond pulse-periodic discharge in air”. In: *64th Annual Gaseous Electronics Conference (GEC, November 14–18, 2011; Salt Lake City, Utah)*. Vol. 56. 15. Nov. 2011. URL: <http://meetings.aps.org/link/BAPS.2011.GEC.FTP1.65>.
- [E5] Andrei Nikipelov, Aleksandr Rakitin, Ilia Popov, Giuseppe Correale, and Andrei Starikovskii. “Plasmatrons Powered By Pulsed High-Voltage Nanosecond Discharge For Ultra-Lean Flames Stabilization”. In: *49th AIAA Aerospace Sciences Meeting including the New Horizons Forum and Aerospace Exposition*. 2011. DOI: [10.2514/6.2011-1214](https://doi.org/10.2514/6.2011-1214).
- [E6] A. E. Rakitin, I. B. Popov, and A. Yu. Starikovskii. “Detonation Initiation by a Gradient Mechanism in Propane-Oxygen and Propane-Air Mixtures”. In: *49th AIAA Aerospace Sciences Meeting including the New Horizons Forum and Aerospace Exposition*. Orlando, Florida, 2011. DOI: [10.2514/6.2011-586](https://doi.org/10.2514/6.2011-586).
- [E7] A. Rakitin, I. Popov, and A. Starikovskiy. “Detonation Initiation by Gradient Mechanism in Propane–Oxygen and Propane–Air Mixtures”. In: *64th Annual Gaseous Electronics Conference*. 2011. URL: <http://meetings.aps.org/link/BAPS.2011.GEC.TF1.7>.
- [E8] A. A. Nikipelov, I. B. Popov, G. Correale, A. E. Rakitin, and A. Yu. Starikovskii. “Compact catalyst-free liquid fuel to syngas reformer with plasma-assisted flame stabilization”. In: *48th AIAA Aerospace Sciences Meeting Including the New Horizons Forum and Aerospace Exposition*. 2010. DOI: [10.2514/6.2010-1343](https://doi.org/10.2514/6.2010-1343).
- [E9] A. Nikipelov, I. Popov, G. Correale, A. Rakitin, and A. Starikovskii. “Ultra-lean flames stabilization by high-voltage nanosecond pulsed discharge”. In: *XX European Conference on the Atomic and Molecular Physics of Ionized Gases, Novi Sad, Serbia*. 2010.
- [E10] Ilya Popov. *Simulations of Thermal Modes of the Reformer at Different Power Levels*. Report. NEQLab Research B.V., June 22, 2010.
- [E11] Ilya Popov. *Simulation of Heat Transfer in the Reformer*. Report. NEQLab Research B.V., Dec. 1, 2009.
- [E12] Ilya Popov. *Simulations of a Plasmatron*. Report. Version 3. NEQLab Research B.V., Dec. 11, 2009.

Acknowledgements

The course of the project which led to this thesis was not straight and simple. And completing this course would be impossible without support and participation of numerous people whom I would like to mention here.

First, I would like to thank my daily supervisor, *Steven Hulshoff*, for his continuous support, the time he devoted to me, for always being available for discussions and providing countless insights and ideas on the topic of the research.

I also thank my promoters, *Hester Bijl* during the first years of my PhD and *Fulvio Scarano* later. Without their support this project would not exist, and without their encouragement this project would not come to the finish.

Special thanks goes to *Guiseppe Correale*, who shared all the course of the project with me though all its twists. His experimental studies always came in parallel with the current work and provided important inputs. He also did a great job tirelessly seeking for promising applications and external partners.

Thanks to *Marios Kotsonis*, for leading plasma actuators research in the department, and to *Theo Michelis*, for his experimental work and invaluable discussions.

Great thanks goes to all the people of the Aerodynamics department, including scientific staff and technicians for their support, invaluable expertise, critical questions and discussions. Special thanks goes to secretary *Colette Russo*, whose role was crucial on all the stages of the project. Thanks to all the fellow PhD students, especially the ones in 'exile' in New Building — *Mustafa, Vahid, Wouter, Rogier, Ilias, Kyle, David, Thijs* and *Mehmed*, for discussions, both on science and unrelated topics. I'd also like to mention two master students with whom I had a pleasure to work, *François Pronk* and *Felipe Alves Portela*.

I would like to thank also all the colleagues at now defunct *NEQLab Research BV* who introduced me to the topic of NS-DBD plasma actuators and where the project originated, namely *Aleksandr, Andrey, Sergey, Paula, Cedric* and *Yuri*. Their expertise in plasma physics is laid in the basis of the model used in the present thesis. During the first two years of the project *NEQLab Research BV* also provided financial support and equipment for the project. Later during the project, great support also came from *Hans Stuker*, then director of *Cryonorm Projects BV*, and

his colleagues *Harold van Berkel* and *Fabienne Capostagno*.

I would also like to thank all my friends in the Netherlands during these years. During various periods of my stay in the Netherlands I had a pleasure to find perfect roommates and friends *Andrey, Maria, Aleksandr, Oleg* and *Tatiana*. Thank you for countless dinners and talks we had together. Also special thanks to my dear friends *Maria, Kirill, Katya, Oleksandr, Iryna, Taya, Alyna* and others. I also thank all the Russian-speaking sailing community in the Netherlands (*RDSC*), especially *Daniil* and *Michael*, for the great time we had together in IJsselmeer and Waddenzee.

And, of course, I am very grateful to my family — my mother, aunt and brothers, who always unconditionally supported and helped me during all these years despite being far away.

Curriculum Vitæ

Ilya POPOV

1983-08-11 Born in Moscow, Soviet Union

Education

1989–2000 School No. 223, then Mathematical School No. 2, Moscow, Russia

2000–2006 **B.Sc. and M.Sc. Degree** (cum Laude)
Moscow Institute of Physics and Technology (MIPT)
Faculty of Problems of Physics and Power Engineering
Department of Mathematical Modeling of Physical Phenomena
Thesis: *“LES Simulation of Atmospheric Boundary Layer above Non-Uniform Terrain”* Supervisor: V. N. Lykossov

2010–2016 **PhD candidate**
Delft University of Technology, Delft, the Netherlands
Aerospace Faculty, Aerodynamics Group
Thesis: *“Numerical Simulations of NS-DBD Plasma Actuators for Flow Control”* Promotor: E. Scarano; Supervisor: S. J. Hulshoff

Working Experience

2006–2009 **Embedded Software Developer**
Space Industry, Moscow, Russia

2009–2011 **Researcher & CFD Specialist**
NEQLab Research B.V., The Hague, the Netherlands

2012–2013 **Researcher & CFD Specialist**
PTD B.V., Alphen a/d Rijn, the Netherlands